UNIVERSITÀ DEGLI STUDI DI PADOVA

Dipartimento di Fisica e Astronomia ”Galileo Galilei”

Master Degree in Astrophysics and Cosmology

Final Dissertation

Age and kinematics of very metal-poor stars in the Galactic disk

Thesis supervisor
Prof. Giovanni Carraro

Thesis co-supervisor
Prof. Sergio Ortolani

Candidate
Anastasiia Plotnikova

Anno Accademico 2020-2021

Contents

1 Introduction

Stars with extremely low metal abundances are of particular astrophysical and cosmological interest because they probe very early times in the evolution of the Universe and its Galactic components. Through the investigation of the age, kinematics and chemical composition we can obtain important constraints on the evolution of the Milky Way, set up a lower limit of the age of the Universe and understand the chemical and dynamical properties of the first Population III supernovae.

Very metal-poor stars are one of the oldest objects in the Universe. Studies of these ancient stars have allowed stellar archaeologists to determine the chemical composition of the star-forming environments in the nascent Milky Way (Frebel & Norris (2015)). Over the years, several spectroscopic observation programs were conducted to study the chemical composition of very metal-poor stars. (Christlieb et al. (2004), Cayrel et al. (2004), Barklem et al. (2005), Schlaufman & Casey (2014), Limberg et al. (2021), etc.)

Furthermore, the precisely derived age of very metal-poor stars is an important test of the cosmological age of the Universe (Bond et al. (2013), VandenBerg et al. (2014)). The current best estimate of the age of the Universe is 13.82 ± 0.06 Gyr, based on the latest WMAP derivation of 13.77 ± 0.06 Gyr (Bennett et al. (2013)), in excellent agreement with observations of the CMB using the Planck satellite (Ade et al. (2014)). Recent simulations (e.g., Ritter et al. (2012), Safranek-Shrader et al. (2014)) suggest that the oldest Population II stars probably formed $\sim 0.2-0.3$ Gyr after the big bang, depending on how quickly the gas from the first (Population III) supernovae was able to cool and condense, as well on the the relevance and impact of the Population III feedback. Precise ages for the oldest and most metal-poor stars can date the onset of star formation (e.g., Bromm & Larson (2004)) following the Big Bang. Moreover, because the oldest stars must be younger than the Universe, precise ages provide a strong test of the consistency between cosmological and stellar physics.

Also, theoretical simulations of galaxy formation (Bullock & Johnston (2005)) have shown that the halo bears the signatures of the Milky Way's assembly from smaller "building block" galaxies. Recent astrometric studies have shown the existence of stellar kinematic signatures that indicate past accretion events (Belokurov et al. (2018); Myeong et al. (2019); Yuan et al. (2020)). That means that kinematics of very metal-poor stars is an important test of the Galaxy formation and evolution theories. Therefore, stars with low metal abundances are also possible members of accreted dwarf galaxies and/or clusters.

In the following work the age, kinematics and chemical composition of a sample of very metal poor stars were put under investigation. Our main goal is to answer to three important questions:

1. What is the age of the very metal-poor stars? How does it correlate with the age of the Universe (13.77 ± 0.06 Gyr) based on data on the cosmic microwave background (CMB), baryon acoustic oscillations, and Hubble constant (Bennett et al. (2013))?

2. Where were very metal-poor stars formed? Is it the disk, the bulge, the halo of the Milky Way, or these stars were captured by our Galaxy? Can these stars tell us about the evolution of the Milky Way or the component that at some time engulfed into it?

3. Is there any chemical signature which can show the peculiarity in chemical and physical processes of the star formation origin and tell information about the first Population III supernovae?

Section 2 presents a historical overview of Galaxy formation and evolution and results obtained about very metal-poor stars. Section 3 explains the choice of data set used in the current work. Precise study of photometry, distance, and following age determination are presented in section 4. Results of kinematics study with a deep investigation of orbits and orbital parameters are shown in section 5. In section 6 main chemical trends are provided. And finally, the results and conclusion are summarized in section 7.

2 Historical overview

2.1 History of the Milky Way formation

Investigation of the Galaxy formation started from ESL model. It is the popular scenario of the fast monolithic collapse suggested by Eggen, Lynden-Bell and Sandage (ESL model, Eggen et al. (1962)). This result was based on the detected correlation between metallicity [Fe/H] and orbital eccentricity e for old stars in a region a few hundred parsecs around the Sun. Low metallicity stars have very small angular momentum that means that they were formed with circular orbits in rapidly collapsing material. Halo was quickly collapsing to a thin rotating disk and the disk was enriched in heavy elements by subsequent star formation events.

Later Searle & Zinn (1978) pointed out a selection bias at the core of the that ESL results. Data set of old stars were formed from high proper motion stars. They remark that globular clusters cover a big range of metallicities without correlation with distance. This shows the evidence of the formation of the Galaxy through the merging of several small protogalaxies.

Nowadays monolithic collapse scenario is not considered viable anymore for our Galaxy, or only for the restricted component: central bulge. The stellar halo is lighter and less dense than the disk and could not collapse into the disk. The only possible place to collapse into is an old bulge (Gilmore (1996)). But despite the fact that bulge stars are old, some of them have the same metallicity as disk stars and it is not easily explained by this scenario either.

The second theory is the hierarchical scenario which tells that our Galaxy was formed through the hierarchical merging of dark halos. Accretion of baryonic matter occurs later. First, the bulge was formed, then progressively the thin disk. The thick disk could be produced as a consequence of heating induced by small/medium mass accreted companions.

The presence of stellar streams in stellar halo supports the hierarchical scenario (Helmi (2002), Ibata et al. (2002)): they are tidal remains of past merging events (Grillmair (2017)). Nowadays we have a number of confirmed accreted events such as Sagittarius dwarf galaxy, Gaia-Enceladus-Sausage, Sequoia, Helmi stream, and other streams are found to be associated with accreted dwarf galaxies/ globular clusters (Koppelman et al. (2019)). The halo of the Galaxy could be mostly built from minor mergers. Furthermore, the fact that merging frequency is increasing with increasing redshift tells us that at time of the beginning of the Galaxy formation merging events were more common. That lends further support to the hierarchical scenario.

The last and most successful scenario is Secular Evolution (SE), with slow and continuous external matter accretion. In this theory, the bulge of the Galaxy was formed due to the accretion of disk matter through the bar dynamics. This scenario is in agreement with the observed color gradient and the relation between the color of bulge and disk studied through statistical analysis of 257 spiral galaxies (Gadotti & dos Anjos (2001)). SE is also supported by the relation between the bulge and disk masses and radii (Courteau et al. (1996)).

Another point is that a radial metallicity gradient independent of luminosity was observed in a large sample of early-type galaxies (De Propris et al. (2005)). This contradicts with monolithic collapse scenario because metallicity changes should follow matter distribution (metallicity gradient is independent of luminosity). Besides, hierarchical model tells us that there should not be any metallicity gradient.

2.2 Metal-poor stars

Metal-poor stars are ideal probes of the beginning of the evolution of the Universe. Because of their low metallicity, they are linked to the most pristine star formation episodes in the Universe.

Over the years, investigations of metal-poor stars were limited by their faint apparent magnitude. As instrumentation improved, we started to have spectroscopically studied samples with an amount of stars large enough for statistical study.

Metal-poor stars have not been studied as extensively as stars with close-to-solar metallicity, because in nowadays universe they are rare objects. Due to star formation, newborn stars are polluted with metals from the cloud which was enriched in heavy elements from the first supernovae. That is why stars that have low metallicity were born in regions where cosmic star formation just started at high redshift. From Madau & Dickinson (2014) we know that starting from the beginning of the Universe in the first 3-4 billion years star formation rapidly increased and then slowly but continuously decreased from then until to date. Consequently, metal-poor stars are very old and if they are still alive they are typically low mass stars hence they have faint apparent magnitudes, which causes difficulties for their detection. Also to confirm the low metallicity abundance of the star high-resolution spectroscopical analysis needed to be done which is more difficult to perform for a large sample of stars compared with photometry.

The acquisition of high signal-to-noise spectra for faint metal-poor stars requires a major telescope-time commitment, making the construction of large samples of metal-poor star abundances prohibitively expensive. Schlaufman & Casey (2014) have developed a new, efficient selection that uses only public, all-sky APASS optical, 2MASS near-infrared, and WISE mid-infrared photometry to identify bright metal-poor star candidates through their lack of molecular absorption near 4.6 microns. The result of the selection is a sample of 11 916 metal-poor star candidates with V < 14, that increases the number of publicly available candidates by more than five times in this magnitude range. The bright apparent magnitudes of this sample have eventually allowed high-resolution follow-up observations that have detected seven previously unknown stars with $\left[\frac{Fe}{H}\right] < -3.0$. The follow-up campaign has identified that $3.8^{+1.3}_{-1.1}\%$ of Schlaufman & Casey (2014) candidates have $\left[\frac{Fe}{H}\right] < -3.0$ and $32.5^{+3.0}_{-2.9}\%$ have $-3.0 < \left[\frac{Fe}{H}\right] < -2.0$. The bulge is the most likely location of any existing Galactic Population III stars, and an infrared-only variant of this selection is effective enough for the identification of metal-poor stars in the bulge. Indeed, two of confirmed metal-poor stars with $\left[\frac{Fe}{H}\right] < -2.7$ from Schlaufman & Casey (2014) sample are within about 2 kpc of the Galactic center. They increased the number of the most metal-poor stars known in the bulge.

Limberg et al. (2021) presented the results of spectroscopic follow-up for 1897 low-metallicity star candidates, selected from the Best Brightest (BB) Survey (Schlaufman & Casey (2014)), carried out with the GMOS-N/S (Gemini North/South telescopes) and Goodman (SOAR Telescope) spectrographs. From these low-resolution ($R \sim 2000$) spectra, they estimate carbon and α-element abundance ratios. Limberg et al. (2021) confirmed that 56% of this program stars are metal-poor ($\left[\frac{Fe}{H}\right] < -1.0$), 30% are very metal-poor (VMP; $\left[\frac{Fe}{H}\right] < -2.0$) and 2% are extremely metal-poor (EMP; $\left[\frac{Fe}{H}\right] < -3.0$). There are 191 carbon-enhanced metal-poor (CEMP) stars, resulting in CEMP fractions of 19% and 43% for the VMP and EMP regimes, respectively. Moreover, resulting data from spectroscopic analysis of Limberg et al. (2021) were combined with Gaia EDR3 astrometric information to delineate new target-selection criteria, which have been applied to the Goodman/SOAR candidates. This doubled the efficiency for identification of *bona-fide* VMP and EMP stars in comparison to random extractions from the BB catalog. They demonstrate that this target-selection approach can achieve success rates of 96%, 76%, 28% and 4% for $\left[\frac{Fe}{H}\right] \leq -1.5, \leq -2.0, \leq -2.5$ and ≤ -3.0, respectively. Finally, Limberg et al. (2021) investigated the kinematics of the studied sample. They found that several VMP/EMP ($\left[\frac{Fe}{H}\right] \leq -2.5$) stars can be associated with either the disk system or halo substructures like Gaia-Sausage/Enceladus and Sequoia.

Christlieb et al. (2004) and Barklem et al. (2005) were focused on the "r-process-enhanced metal-poor" stars. For ease of discussion, the r-process enhancement phenomenon in metal-poor stars was divided into two categories:

- r-I: metal-poor stars with $+0.3 \leq \left[\frac{Eu}{Fe}\right] \leq +1.0$ and $\left[\frac{Ba}{Eu}\right] < 0$;
- r-II:metal-poor stars with $\left[\frac{Eu}{Fe}\right] > +1.0$ and $\left[\frac{Ba}{Eu}\right] < 0$.

These objects are enormously important as they allow us to study, among other topics, the nature of the rapid neutron-capture process(es), and possibly identify the site(s) for this nucleo-synthesis process(es). Furthermore, and perhaps even more importantly, individual age determinations can be performed for these stars using long-lived radioactive isotopes, such as ^{232}Th (half-life 14.05 Gyr) or ^{238}U (4.468 Gyr). This allowed, for the first time in an extremely metal-poor star, the use of this technique to place a strong lower limit on the age of the Galaxy and consequently of the Universe. For example, Sneden et al. (2003), using new calculations for the Th/Eu production ratio, determined age of 12.8 ± 3 Gyr for CS 22892-052. The age of the Universe (13.77 ± 0.06 Gyr) is on the other hand based on data on the cosmic microwave background (CMB), baryon acoustic oscillations, and Hubble constant (Bennett et al. (2013)). However, to go deeper into this research topic more very-metal poor stars should be studied to obtain a large enough sample of r-process-enhanced stars for statistical analysis. Typically for several hundred confirmed metal-poor giants the $2 - 3\%$ r-II stars are expected to be among them (Christlieb et al. (2004)).

This spectral analysis gives as a result one of the largest sample of very metal-poor stars with homogenously-measured abundances of a significant number of individual elements. Given the large number of spectra to be processed, it is mandatory to use automated techniques for abundance analysis. This sample was used in the following work.

Also, investigations on individual metal-poor stars were done.

Bond et al. (2013) studied HD 140283 is an extremely metal-deficient and high-velocity sub-giant in the solar neighborhood, having a location in the Hertzsprung–Russell diagram where absolute magnitude is most sensitive to stellar age. Because it is bright, nearby, unreddened, and has a well-determined chemical composition, this star does not present most of critical issues in age determinations for globular clusters, for instnace. Using the Fine Guidance Sensors on the Hubble Space Telescope, they have measured a trigonometric parallax of 17.15 ± 0.14 mas for HD 140283. Using modern theoretical isochrones, which include effects of helium diffusion, revised nuclear reaction rates, and enhanced oxygen abundance, together with the precise distance Bond et al. (2013) identified an age of 14.46 ± 0.31 Gyr. The presented error includes only the uncertainty in the parallax, and is for adopted surface oxygen and iron abundances of [O/H] = −1.67

and [Fe/H] = −2.40. Uncertainties in the stellar parameters and chemical composition, especially the oxygen content, now contribute more to the error budget for the age of HD 140283 than does its distance, increasing the total uncertainty to about ±0.8 Gyr. Within the errors, the age of HD 140283 does not conflict with the age of the Universe, 13.77 ± 0.06 Gyr, based on the microwave background and Hubble constant, but this star must have formed soon after the big bang.

Subsequent work of VandenBerg et al. (2014) derived the most accurate ages for the oldest stars - nearby halo subgiants because their age determination depends almost entirely on just the measured parallaxes and absolute oxygen abundances. In this study, they have used the Fine Guidance Sensors on the Hubble Space Telescope to determine trigonometric parallaxes, with precisions of 2.1% or better, for the Population II subgiants HD84937, HD132475, and HD140283. High-quality spectra have been employed to derive their surface abundances of O, Fe, Mg, Si, and Ca, which are assumed to be 0.1−0.15 dex less than their initial abundances due to the effects of element internal diffusion. Comparisons of isochrones with the three subgiants on the ($\log T_{eff}$, M_V) diagram yielded ages of 12.08 ± 0.14, 12.56 ± 0.46, and 14.27 ± 0.38 Gyr for HD84937, HD132475, and HD140283, in turn, where each error bar includes only the parallax uncertainty. The total uncertainty is estimated to be $\sim \pm 0.8$ Gyr (larger in the case of the near-turnoff star HD84937). Although the age of HD140283 is greater than the age of the Universe as inferred from the cosmic microwave background by $\sim$ 0.4−0.5 Gyr, this disagreement is at a level of $< 1\sigma$. Nevertheless, the first Population II stars apparently formed very soon after the Big Bang. (Stellar models that neglect diffusive processes seem to be ruled out as they would predict that HD140283 is $\sim$ 1.5 Gyr older than the universe.) The field halo subgiants appear to be older than globular clusters at similar metallicities: if distances close to those implied by the RR Lyrae standard candle are assumed, HD140283 and HD132475 are older than M92 and M5 by $\sim$ 1.5 and $\sim$ 1.0 Gyr, respectively.

3 Data

The very rare class of objects known as the “r-process-enhanced metal-poor” stars was put as a target of investigation in Christlieb et al. (2004). Note that the term “metal-poor” is not necessarily referring to the overall metal-content of the star, which might in fact not be significantly below the solar value when the star under consideration also has strong over-abundances of C, N, and O. To detect these stars, Christlieb et al. (2004) adopt a two-step approach.

The targets were drawn from lists of confirmed metal-poor stars with $\left[\frac{Fe}{H}\right] < -2.5$ from the HK and Hamburg/ESO surveys (HES), where $\left[\frac{Fe}{H}\right]$ is determined from moderate-resolution (~ 2 Å) follow-up spectroscopy using the Ca II K technique of Beers et al. (1999). Christlieb et al. (2004) restricted the sample to stars with B-V > 0.5, because their primary interest was the cool, sharp-lined giants. The B-V colors are based on CCD photometry in the case of the HK-survey stars (recognizable by designations beginning with “CS” for Curtis Schmidt-telescope), or were derived directly from the HES objective-prism spectra, in case of the HES stars (designations beginning with “HE”). Despite this color selection, two stars later turned out to be dwarfs and a few to be subgiants.

In the Hamburg/ESO R-process Enhanced Star (HERES) survey, “snapshot” spectra of 373 very metal-poor stars, here meaning with $\left[\frac{Fe}{H}\right] \leq -1.51$ as judged from medium resolution spectra, have been obtained with VLT2-UVES. It covers a wavelength range of $3760 - 4980$ Å, and has an average signal-to-noise ratio of S/N ~ 54 per pixel over the spectral range, though some spectra have S/N as low as 17 and as high as 308. A $2''$ slit is employed giving a minimum resolving power of $R \approx 20\ 000$, though typically the resolving power is seeing limited and thus slightly better. As mentioned in Christlieb et al. (2004), the pipeline-reduced spectra are corrected to the stellar rest frame. Though the snapshot spectra typically would be considered low quality for abundance analysis, however, they contain a lot of information and abundances may be obtained for a significant number of elements with moderate precision (absolute rms errors of order 0.25 dex, relative errors of order 0.15 dex). Modern surveys of metal-poor stars, such as the ESO “First Stars” Large programme (Cayrel et al. (2004); Hill et al. (2002)), now retrieved significantly better quality spectra for of the order of 70 stars, before the spectra of similar quality to our snapshot spectra were typical for studies of very metal-poor stars (e.g. McWilliam, Preston, Sneden & Shectman (1995), McWilliam, Preston, Sneden & Searle (1995)).

The large number of stars observed in the HERES survey offers the possibility to investigate more general trends in metal-poor star abundances, age, kinematics, etc. in a previously unexplored statistical regime. In particular, the scatter in abundance distributions may provide important information on the mixing and the diversity of supernovae at early epochs. The study of Norris et al. (2001)), which investigated such scatter, drawing from different surveys in the literature, had of order 70 stars in this metallicity regime. This project provides a homogeneously analyzed sample of several hundred stars.

To obtain abundances of chemical elements, a software for automated analysis of the spectrum has been developed by Barklem et al. (2005), based on the Spectroscopy Made Easy (SME) package by Valenti & Piskunov (1996). SME consists of three components: a spectrum synthesis component written in C++, a parameter optimization component written in IDL, and a user interface written in IDL. Barklem et al. (2005) used only the first two tools. Their developed software is written in IDL, and essentially provides an alternative interface to the parameter optimization component, which in turn calls the spectrum synthesis component. Some minor adaptations and improvements to the SME codes were also made.

The final sample of stars analysed in Barklem et al. (2005) contains 253 stars with following restriction:

- Spectra showing strong molecular carbon features cannot be analysed by the method proposed by Barklem et al. (2005). That is why these type of stars were not included in their analysis.
- Also, an metallicity cut-off was applied: $\left[\frac{Fe}{H}\right] < -1.5$
- To cool stars ($T_{eff} < 4200$ K) were excluded from Barklem et al. (2005) analysis method too.
- The primarily interest of Barklem et al. (2005) was the cool, sharp-lined giants. That is why stars were restricted with B−V > 0.5.
- And finally stars suspected to be spectroscopic binaries or rotators, were also removed from the sample.

Elemental abundances of moderate precision (absolute rms errors of order 0.25 dex, relative rms errors of order 0.15 dex) have been obtained for 22 elements: C, Mg, Al, Ca, Sc, Ti, V, Cr, Mn, Fe, Co, Ni, Zn, Sr, Y, Zr, Ba, La, Ce, Nd, Sm, and Eu, where detectable.

These very metal-poor stars are located in the upper and lower parts of the Galactic halo ($|b| > 20^o$) (Fig.2). Moreover, they are found to be α-element enhancement.

Main characteristics of the data set:

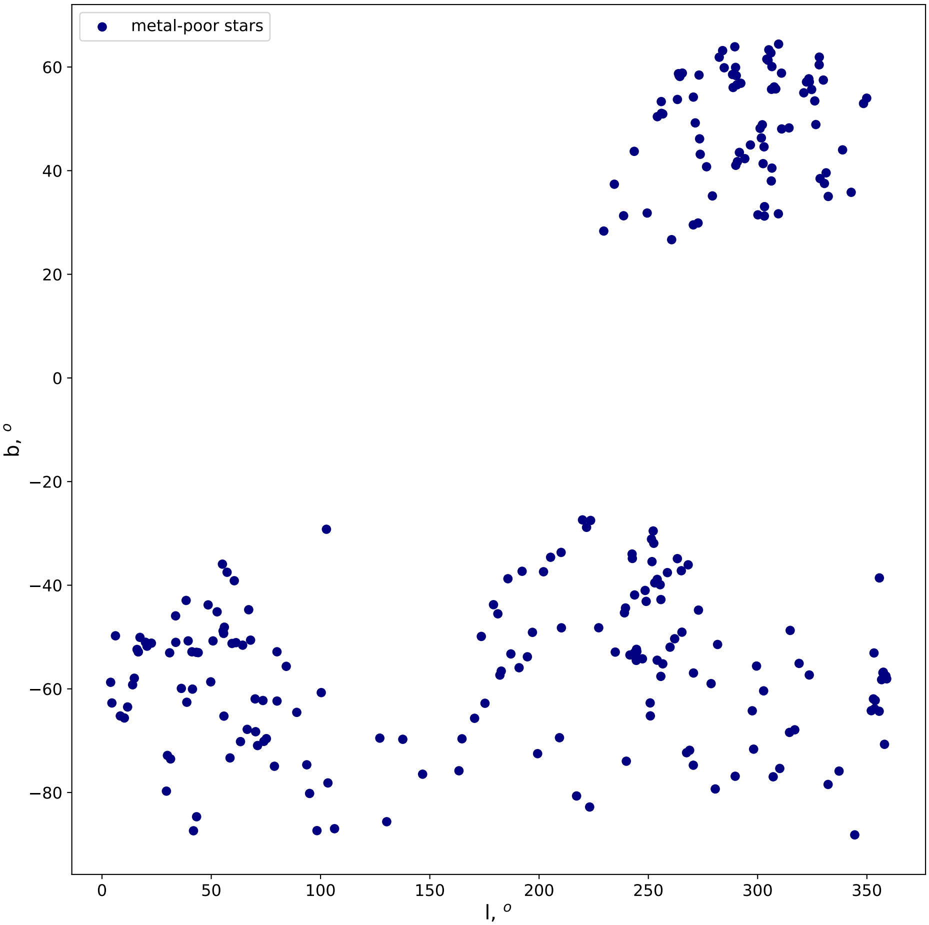

Figure 1: Location of 253 very metal-poor stars in galactic coordinates

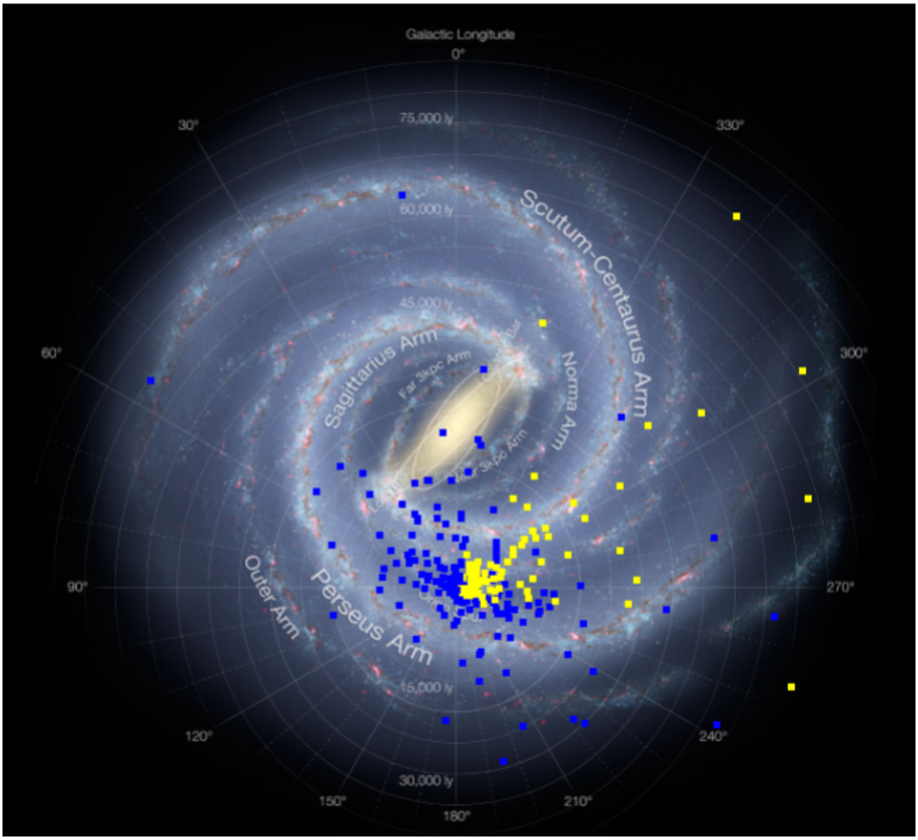

Figure 2: Location of 253 very metal-poor stars in Galactic plane. Blue dotes correspond to the lower Galactic halo, yellow are coming from the upper Galactic halo.

- The majority of the stars have brightness in Gaia EDR3 and Johnson photometry in range $12 < G < 17$ mag.

- Distance estimated with Gaia Early Data Release 3 parallaxes is lying in $0 < D < 30$ kpc range.

- Metallicity cover $-3.76 < \left[\frac{Fe}{H}\right] < 1.52$ dex values.

The distribution of stars in the listed below parameters are shown in Fig.3. Coordinates, photometry and chemical abundance are present in Tab.13, 15, 16.

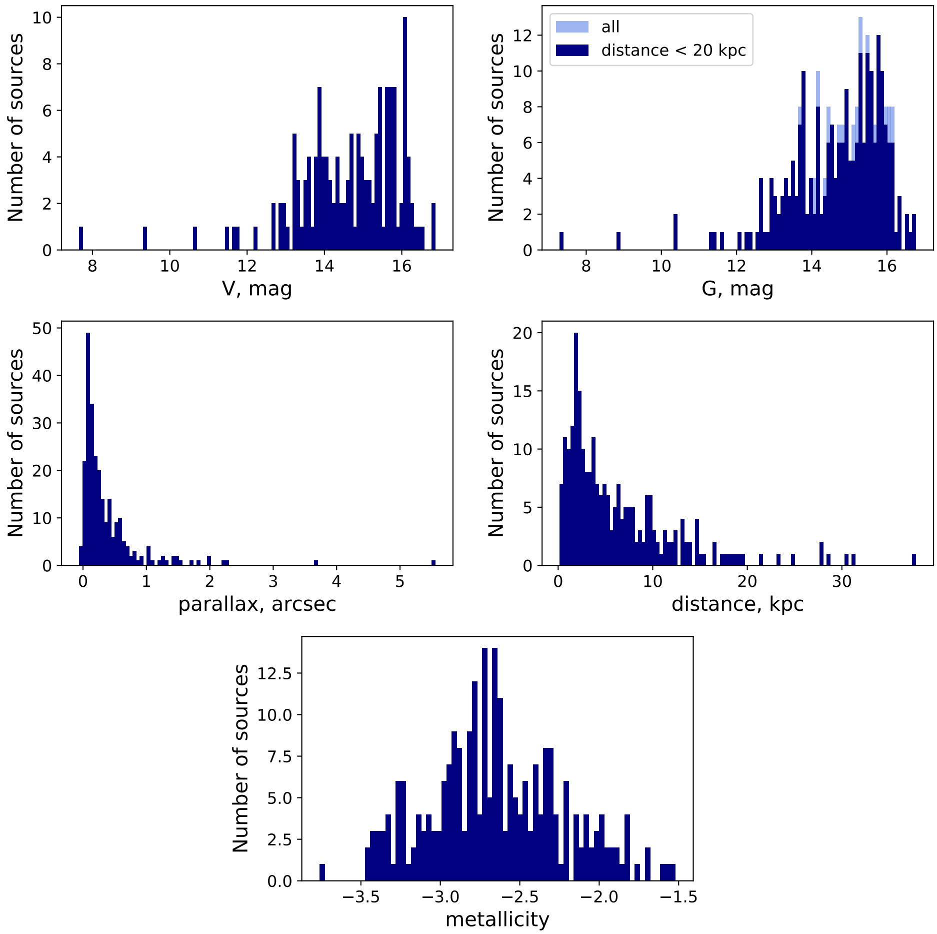

Figure 3: Distribution of very metal-poor stars in G-band (Gaia EDR3) - *top left*, V-band (Johnson) photometry - *top right*, in parallax Gaia EDR3 - *middle left*, distance from Gaia EDR3 parallax - *middle right*, in metallicity - *bottom*.

3.1 Check for binaries

Based on Gaia Early Data Release 3 El-Badry et al. (2021) develop an extensive catalog of spatially resolved binary stars within 1 kpc of the Sun, with projected separations ranging from a few AU to 1 pc. The catalog contains 1.3 (1.1) million binaries with $> 90\%$ ($> 99\%$) probability of being bound, including 16,000 white dwarf – main sequence (WD+MS) binaries and 1,400 WD+WD binaries. The amount of stars in studied data set that have distance according to Gaia EDR3 parallax less than 1 kpc of the Sun is equal to 27. All very metal-poor stars were check to be located in El-Badry et al. (2021) catalog[1]. No overlap between the data set and El-Badry et al. (2021) catalog of binary stars were found.

[1]https://zenodo.org/record/4435257

4 Age determination

For determining the age we studied the color-magnitude diagram (CMD) of the stars in the data set taking into consideration that they have close to each other age. CMD obtained in Johnson, taken from different literature sources, and Gaia Early Data Release 3 (Gaia EDR3)(Gaia Collaboration (2021)) photometry. Absolute magnitudes for all stars are calculated by means of distances from parallaxes: Gaia EDR3, Gaia EDR3 corrected by Lindegren et al. (2021) and derived by Bailer-Jones et al. (2021). Then isochrones for old metal-poor populations are used for deriving the precise age of the data set being studied. Padova isochrones and a Bag of Stellar Tracks and Isochrones (BaSTI) (Hidalgo et al. (2018)) used the most modern stellar models taking into account low metallicities.

4.1 Distance

Stellar distances constitute a foundational pillar of astrophysics. In our task, we need distances for computing absolute magnitudes and orbital parameters for our data set of very metal-poor stars. Distance is one of the important parameters that accuracy will affect future obtained results. That is why we should derive distances properly.

4.1.1 Gaia Early Data Release (Gaia EDR3) parallaxes

The first main technique is parallax distance. Today we have very accurate trigonometrically determined parallaxes (see for uncertainties Tab.1) obtained by Gaia satellite for around 1,47 billion stars (Gaia Collaboration (2021)). From these trigonometric parallaxes distance can be obtained through the following equation:

$$D = \frac{1}{\pi} \tag{1}$$

where D - distance to the object in pc, π - trigonometric parallax of the object in arcsec. The problem of this distance determination is that due to the structure of this equation uncertainties of the resulting distance are not symmetric around the mean value especially for big values of uncertainty. That is why errors for each source should be computed separately for the higher and lower borders of the distance:

$$D_{low} = \frac{1}{\pi + \Delta\pi} \tag{2}$$

$$D_{high} = \frac{1}{\pi - \Delta\pi} \tag{3}$$

The results are shown in Tab.14

Table 1: Uncertainties of Gaia Erly Data Release 3 astrometry Gaia Collaboration (2021)

Data product or source type	Typical uncertainty			
	G < 15	G = 17	G = 20	G = 21
Five-parameter astrometry				
position, mas	0.01 - 0.02	0.05	0.4	1
parallax, mas	0.02 - 0.03	0.07	0.5	1.3
proper motion, mas yr^{-1}	0.02 - 0.03	0.07	0.5	1.4
Six-parameter astrometry				
position, mas	0.02 - 0.03	0.08	0.4	1
parallax, mas	0.02 - 0.04	0.1	0.5	1.4
proper motion, mas yr^{-1}	0.02 - 0.04	0.1	0.6	1.5

4.1.2 Correction for Gaia EDR3 parallaxes

Lindegren et al. (2021) Parallaxes measured by Gaia Collaboration (2021) can have some bias that was measured by Lindegren et al. (2021). Lindegren et al. (2021) found that parallaxes that correspond to quasars (distant objects, whose parallaxes should be distributed around zero) have a systematical offset from the expected distribution around zero, by a few tens of microarcsec. Based on quasars bias for faint sources they extend the map of the correction to lower magnitudes using physical pairs (binaries) and Large Magellanic Cloud sources. The parallax bias is found to depend in a non-trivial way on (at least) the magnitude, color, and ecliptic latitude of the source. Different dependencies apply to the five- and six-parameter solutions in Gaia EDR3. While it is not possible to derive a definitive recipe for the parallax correction, they give tentative expressions to be used at the researcher's discretion and point out some possible paths towards future improvements. We applied the Lindegren et al. (2021) correction for downloaded Gaia EDR3 parallaxes for data set under investigation and then computed distance and its low and high limit through Eq.(1), (3), (2). The results are shown in Tab.14.

Bailer-Jones et al. (2021) Despite Gaia EDR3 high precision, the majority of stars observed by Gaia are distant or faint so that their parallax uncertainties are large and this prevents the direct inversion of parallax for obtaining distance. That is why Bailer-Jones et al. (2021) used a probabilistic approach to estimate stellar distances that uses a prior construction from a three-dimensional model of our Galaxy. This model includes interstellar extinction and Gaia's variable magnitude limit. They obtain two types of distance. The first, geometric, uses the parallax together with a direction-dependent prior on distance. The second, photogeometric, additionally uses the color and apparent magnitude of a star, by exploiting the fact that stars of a given color have a restricted range of probable absolute magnitudes (plus extinction). Tests on simulated data and external validations show that the photogeometric estimates generally have higher accuracy and precision for stars with poor parallaxes. This way, they provided a catalog of 1.47 billion geometric and 1.35 billion photogeometric distances together with asymmetric uncertainty measures from which distances were downloaded from the Gaia EDR3 by using `source_id` as a marker (output is shown in Tab.14)

The comparison of distances from Bailer-Jones et al. (2021) and parallaxes from Gaia EDR3 and corrected by Lindegren et al. (2021) are shown in Fig.4, 5. The vertical axis shows the Gaia EDR3 parallax and corrected parallax multiplied by the geometric (Fig.4), photogeometric (Fig.5) distance: values under 1 correspond to the parallax distance larger than the value of Bailer-Jones et al. (2021) distance and vice versa. The vertical error bars take into account the statistical uncertainties both on the parallax and the distance, but the horizontal error bars for the distance are not displayed. We can see that for close objects (< 3 kpc) parallaxes corrected by Lindegren et al. (2021) are in good agreement with Bailer-Jones et al. (2021) geometric and photo-geometric distances. After 3 kpc corrected parallaxes give higher distances than geometric and photo-geometric results. Ordinary Gaia EDR3 parallaxes yield higher distances in all ranges of distances. Some of the stars have negative parallaxes but positive distances can be derived from Bailer-Jones et al. (2021).

Finally, to consider the best estimate of distances for our data set deeper investigations should be done using color-magnitude diagram (CMD) and isochrone fitting technique. Which will proceed in section 4.2.2, 4.3.2.

4.2 Color-magnitude diagram

For the determination of age, we used a color-magnitude diagram. We studied CMD taking into consideration that all stars have similar ages. Distances obtained from different techniques (see Tab.14) were used to compute the absolute magnitude for each star.

4.2.1 Photometric systems

In this thesis, we used two different photometric data sets (Tab.): Gaia EDR3 photometry and Johnson photometry.

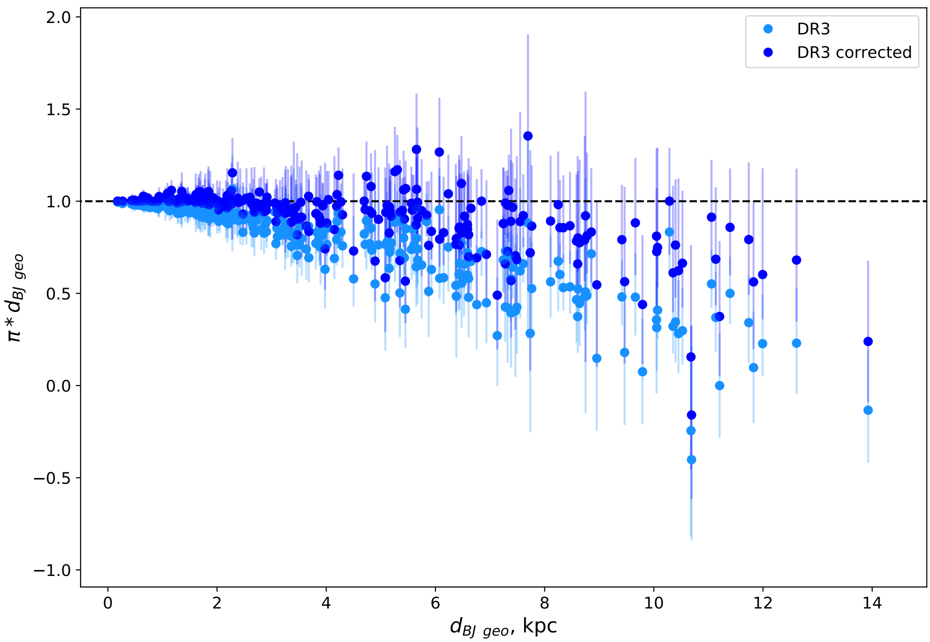

Figure 4: Comparison of parallax from Gaia EDR3 (light blue) and corrected Gaia EDR3 by Lindegren et al. (2021) (blue) with geometric distance from Bailer-Jones et al. (2021). The vertical axis shows the Gaia EDR3 parallax and corrected parallax multiplied by the geometric distance: values under 1 correspond to the parallax distance being bigger than the value of Bailer-Jones et al. (2021) distance and vice versa. The vertical error bars take into account the statistical uncertainties both on the parallax and the distance, but the horizontal error bars for the distance are not displayed.

Gaia photometry During the Gaia mission, the Gaia satellite was observing the sky in G, G_{BP} and G_{RP} photometric filters. G band is a wide filter that covers the range 330 - 1050 nm, G_{BP} and G_{RP} respectively 330 - 680 nm and 680 - 1050 nm in wavelength (see Tab.2). The transmissivity of the filters is shown in Fig.6. It changed with time: previous published sensitivity is shown in grey and nowadays colored with green: G; blue: G_{BP}; red: G_{RP}. The accuracy of Gaia photometry is good for bright sources. Stars in the data set are mostly in range $12 < G < 17$ mag therefore their uncertainties are less or equal 1 mmag (see Tab.3).

UBVIJHK photometry Photometry in UBVIJHK filters was collected from different sources in the literature. U is in the ultraviolet part of the spectrum; B, V is in visual; I, J, H, K are in near-infrared. U, B, V filters define the Johnson

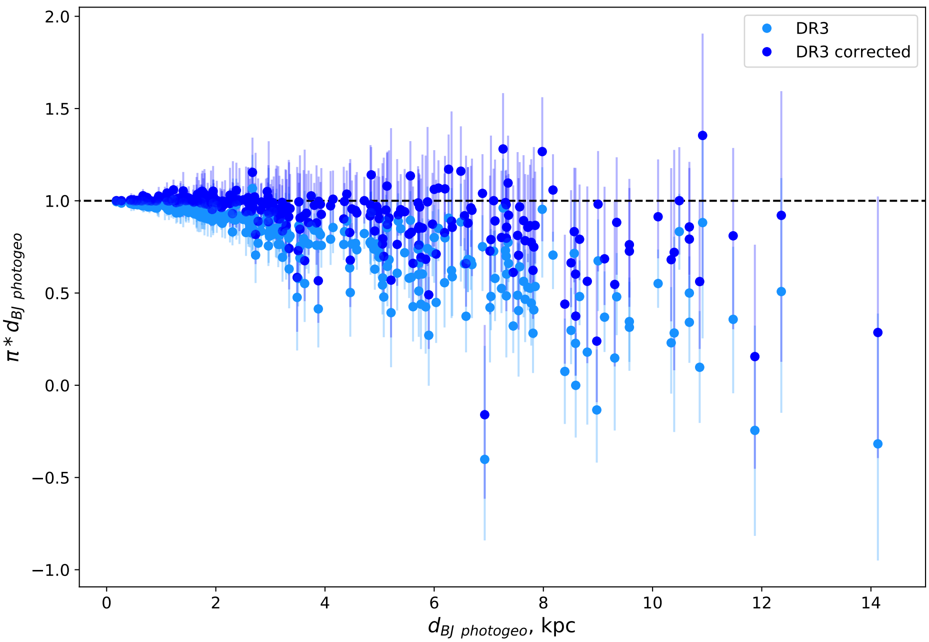

Figure 5: Comparison of parallax from Gaia EDR3 (light blue) and corrected Gaia EDR3 by Lindegren et al. (2021) (blue) with photogeometric distance from Bailer-Jones et al. (2021). The vertical axis shows the Gaia EDR3 parallax and corrected parallax multiplied by the photogeometric distance: values under 1 correspond to the parallax distance being bigger than the value of Bailer-Jones et al. (2021) distance and vice versa. The vertical error bars take into account the statistical uncertainties both on the parallax and the distance, but the horizontal error bars for the distance are not displayed.

Table 2: Characteristics of Gaia EDR3 filters

Passband	Wavelength range nm
G	330 - 1050
G_{BP}	330 - 680
G_{RP}	680 - 1050

Table 3: Uncertainties of Gaia Erly Data Release 3 photometry

Data product or source type	Typical uncertainty		
	$G < 13$	$G = 17$	$G = 20$
Mean G-band photometry, mmag	0.3	1	6
Mean G_{BP}-band photometry, mmag	0.9	12	108
Mean G_{RP}-band photometry, mmag	0.6	6	52

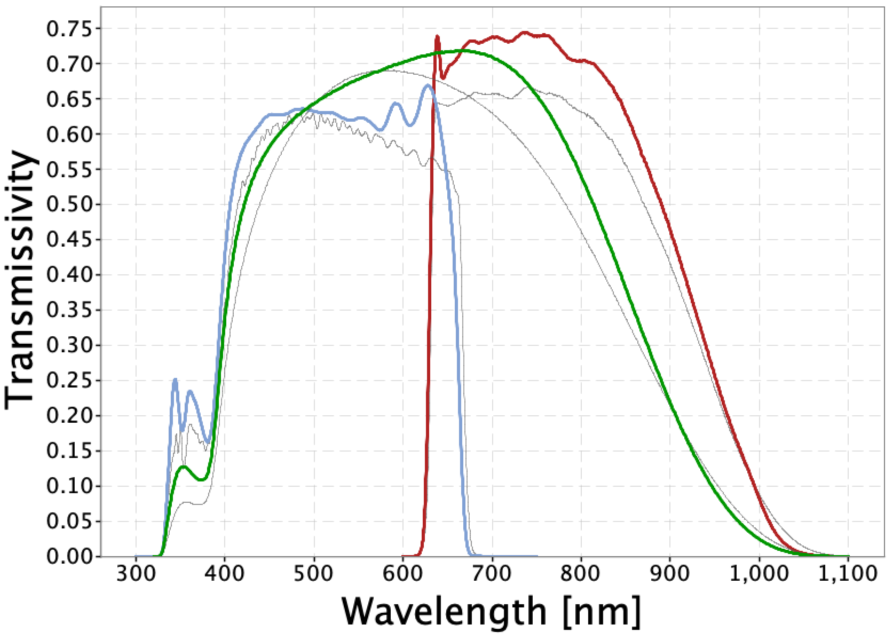

Figure 6: Transmissivity of Gaia EDR3 photometric filters. The coloured lines in the figure show the G, G_{BP} and G_{RP} passbands (green: G; blue: G_{BP}; red: G_{RP}). The thin, grey lines show the nominal, pre-launch passbands published in Jordi et al. (2010b), used for Gaia DR1. Gaia Collaboration (2021)

photometric system the first standardized photometric system (see Fig.7). The later photometric system was extended to the visual and infrared parts of the electromagnetic spectrum. Filter characteristics are shown in Tab.4.

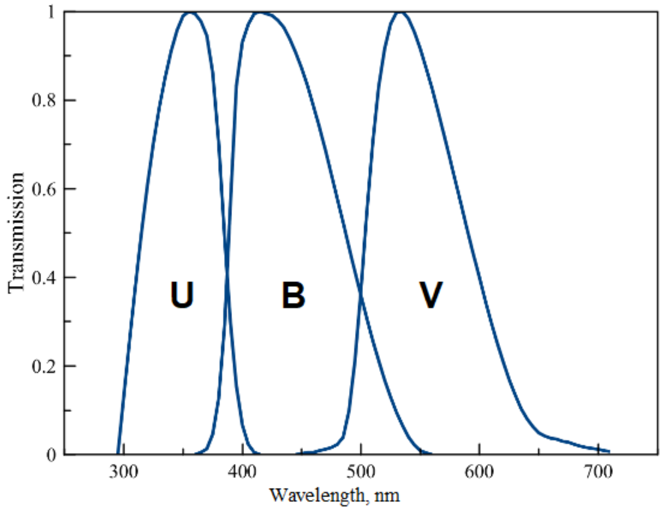

Figure 7: Transmissivity of Johnson photometric filters.

Table 4: Characteristics of UBVIJHK photometric filters

Filter	λ_{eff} nm	FWHM nm
U	365	66
G	445	94
B	464	128
V	551	88
R	658	138
I	806	149
J	1220	213
H	1630	307
K	2190	390

4.2.2 The resulting CMD

The resulting CMD in two photometric systems is presented in Fig.8 (Gaia photometry), Fig.9 (Johnson photometry). The data set has been cleaned by following criteria:

1. Parallax $\pi > 0.05$, only stars inside 20 kpc from the Sun are taken because after 20 kpc uncertainties represent more than 20% of the total parallax.

2. Uncertainty of the parallax measurement should be less than the parallax value $\Delta\pi < \pi$.

The top left diagram is CMD computed with Gaia EDR3 (light blue) and Gaia EDR3 corrected (blue) by Lindegren et al. (2021). The top right is CMD obtained with geometric (red) and photogeometric (yellow) distances from Bailer-Jones et al. (2021). The bottom diagram includes both top diagrams. We can see that stars that belong to the turn-off point are coinciding for all distances, instead, red giant branch (RGB) become more curved and tilted down in sequence (where distance in average is decreasing see Fig.4, 5): Gaia EDR3, Gaia EDR3 corrected, geometric, photogeometric, and curve that stars form is squeezed. In Johnson's photometric system for the previous sequence is becoming more evident that some stars lie out of the RGB to the fainter absolute magnitudes. This peculiarity is not present in the Gaia photometry diagram. That can tell us that made corrections for Gaia EDR3 parallaxes related to Gaia photometry have a bias based on Gaia EDR3 photometric uncertainties and is showing some incorrect results in other photometric bands such as B, V. In fact all mentioned before corrections (Lindegren et al. (2021), Bailer-Jones et al. (2021)) used Gaia EDR3 photometry as a parameter for their investigation.

Bailer-Jones et al. (2021) distances used as parameter in prior the corrected by Lindegren et al. (2021) Gaia EDR3 parallax that is why Bailer-Jones et al. (2021) distances are affected by Lindegren et al. (2021) correction uncertainties and over/underestimates. Although Bailer-Jones et al. (2021) distances work very well for nearby sources decreasing their uncertainties, for distant stars they show worse results. As they note: ”Poor data remain poor data”. In general, distances obtained by Bailer-Jones et al. (2021) are underestimated as shown in Bailer-Jones et al. (2021), Fig.8, 26, especially for low galactic latitude which is important for our data set where mostly all stars with poor parallaxes located in the red giant branch are from lower Galactic bulge (see Fig.10). Based on the facts that Bailer-Jones et al. (2021) distances produce in Johnson photometry CMD dotes which

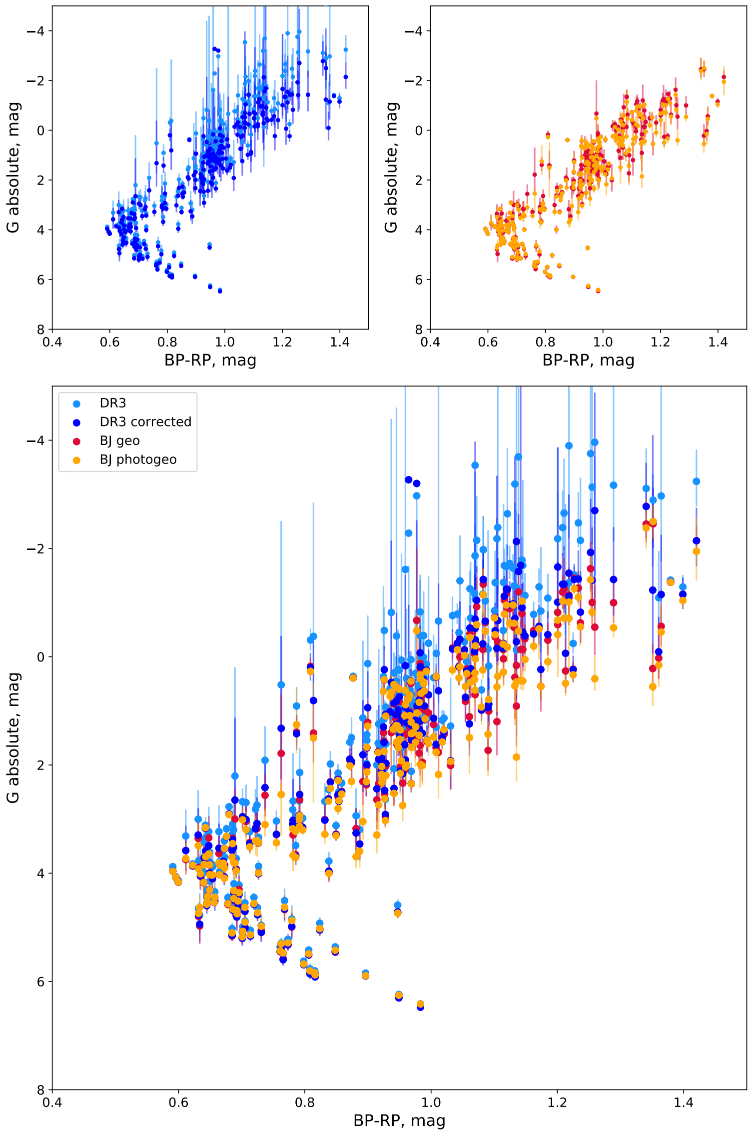

Figure 8: CMD in Gaia EDR3 photometry. The data set is cleaned by following criteria: (1) parallax $\pi > 0.05$, only stars inside 20 kpc from the Sun are taken, (2) uncertainty of the parralax measurment should be less than the parallax value $\Delta\pi < \pi$. *Left top*: absolute magnitude G is computed using parallax from Gaia EDR3 (light blue), Gaia EDR3 corrected by Lindegren et al. (2021) (blue). *Right bottom*: absolute G magnitude obtained by means of geometric (red) and photogeometric (yellow) distances from Bailer-Jones et al. (2021). *Bottom*: two *top* CMD combined together. The error bars are only due to distance uncertainties.

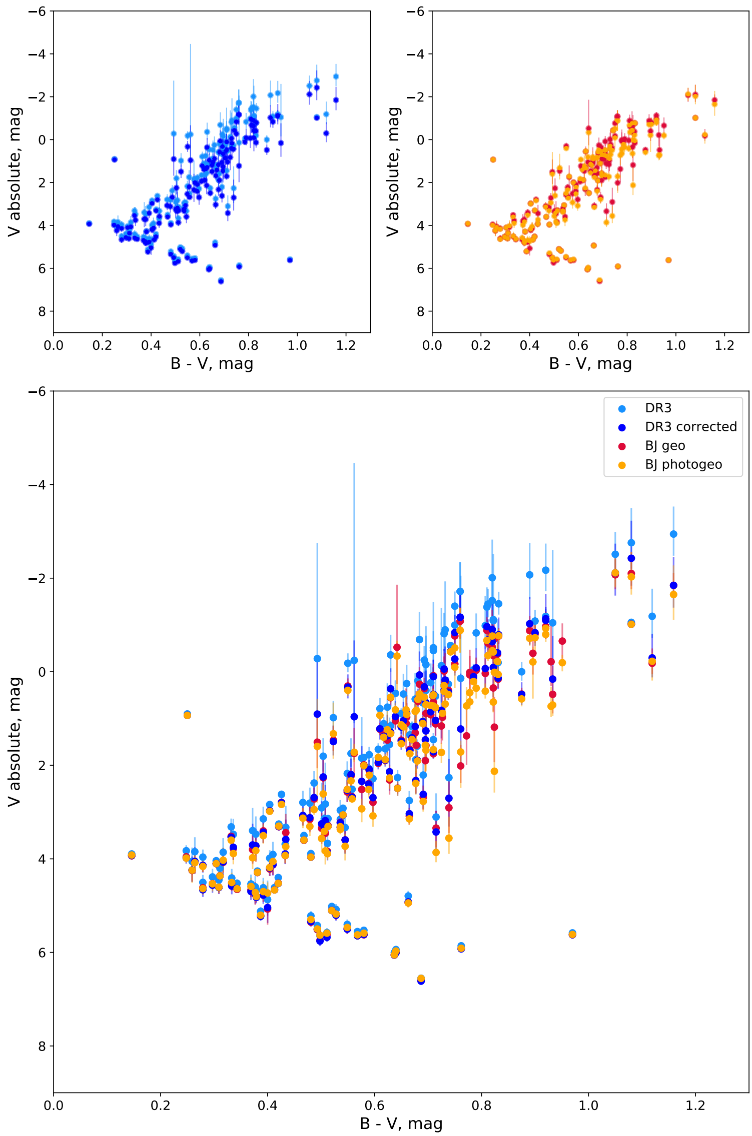

Figure 9: CMD in Johnson photometry. The data set is cleaned by following criteria: (1) parallax $\pi > 0.05$, only stars inside 20 kpc from the Sun are taken, (2) uncertainty of the parralax measurment should be less than the parallax value $\Delta\pi < \pi$. *Left top*: absolute magnitude V is computed using parallax from Gaia EDR3 (light blue), Gaia EDR3 corrected by Lindegren et al. (2021) (blue). *Right top*: absolute magnitude V obtained by means of geometric (red) and photogeometric (yellow) distances from Bailer-Jones et al. (2021). *Bottom*: two *top* CMD combined together. The error bars are only due to distance uncertainties.

are located far away from the red giant branch to the fainter part where no realistic stars can be present we exclude Bailer-Jones et al. (2021) distances from our investigation in the next part of the work.

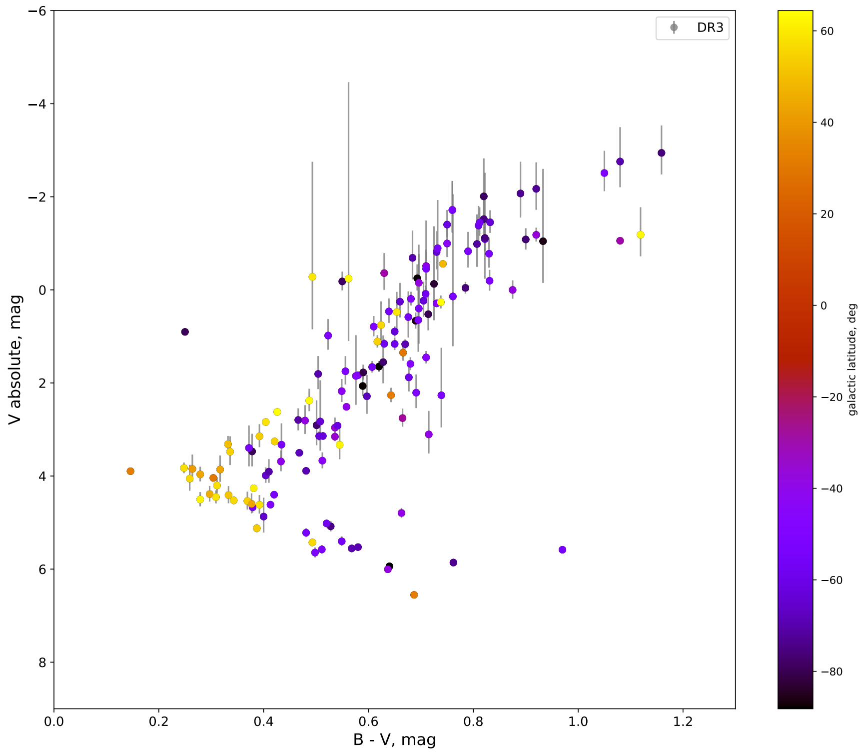

Figure 10: CMD in B, V photometric filters colored with galactic latitude.

In general, compare two photometric systems, data in Gaia photometric bands is more dispersed than in Johnson. On the other hand, Johnson photometry is an alternative source of information, uncertainties of Johnson photometry and Gaia EDR3 parallaxes have different nature and can help to unmask each other. Based on these arguments we assume Johnson photometry as the main sample and Gaia photometry is a testing one. Also due to big dispersion in Gaia photometry, it can not be used for isochrone fitting.

A deeper look at CMD built with Johnson photometry shows a clear evidence of a split in the turn-off point into two populations: bluer and redder. This separation is not clearly present in Gaia photometry, though. It is worth considering that separation in turn-off point in CMD is well explained with Galactic latitude

(Fig.10). Bluer population (yellow) is located at high Galactic latitude, while the redder (blue) is located at lower latitude. If we will look at the CMD in Gaia EDR3 photometry also colored with galactic latitude (Fig.11) we see the evident separation in the turn-off point region again to redder (blue) and bluer (yellow) populations. That means that the turn-off split has a physical origin and is not an artifact from photometric uncertainties in B, V filters. This peculiarity will be analysed further in the section 4.3.

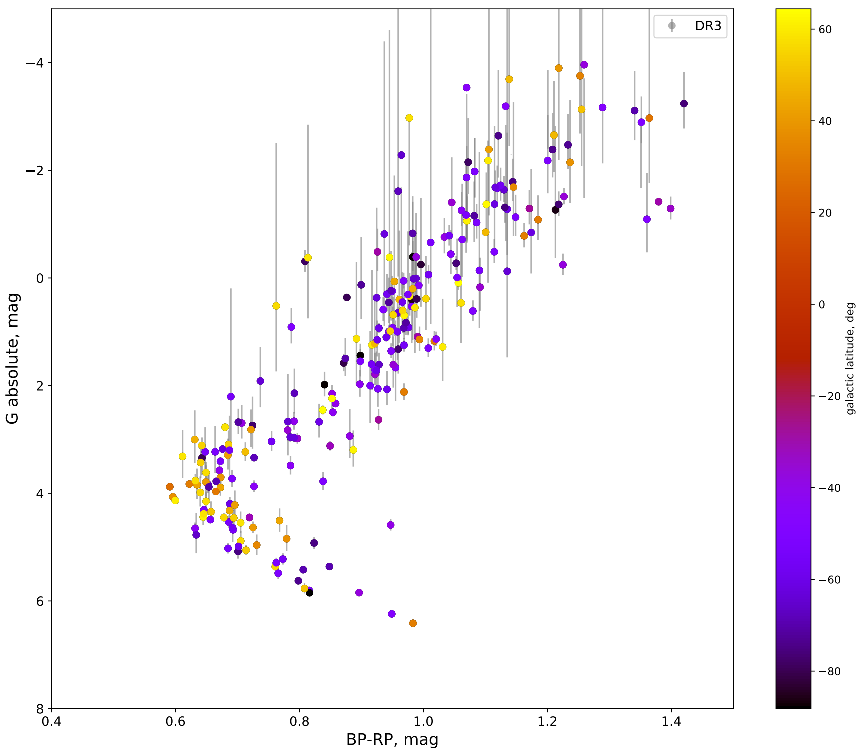

Figure 11: CMD in Gaia EDR3 photometric filters colored with galactic latitude.

4.3 Isochrone fitting

Initially, for deriving age, the isochrone fitting technique was used. Then the isochrones corresponding to the metallicity, α-abundance, He-abundance and different ages were plotted and their best fit provided us with the age of the population. Since the stars under investigation are very metal-poor we can assume they have close to each other age and they can be studied as a "star cluster" and therefore isochrones can be employed. For the isochrone fitting technique, two different sets of isochrone were used: Padova isochrones [2] and a suite of Stellar Tracks and Isochrones (BaSTI) (Hidalgo et al. (2018)) which used the most modern stellar models taking into account low metallicities. For Padova isochrones the low limit for metallicity is $\left[\frac{Fe}{H}\right] = -2.2$, for BaSTI $\left[\frac{Fe}{H}\right] = -3.5$. The choice for isochrone parameters was based on the characteristics of the stars (see section 3) and a prediction that due to their low metallicity they should be older than 10 Gyr.

4.3.1 Isochrones

Padova isochrones From Padova isochrones bank set of isochrones was downloaded with characteristics shown in Tab.5.

Table 5: Chosen characteristics for downloaded set of Padova isochrones.

Parameter	Choice
Age	10 - 15 Gyr with step 1 Gyr
$\left[\frac{Fe}{H}\right]$	-2, -2.2
Interstellar extinction	$A_V = 0$
Photometric system	UBVIJHK, Gaia EDR3

BaSTI isochrones From BaSTI, isochrones were downloaded with characteristics shown in Tab.6.

Table 6: Chosen characteristics for downloaded set of BaSTI isochrones.

Parameter	Choice
Age	10 - 15 Gyr with step 1 Gyr
$\left[\frac{Fe}{H}\right]$	-1.9, -2.2, -2.5, -3.2
Heavy element mixture	α-ehanced $\left[\frac{\alpha}{Fe}\right] = +0.4$
Available grids	He = 0.0275
Interstellar extinction	$A_V = 0$
Photometric system	UBVIJHK, Gaia EDR3

The fits of Padova and BaSTI isochrones for the chosen ranges in parameters for Johnson photometry are presented in Fig.12, 13, 14.

[2] http://stev.oapd.inaf.it/cmd

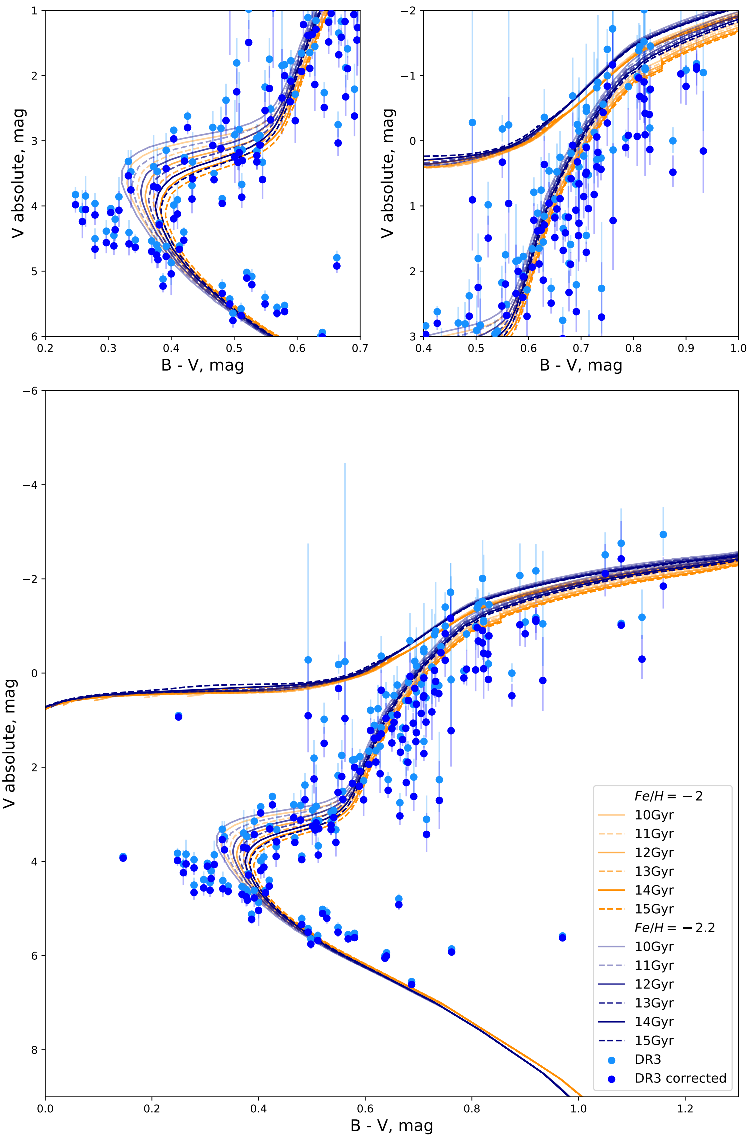

Figure 12: *Bottom*: CMD in Johnson photometry with Padova isochrones fit for $\left[\frac{Fe}{H}\right] = -2$ (orange), -2.2 (blue). The data set is cleaned by following criteria: (1) parallax $\pi > 0.05$, only stars inside 20 kpc from the Sun are taken, (2) uncertainty of the parallax measurement should be less than the parallax value $\Delta\pi < \pi$. *Left top*: Zoom of turn off point in CMD. *Right top*: Zoom of red giant branch in CMD.

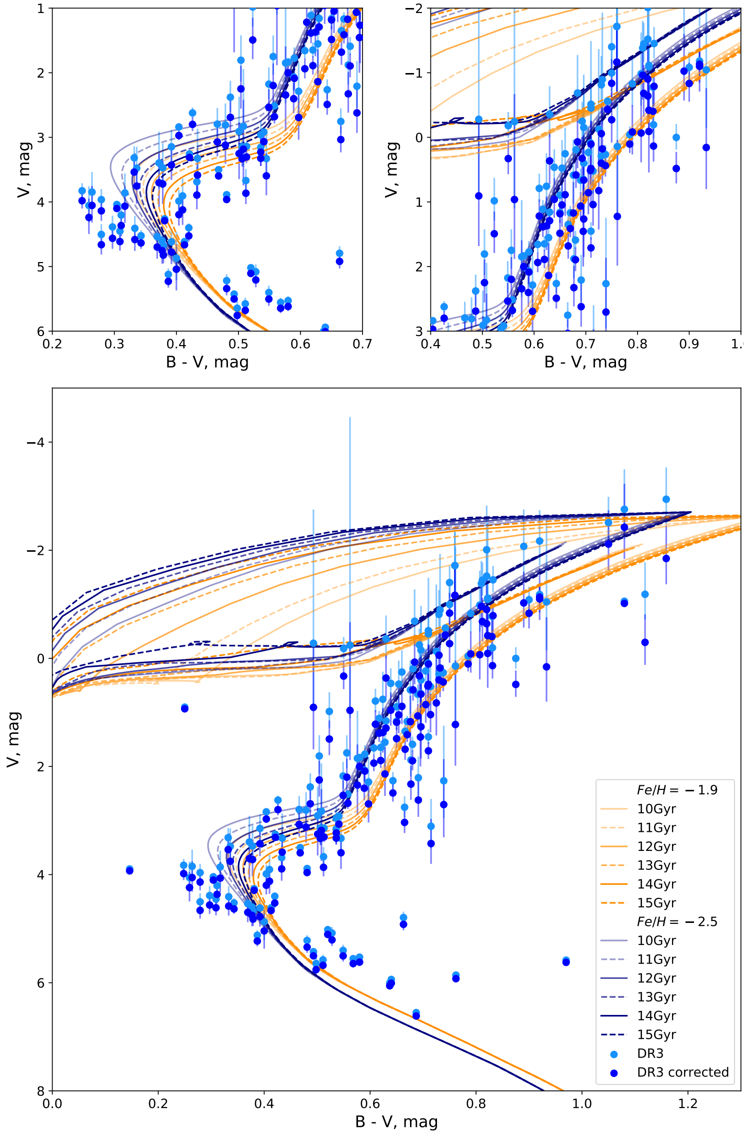

Figure 13: *Bottom*: CMD in Johnson photometry with BaSTI isochrones fit for $\left[\frac{Fe}{H}\right] = -1.9$ (orange), -2.5 (blue). The data set is cleaned by following criteria: (1) parallax $\pi > 0.05$, only stars inside 20 kpc from the Sun are taken, (2) uncertainty of the parallax measurement should be less than the parallax value $\Delta\pi < \pi$. *Left top*: Zoom part of turn off point in CMD. *Right top*: Zoom part of red giant branch in CMD.

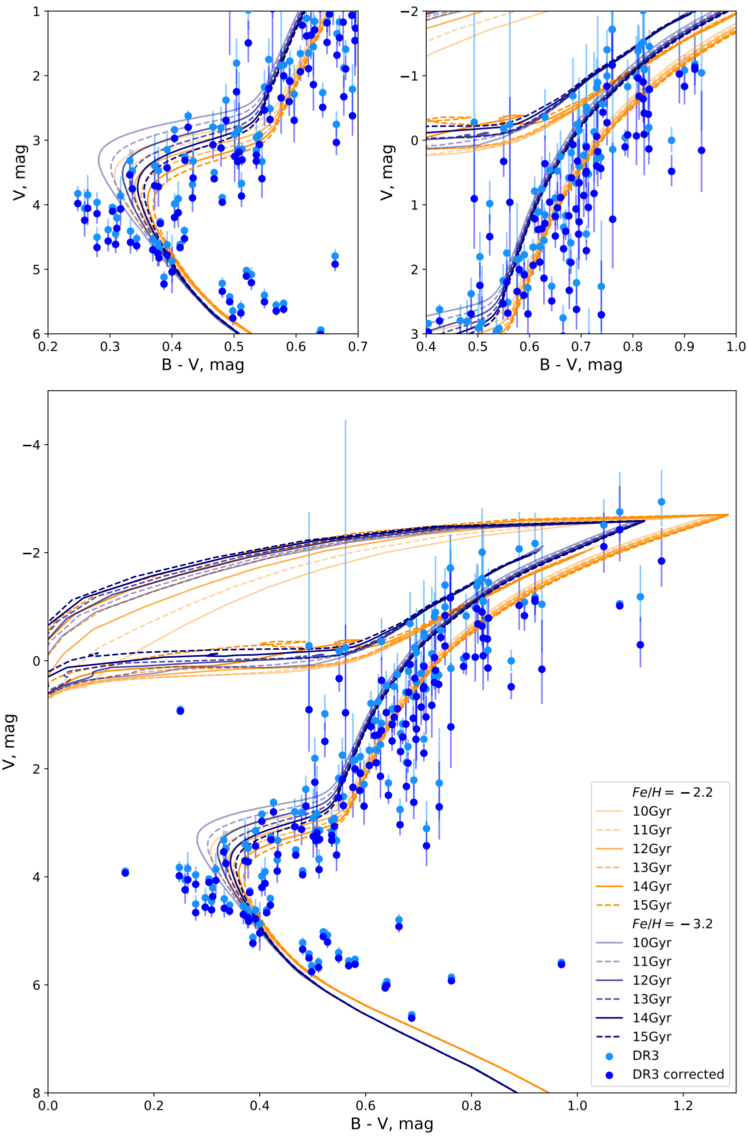

Figure 14: *Bottom*: CMD in Johnson photometry with BaSTI isochrones fit for $\left[\frac{Fe}{H}\right] = -2.2$ (orange), -3.2 (blue). The data set is cleaned by following criteria: (1) parallax $\pi > 0.05$, only stars inside 20 kpc from the Sun are taken, (2) uncertainty of the parallax measurement should be less than the parallax value $\Delta\pi < \pi$. *Left top*: Zoom part of turn off point in CMD. *Right top*: Zoom part of red giant branch in CMD.

The shapes of Padova and BaSTI isochrones were compared to see significant differences (see Fig.15). We can notice that in the turn-off point region BaSTI isochrones are shifted a little to the blue part of the diagram and their red giant branch is less curved. But in general, these data sets show good agreement.

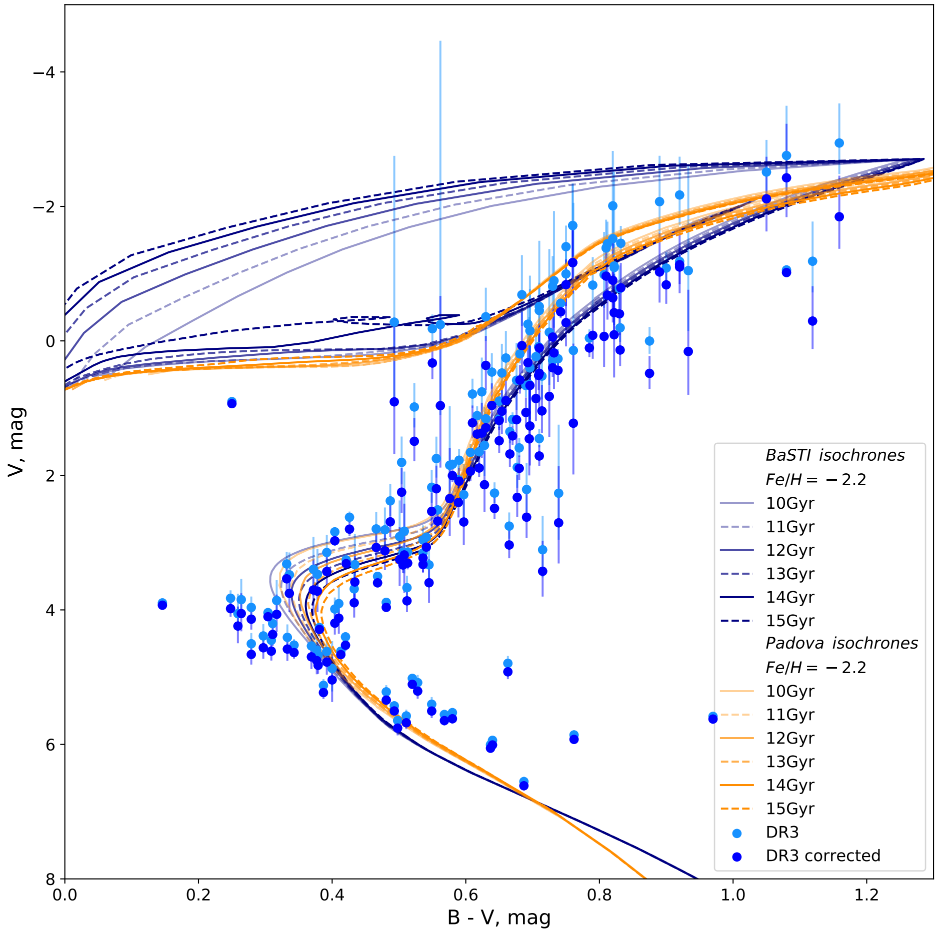

Figure 15: Comparison between fits of Padova and BaSTI isochrones ($\left[\frac{Fe}{H}\right] = -2.2$) for Johnson photometry.

To derive age in a most accurate way all parameters of isochrone should be defined accurately. There are three main characteristics that affect age determination with the isochrone fitting technique: (1) distance, (2) reddening, and

(3) metallicity. That is why a detailed consideration should be devoted to these characteristics to obtain a precise age.

4.3.2 Distance

From Fig.12, 13, 14 we can see the difference in shape between absolute magnitude obtained with Gaia EDR3 parallax and parallax corrected by Lindegren et al. (2021). The data set which was calculated with corrected Gaia EDR3 parallax is showing a more inclined red giant branch and squeezed total shape. This deviates from isochrone fits especially in the red giant branch (*top right* in Fig.12, 13, 14). That is why we chose to use as a main distance the distance obtained with original Gaia EDR3 parallaxes.

The exclusion of parallaxes corrected by Lindegren et al. (2021) is an additional argument to exclude Bailer-Jones et al. (2021) distances (see section 4.2.2) because as mentioned in Bailer-Jones et al. (2021) their distances inherit uncertainties from Lindegren et al. (2021) parallax correction. In fact zero-point corrected parallaxes were used as input parameters of their prior.

To sum up, incorrect distances are responsible for the unexpected location of stars below the red giant branch locus implied by their age and metallicity. Therefore, we consider as best distance estimates for our data set the original Gaia EDR3 parallaxes.

We also should mention that due to similar results for absolute magnitude in the turn-off point part (the most sensitive to the age part of CMD) from different distances, our resulting age estimates are not significantly affected by our choice of distance.

4.3.3 Reddening

From one side from isochrone fitting analysis, we saw that very metal-poor stars seem to be shifted to the red and faint part, which is typical reddening effect. But from the other side stars from the studied data set are located in the Galactic halo (for all stars $|b| > 20^o$). Galactic halo is poor in gas and dust and, as a consequence, it does not exhibit significant reddening. But to check it directly we used computed extinction values by means of `StarHorse` code (Queiroz et al. (2019)). They combined high-resolution spectroscopic data from APOGEE-2 survey Data Release 16 (DR16) with broad band photometric data from several sources, as well as parallaxes from Gaia Data Release 2 (DR2). The Bayesian isochrone-fitting code `StarHorse` was used to derive distances, extinctions and astrophysical parameters for around 388,000 APOGEE stars, achieving typical extinction uncertainties of about 0.07 mag, when all the photometric information is available. StarHorse uncertainties vary with the input spectroscopic catalog, with the available photometry, and with the parallax uncertainties. Data is available in https://gaia.aip.de/query/ in catalog: `gaiadr2_contrib.starhorse_v05` through IDQL query.

In Fig.16, 17 in blue shown the original data and in red corrected for reddening. Arrow show 0.5 of reddening vector. For both photometric systems reddening from `StarHorse` works mostly in the red giant branch. Due to bigger uncertainties in photometry and bigger difficulties in isochrone fitting stars corrected for reddening in the red giant branch become more disperse and destroy a clear picture of the population. For Gaia photometry reddening effect is more prominent because G and G_{BP} filters are taking bluer part of the spectrum (starts from 330 nm) compare with the B filter (starts from 464 nm) (see section 4.2) and G_{BP}, G_{RP} cover bigger range in wavelengths. For B, V photometric filters reddening is less present.

To check the accuracy of `StarHorse` correction in our data set we used color-color diagram $J - H/H - K$ where we collected all points which lie far away from the main sequence (Fig.18 - red dotes), most reddened stars according to J, H, K photometric filters. These stars are located in the upper part of the red giant branch (see Fig.17 green circles), which means that high extinction is not affecting stars in other parts of CMD.

Based on the following results: (1) disagreement `StarHorse` reddening correction and $J - H/H - K$ check in the low part of the red giant branch and bigger dispersion for data set under investigation, (2) location of the stars in Galactic halo, we decided to exclude reddening correction for next part of the work.

On balance, reddening is not significantly affecting turn-off point (the most sensitive to the age part of the CMD) in Johnson photometry and exclusion reddening correction does not affect the age determination procedure. And it is worth considering that split in turn-off point even described well with galactic latitude can not be explained with reddening.

4.3.4 Metallicity

Finally, to derive precise age metallicity should be chosen very close to the real one. That is why before age determination we did a deep analysis on metallicity. Fig.19 show CMD in Johnson photometry colored with metallicity, histogram show distribution in metallicity for two parts of CMD: red giant branch (RGB) absolute magnitude $V_{abs} < 2$ mag, turn-off point (TO) $V_{abs} > 2$ mag. The average metallicity of RGB is lower than for TO, and both parts show bimodal distribution. From metallicity analysis, we understand that Padova isochrones due to its lower

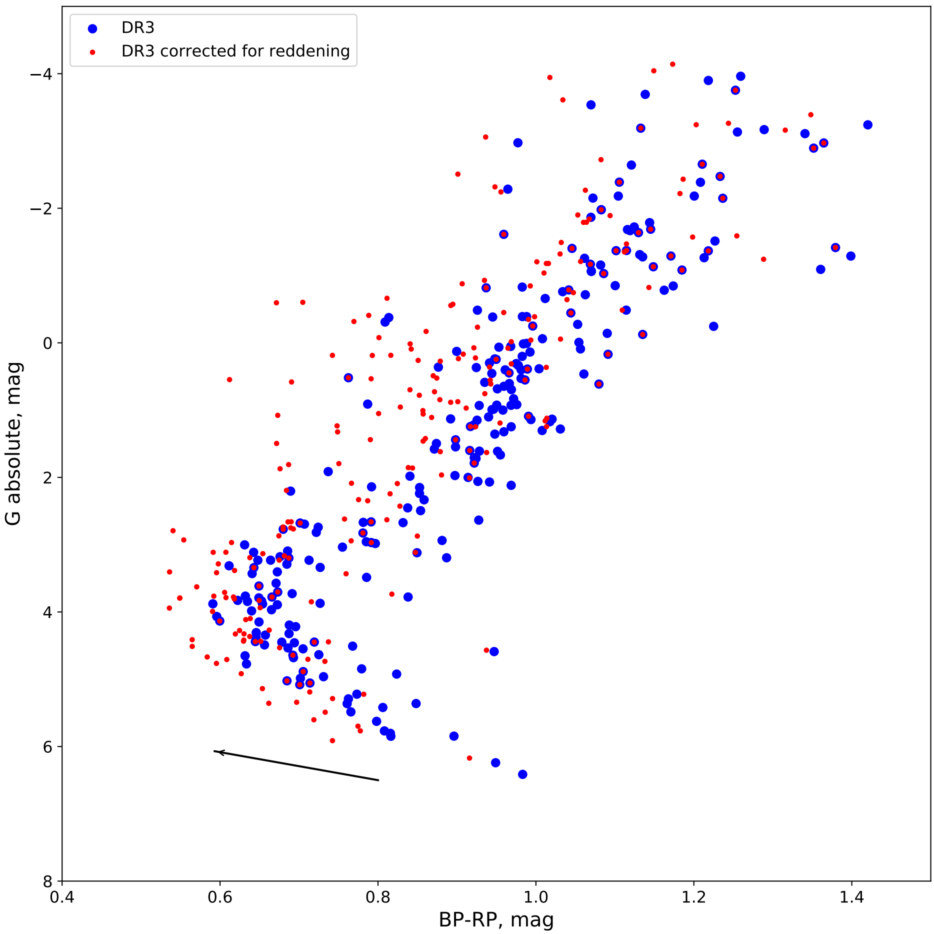

Figure 16: Comparison of original (blue) and corrected for reddening from StarHorse (red) data in Gaia EDR3 photometric filters. Arrow show 0.5 of reddening vector.

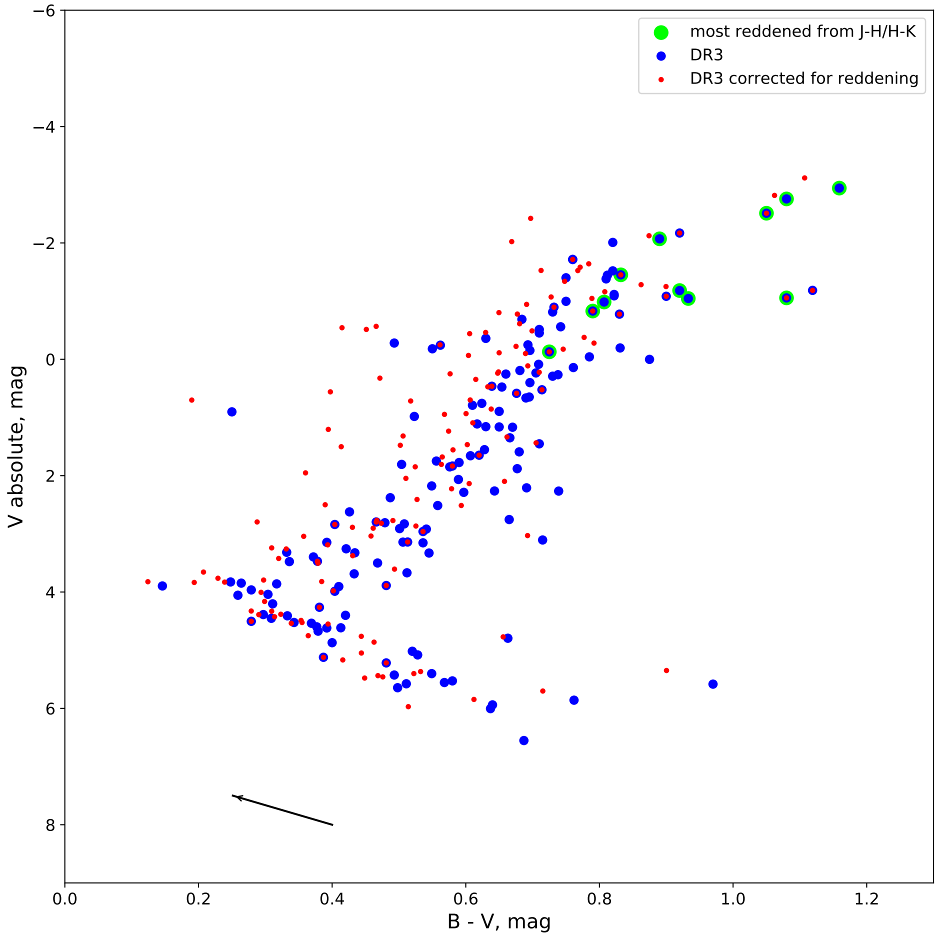

Figure 17: Comparison of original (blue) and corrected for reddening from StarHorse (red) data in B, V photometric filters. Arrow show 0.5 of reddening vector. Green circles highlight the most reddened stars from color-color diagram $J - H/H - K$.

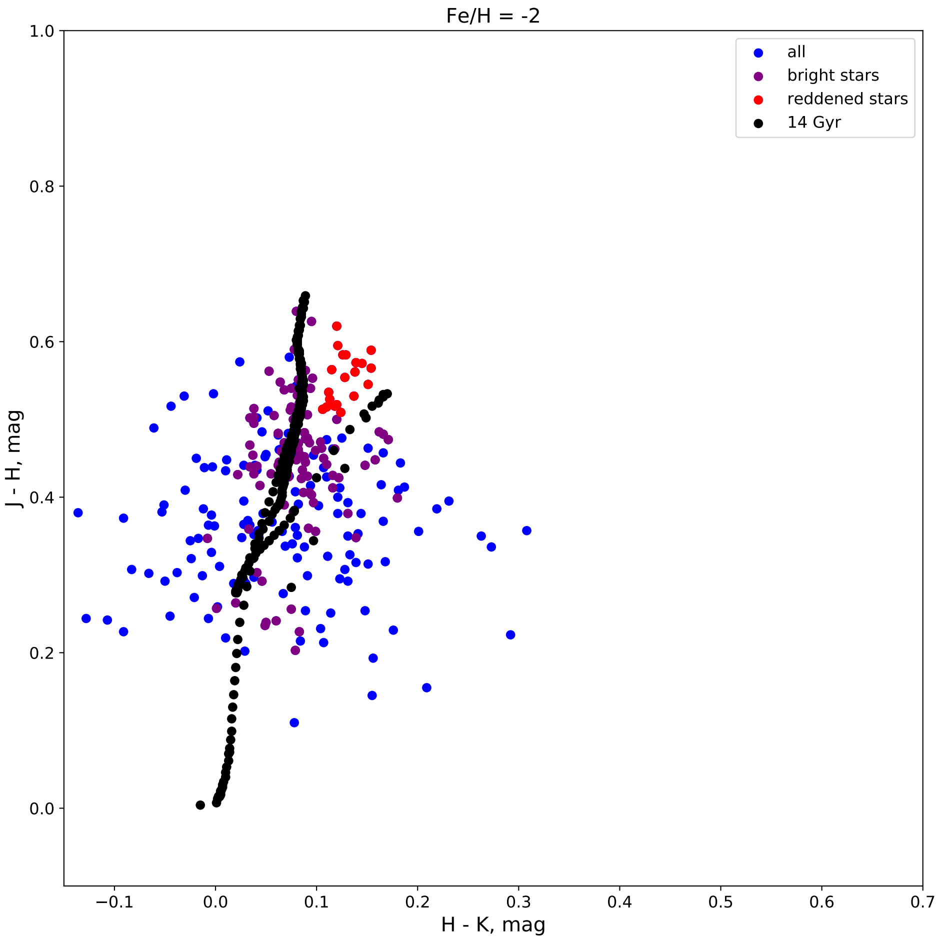

Figure 18: Color-color diagram where blue is all stars, violet is bright stars ($H < 13$ mag) and red is most reddened stars.

value $\left[\frac{Fe}{H}\right] = -2.2$ can explain only the more metal reach part of the data. BaSTI isochrones instead cover all range of metallicities.

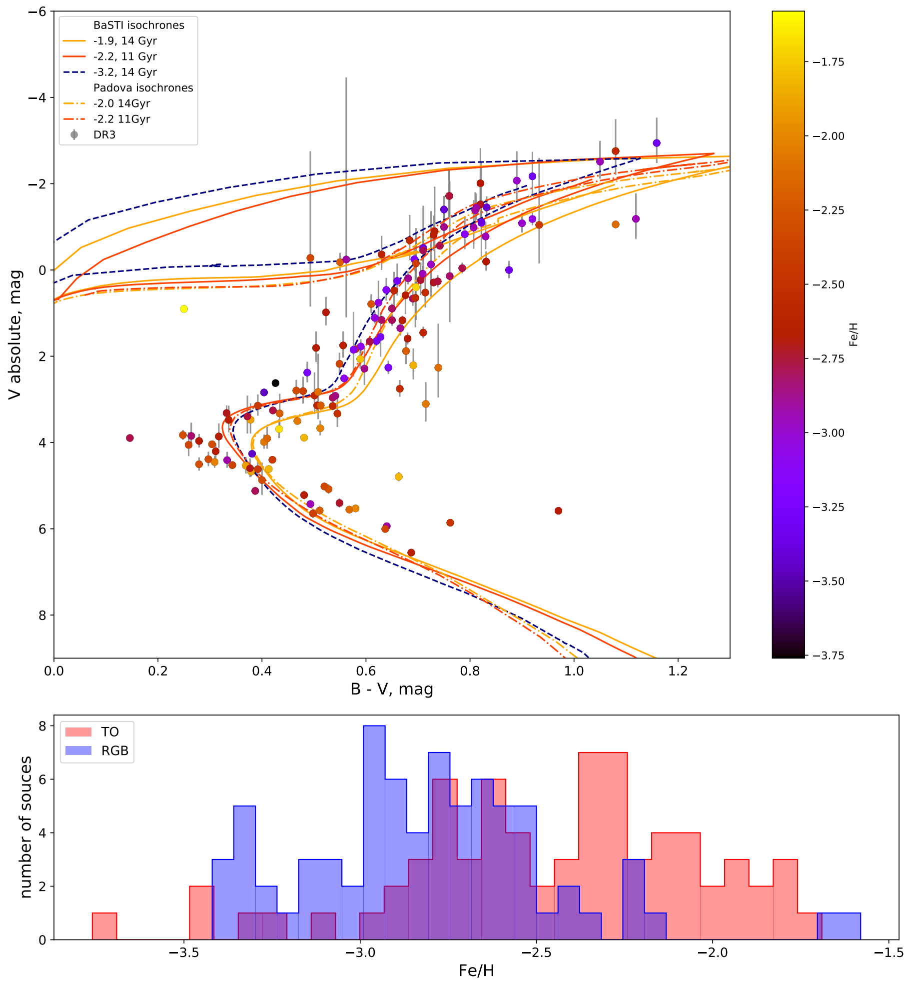

Figure 19: CMD in Johnson photometry colored with metallicity, histogram show distribution in metallicity for two parts of CMD: red giant branch (RGB) absolute magnitude $V_{abs} < 2$ mag, turn-off point (TO) $V_{abs} > 2$ mag. BaSTI isochrones show the best fit for groups with different metallicity.

We can divide data in three metallicity groups: $\left[\frac{Fe}{H}\right] \approx -2$ - orange, $\left[\frac{Fe}{H}\right] \approx -2.2 - -2.5$ - red, $\left[\frac{Fe}{H}\right] \approx -3.2$ - blue (see colors in Fig.19). For each group isochrones with corresponding metallicity were used.

4.3.5 Results

Because of the limited amount of data statistical analysis for deriving the best fit of isochrone can not be used. That is why the best fit was derived by eye-balling the star distribution in the CMD. We need to fit three groups with different metallicity.

Group with average metallicity $\left[\frac{Fe}{H}\right] \approx -2$ located mostly in the redder turn-off point with only few dotes in red giant branch. The best fit for this group taking into account its metallicity is 14 Gyr isochrone with $\left[\frac{Fe}{H}\right] = -1.9$ for BaSTI and $\left[\frac{Fe}{H}\right] = -2$ for Padova. This is very old but relatively metal-reach population.

Group with metallicity in range $\left[\frac{Fe}{H}\right] \approx -2.2 - -2.5$ populated bluer turn-off point and red giant branch. The best fit is 11 Gyr with metallicity $\left[\frac{Fe}{H}\right] = -2.2$ for Padova and BaSTI. This group is younger than the previous one but more metal-poor. An important feature of this group is that stars which lie on the blue side of the turn-off point and pretending to have younger ages (Fig.20). These stars are usually called Blue Stragglers.

The majority of the stars from the most metal-poor group $\left[\frac{Fe}{H}\right] \approx -3.2$ is present mostly in the red giant branch part that makes it difficult to define precise age. The turn-off point is the main indicator for age and we have just a few stars here. That is why the chosen best fit isochrone 14 Gyr with $\left[\frac{Fe}{H}\right] = -3.2$ is not accurate and give just an estimate.

All results are listed in Tab.7

Table 7: Results of isochrone fitting for three populations with different metallicity.

Group color	metallicity	age
	dex	Gyr
Orange	-2	14
Red	-2.2	11
Blue	-3.2	14

4.3.6 Split into 2 populations

As we discussed in previous sections in CMD in B, V photometric bands we see (Fig.9) the clear split into two populations: redder and bluer in color (B-V). Where redder population is fitted very well by 14 Gyr isochrone ($\left[\frac{Fe}{H}\right] = -2$) and bluer by 11 Gyr isochrone ($\left[\frac{Fe}{H}\right] = -2.2$). Another separation reason is galactic latitude. Bluer turn-off formed from the stars from the upper Galactic halo and

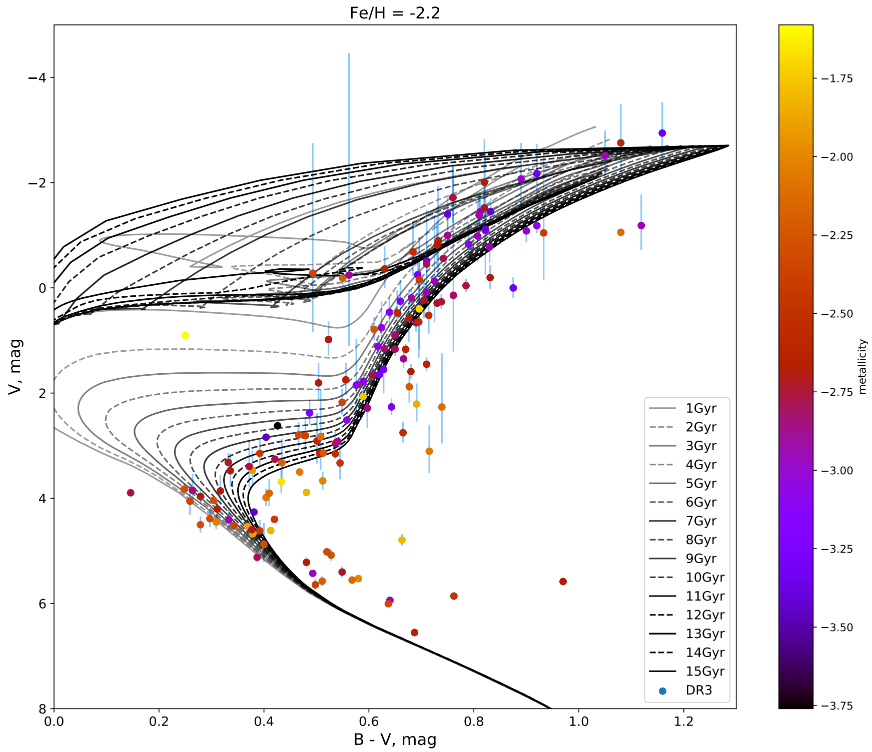

Figure 20: CMD in Johnson photometry with BaSTI isochrones for 1-15 Gyr. Dotes colored with metallicity.

redder from the lower Galactic halo. Correlation between galactic latitude, age and metallicity is shown in Fig21. We can say that stars in Galactic halo have on average the same metallicity for turn-off and red giant branch. Lower Galactic halo instead show a bigger spread and the turn-off point is significantly more metal-rich. That means that due to their difference in space location, age and metallicity characteristics they can have a different origin. To study it deeper we will work with kinematics in section 5.

4.4 Comparison with metal-poor globular clusters NGC 6397, M 30, M 92

We can perform an additional fit to check our isochrone fitting results. Three metal-poor globular clusters: NGC 6397, NGC 7099 (M 30), NGC 6341 (M92) were taken to use as a kind of observed isochrone. The characteristics of these globular

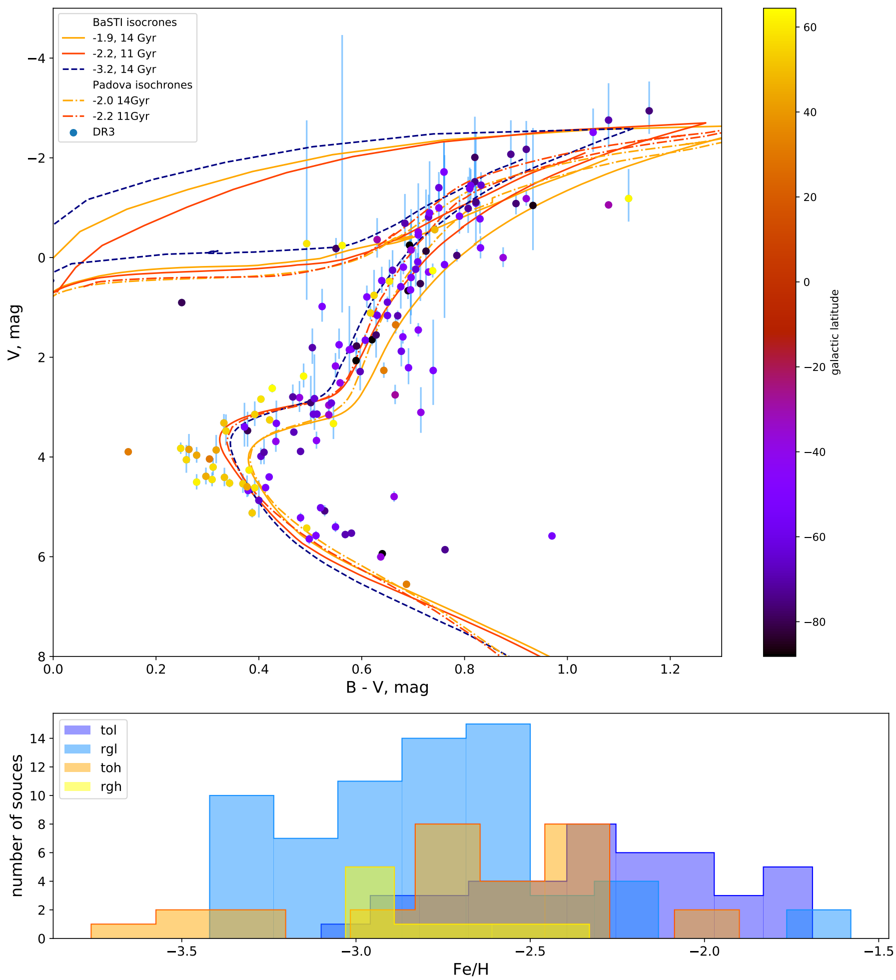

Figure 21: CMD in Johnson photometry colored with galactic latitude, histogram show distribution in metallicity separately for lower (blue) and upper (yellow) Galactic halo for two parts of CMD: red giant branch (RGB) absolute magnitude $V_{abs} < 2$ mag (lighter), turn-off point (TO) $V_{abs} > 2$ mag (brighter). BaSTI isochrones show the best fit for groups with different metallicity.

clusters are listed in Tab.8. Metallicities are taken as an average of results listed in the SIMBAD catalog[3]. Age was collected from Correnti et al. (2018) (NGC 6397), Kains et al. (2013) (M 30), VandenBerg et al. (2016) (M 92). Parallaxes for all of the used globular clusters are presented in Vasiliev & Baumgardt (2021). Reddening was estimated by the dust reddening map (Schlafly & Finkbeiner (2011)) based on the colors of stars with spectra in the Sloan Digital Sky Survey. The photometry in V and B passbands were taken from Stetson observations [4]. Gaia EDR3 photometry was downloaded from Gaia EDR3 and transformed from Johnson photometry. From Fig.22 we can see that the transformed Gaia photometry coincides with the direct one. Transformation was made from V-I color according to Tab.9 taken from Jordi et al. (2010a). All globular clusters are corrected for reddening and shifted with respect to the parallax. The fits were performed for Gaia EDR3 (Fig.23) and Johnson photometric systems (Fig.24).

Table 8: Globular cluster's parameters

Name	$\left[\frac{Fe}{H}\right]$ dex	age Gyr	⊠ mas	A_v mag
NGC 6397	-1.99	12.6	0.414	0.512
M 30	-2.3	13.0	0.132	0.140
M 92	-2.3	12.5	0.108	0.061

Table 9: Transformation coefficients fron V, I_c passbands to Gaia photometry Jordi et al. (2010a)

	a_0	a_1(V-I_C)	$a_2(\text{V-I}_C)^2$	$a_3(\text{V-I}_C)^3$	⊠
G-V	-0.0257	-0.0924	-0.1623	0.0090	0.05
G-G_{RVS}	-0.0138	1.1168	-0.1811	0.0085	0.07
G-G_{BP}	0.0387	-0.4191	-0.0736	0.0040	0.05
G-G_{RP}	-0.0274	0.7870	-0.1350	0.0082	0.03
V-G_{RVS}	0.0119	1.2092	-0.0188	-0.0005	0.07
V-G_{BP}	0.0643	-0.3266	0.0887	-0.0050	0.05
V-G_{RP}	-0.0017	0.8794	0.0273	-0.0008	0.06
G_{BP}-G_{RP}	-0.0660	1.2061	-0.0614	0.0041	0.08

From plots, we can see that globular cluster NGC 6397 is fitting the data set very well in the region of the main sequence, turn-off point, and subgiant branch

[3]http://simbad.u-strasbg.fr/simbad/sim-fbasic

[4]https://www.canfar.net/storage/list/STETSON/Standards

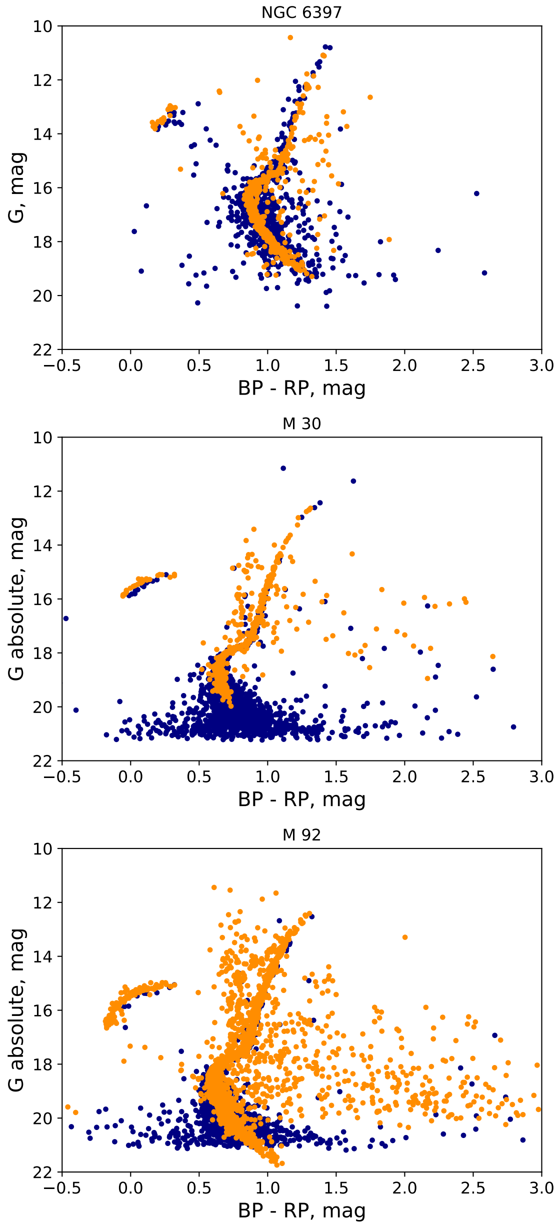

Figure 22: Comparison of photometric data from Gaia EDR3 and transformed from V, I_c to Gaia passbands with coefficients Tab.9

in both photometric systems (for B, V passbands NGC 6397 is fitting very well the redder population). But the red giant branch of this cluster is shifted more to the red part, in other words, the interval between the turn-off point and the red giant branch is bigger than for very metal-poor stars. That means that stars under investigation are older than the globular cluster NGC 6397 (12.6 Gyr). Which is in agreement with the isochrone result.

In Johnson photometry, the fit of globular cluster M 30 is close to the redder population of very metal-poor stars. Also, the interval between the turn-off point and the red giant branch is smaller (13 Gyr) and coincides with the data better. But still, it is some offset in the turn of the point that shows that the red population of data set in CMD in Johnson photometry is older than 13 Gyr, bluer population instead is younger.

In Johnson photometry, globular cluster M 92 shows a vertical shift out of the data. The sift in absolute magnitude is around 0.5 mag and the reason for it can be the wrong estimate of the distance.

Another feature that can be spotted is that the dotes which absolute magnitude obtained with Gaia EDR3 corrected by Lindegren et al. (2021) parallaxes show the more curved shape of the red giant branch with respect to globular cluster fits. The same behavior which the isochrone fitting technique showed. From this, we can make a conclusion that corrected Gaia EDR3 parallaxes are deforming the real shape of the population. Also Vasiliev & Baumgardt (2021) indicated that parallaxes resulting from Lindegren et al. (2021) correction are in average slightly overestimated around 0.005 - 0.01 mas. That result support again the idea that for this data set Gaia EDR3 original parallaxes are the best estimate for distance.

To sum up, globular clusters confirm isochrone fitting results in metallicity ranges and age determination.

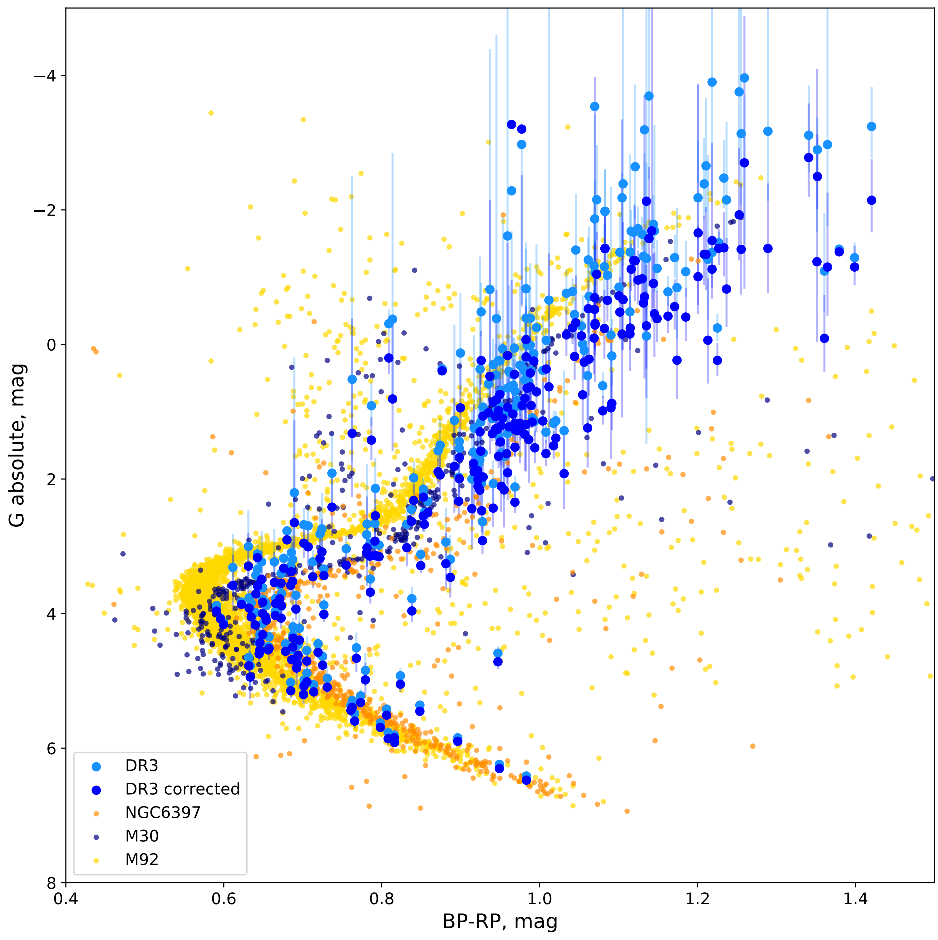

Figure 23: Fit of globular clusters: NGC 6397, M 30, M 92 with very metal poor stars for Gaia EDR3 photometry.

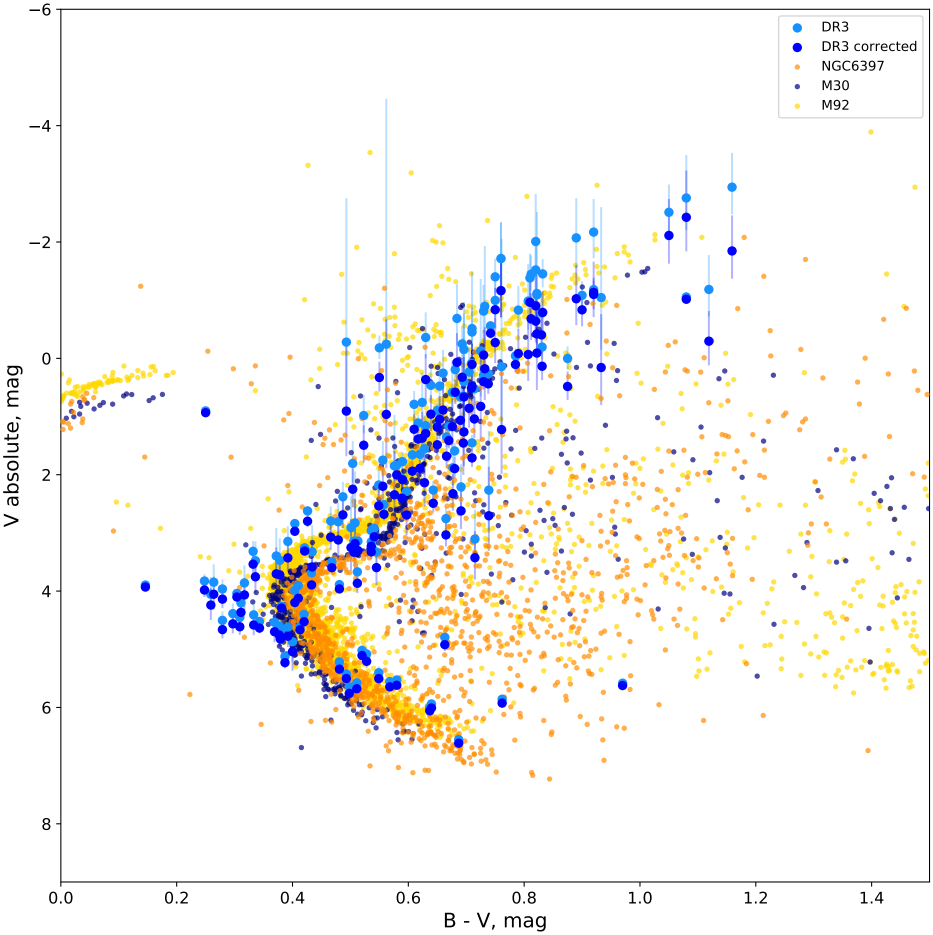

Figure 24: Fit of globular clusters: NGC 6397, M 30, M 92 with very metal poor stars for Johnson photometry.

5 Kinematics

Orbits and orbital parameters for all stars in the data set using distances (used for CMD), proper motion and radial velocities (Gaia EDR3) were found by numerical calculation in the Galactic potential. Different models of the gravitational potential of the Milky Way were used in this study especially with and without bar. Thereafter, using obtained data we derived origin whose kinematics is followed by these very metal-poor stars.

5.1 Data

For calculating orbital parameters coordinates, distance, radial velocity and proper motion need to be found. In section 4.3 we consider that according to the following results: (1) unreal location of stars lower than red giant branch for absolute magnitude obtained with corrected distances and (2) clear deviation (belting) of the red giant branch to fainter magnitudes compare with isochrones for different ages and metallicity, original parallaxes from Gaia EDR3 are the best estimate for distance modulus. Radial velocity and proper motion were taken from the Gaia EDR3 data bank. Uncertainties for velocity components are shown in Tab.10, 1. Position and velocity of the stars in the Equatorial Coordinates were transformed to Galactocentric coordinates.

Table 10: Uncertainties of Gaia Erly Data Release 3 proper motions

Data product or source type	Typical uncertainty, km s^{-1}		
	$G_{RVS} < 8$	$G_{RVS} = 10$	$G_{RVS} = 11.75$
Median radial velocity over 22 months	0.3	0.6	1.8
Systematic radial velocity errors	< 0.1	-	0.5

5.2 Models of the Galactic potential

In this research, we used two different models of Galactic potential: with and without bar structure. Stars under investigation are located in the halo and probably for the majority the bar potential does not show a big effect but some of them could reach the bulge region during their motion and be affected by bar potential.

5.2.1 Without bar

The first and simplest model consist three components: the central bulge, the plane disk and the spherical halo. All of them are described by time-independent, axisymmetric potentials. Total Galaxy potential is:

$$\Phi(r,z) = \Phi_b(R(r,z)) + \Phi_d(r,z) + \Phi_h(R(r,z)) \tag{4}$$

where $R = \sqrt{r^2 + z^2}$.

The model which was applied is a well-known Allen & Santillan (1991) potential which is build by a bulge, a disk and a halo. The form of the potential for the bulge and the disk are proposed by Miyamoto & Nagai (1975) and halo inside the R_0 is given by Allen & Martos (1986):

$$\Phi_b(R) = -\frac{M_b}{\sqrt{R^2 + b_b^2}}, \tag{5}$$

$$\Phi_d(r,z) = -\frac{M_d}{\sqrt{r^2 + (a_d + \sqrt{z^2 + b_d^2}}}, \tag{6}$$

$$\Phi_h(R) = \begin{cases} \frac{M_h}{a_h}\left(\frac{1}{\gamma-1} ln\left(\frac{1+\left(\frac{R}{a_h}\right)^{\gamma-1}}{1+\left(\frac{R_0}{a_h}\right)^{\gamma-1}}\right) - \frac{\left(\frac{R_0}{a_h}\right)^{\gamma-1}}{1+\left(\frac{R_0}{a_h}\right)^{\gamma-1}}\right) & \text{, if } R < R_0, \\ \frac{M_h}{R}\frac{\left(\frac{R_0}{a_h}\right)^{\gamma}}{1+\left(\frac{R_0}{a_h}\right)^{\gamma-1}} & \text{, if } R > R_0. \end{cases} \tag{7}$$

where M_b, M_d, M_h are the total masses of the bulge, the disk and the halo, R_0 is cut-off radius to avoid infinite mass of the halo. The b_b, a_d, a_h parameters control the scale of bulge, disk and halo component. The b_d limit the scale height of the disk. The constants are derived to be in good agreement with observational data such as: galactic rotational curve, local density and local surface density Yeh et al. (2020). All constants are listed in Tab.11.

5.2.2 With bar

To explore the orbits of the stars which spent a sufficient amount of time in the area of the bulge during their evolution the bar potential should be added to the previous model. Unlike the potential of the bulge, disk and halo component the bar potential is time-dependent. Ferrer's ellipsoid bar potential was adopted for

Table 11: Parameters for Galactic potential without bar. The Values are extracted from Tab.1 of Irrgang et al. (2013).

Parameter	Value
M_b, $10^{10}M_\odot$	0.950925
M_d, $10^{10}M_\odot$	6.6402
M_h, $10^{10}M_\odot$	2.36685
b_b, kpc	0.23
a_d, kpc	4.22
b_d, kpc	0.23
a_h, kpc	2.562
R_0, kpc	200
γ	2
Constraints	Observed
V_r	see Bhattacharjee et al. (2014)
$\rho_\odot$	0.102±0.01
$\Sigma_{1.1}$	74±6

this model. From observational data, we know that bar rotates clockwise around the Galactic center but the angular velocity value is very uncertain. Different observational methods and models give angular momentum in range $40 < \Omega < 70$ km s^{-1} kpc^{-1}. Another important difference from the bulge, disk and halo potential is that the potential of the bar component is triaxial, dependent on θ. For orbital calculations, the bar potential is added with assumption that all of the bulge mass transferred directly to the bar component instantly.

The density of triaxial Ferrer's bar is given by

$$\rho(x, y, z) = \begin{cases} \rho_c(1 - m^2)^2 & , \text{if } m < 1, \\ 0 & , \text{if } m > 1, \end{cases} \tag{8}$$

where $\rho_c = \frac{105}{32\pi}\frac{GM_{bar}}{abc}$, M_{bar} is the total mass of the bar transferred from the mass of the bulge, $m = \frac{x^2}{a^2} + \frac{y^2}{b^2} + \frac{z^2}{c^2}$. The a, b, c parameters are the semi-axis of the elipsoidal bar with $a > b > c > 0$. According to Pichardo et al. (2004), the major axis half-length $a = 3.14$ kpc, and the axis ratio $a : b : c = 10 : 3.75 : 2.56$. Based on Bovy et al. (2019), the present position angle of the longest axis of the bar with respect to the line of sight is 25^o.

According to Chandrasekar(1969, p.53) the potential of the bar for Eq.8 is expressed as:

$$\Phi = -\pi Gabc\frac{\rho_c}{n+1}\int_{\lambda}^{\infty}\frac{du}{\Delta(u)}(1-m^2(u))^3, \text{ where} \tag{9}$$

$$m^2(u) = \frac{x^2}{a^2+u} + \frac{y^2}{b^2+u} + \frac{z^2}{c^2+u}, \text{ and} \tag{10}$$

$$\Delta^2(u) = (a^2+u)(b^2+u)(c^2+u). \tag{11}$$

λ is the positive solution of $m^2(u) = 1$ such that outside the bar $\Phi = 0$. Iside the bar $\lambda = 0$. All bar parameters are listed in Tab.12.

Table 12: Parameters for Galactic potential with bar. The Values are extracted from Tab.1 of Irrgang et al. (2013), Bovy et al. (2019), Pichardo et al. (2004).

Parameter	Value
M_bar, $10^{10} M_\odot$	0.950925
M_d, $10^{10} M_\odot$	8.9015
M_h, $10^{10} M_\odot$	2.66573
b_b, kpc	0.27
a_d, kpc	6.21
b_d, kpc	0.33
a_h, kpc	2.39
R_0, kpc	200
a, kpc	3.14
Ω, km s^-1 kpc^-1	41
γ	2

5.3 Calculation

The Gauss-Radau spacings of 15th order with $(\Delta t)^{16}$ was chosen as an algorithm for computing orbits and orbital parameters. Among different algorithms, Gauss-Radau spacings improves integration accuracy greatly by considering forces at specific spacing within the entire time step. This method allows to use large time steps and therefore reduces the computational time.

Orbits and orbital parameters were calculated backward in 5 Gyr with 5000 steps for Galactic potential without bar and with 500 steps for Galactic potential with bar.

As a result of the numerical calculation in the Galactic potential orbits and following orbital parameters were obtained: angular momentum L_z (averaged over the time for bared potential $< L_z >$), the total energy of the star (sum of kinetic and potential energy), eccentricity e, perigalactic/apogalactic distances R_{min}/R_{max} (the closest/farthest point of the orbit to the Galactic center in the projection to the Galactic plane), the maximum height under the Galactic plane z_{max}. Thereafter all these kinematics needed to be studied deeper to relate the part of the Galaxy to the star according to its motion. For this purpose, several techniques of separation were used.

5.4 Separation by orbit

The first and foremost technique is based on the shape of the orbit of an individual star. Bajkova et al. (2020) shown for globular clusters that the shape of the orbit marks the part of the Galaxy whose kinematics an object is following. Consequently, separating orbits according to criteria which Bajkova et al. (2020) demonstrated, we can define the origin of our stars. Three main groups of orbits can be defined from Bajkova et al. (2020): bulge/bar, thick disk and halo (see Fig.25).

The classification of the orbits was done separately for (x,y) and (r,z) Galactic projections and for two different potentials: with and without bar. For each plane and potential, we derived three main groups according to Bajkova et al. (2020): bar/bulge, disk, halo and one group of unknown orbits where all unreal trajectories are collected. Defined groups are presented in Fig.26. The bar/bulge main orbital characteristics in (x,y) is a ring structure where the inner radius is much smaller than outer radius $R_{min} \ll R_{max}$; in (r,z) for barred potential is a rectangle that turns into a circle sector. The disk typical features of the orbit in (x,y) is a ring which inner and outer radii are close to each other $R_{min} \precsim R_{max}$; in (r,z) is a trapezoid which longer base look to the positive direction of r. The halo main orbital shape in (x,y) is small circles that intersect with bigger ovals; in (r,z) is curved lobes looking towards z positive and negative directions and crossing them big arc directed to the positive r. On balance we separate stars into four groups: the bar/bulge, the disk, the halo and unknown (where all unreal trajectories are collected). For different Galactic projections efficiency of separation is different due to similarities of the shapes for different groups. For example, in (x,y) plane bar/bulge and disk orbits in some cases have a similar ring shape, in (r,z) - bulge and disk have a similar trapezoid shape. But in general separation results are consistent with each other.

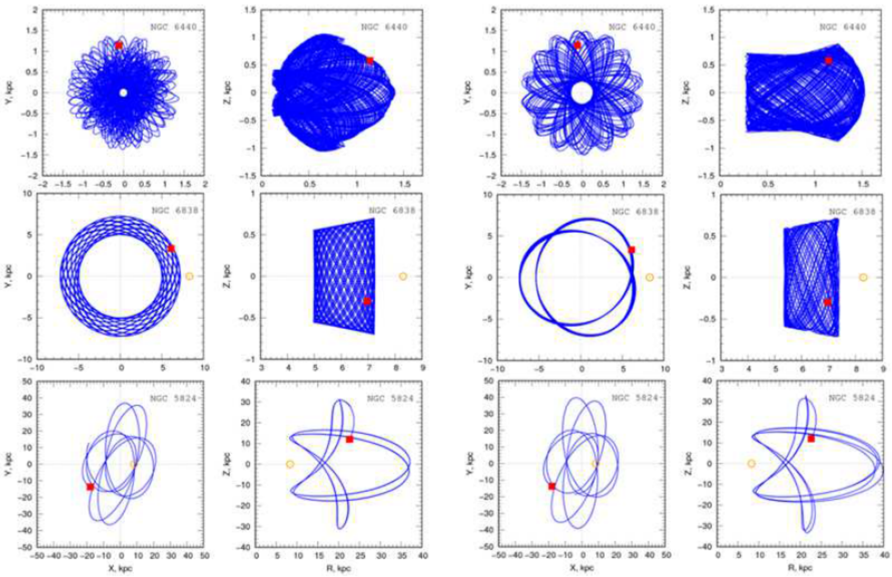

Figure 25: Orbits of NGC 6440 (*top line*), NGC 6838 (*middle line*), and NGC 5824 (*bottom line*) belonging to the bar/bulge, the thick disk, and the halo respectively, obtained in the axisymmetric potential (*two left-hand columns*) and in a barred potential (*two right-hand columns*). Red dote is a position of the star nowadays. Bajkova et al. (2020)

To check separation by orbit other separation methods and tests should be done.

5.5 Check of separation by orbit with orbital parameters

5.5.1 E/L_z diagram

The same study with separation by orbits Bajkova et al. (2020) showed for globular clusters that objects from the different origins are located in E/L_z diagram in specific places.

According to separation by orbit, all stars were colored in four groups: bar/bulge (purple), disk (blue), halo (light blue), unknown (black). It is worth considering although we call some stars as bulge stars none of them are really bulge stars because for all stars apogalactic distance is lying outside bar/bulge space. The minimum perigalactic distance for our stars is $\min(R_{max}) \approx 7$ kpc which is much less than the criterion used by Bajkova et al. (2020) to identify stars as a bulge/bar

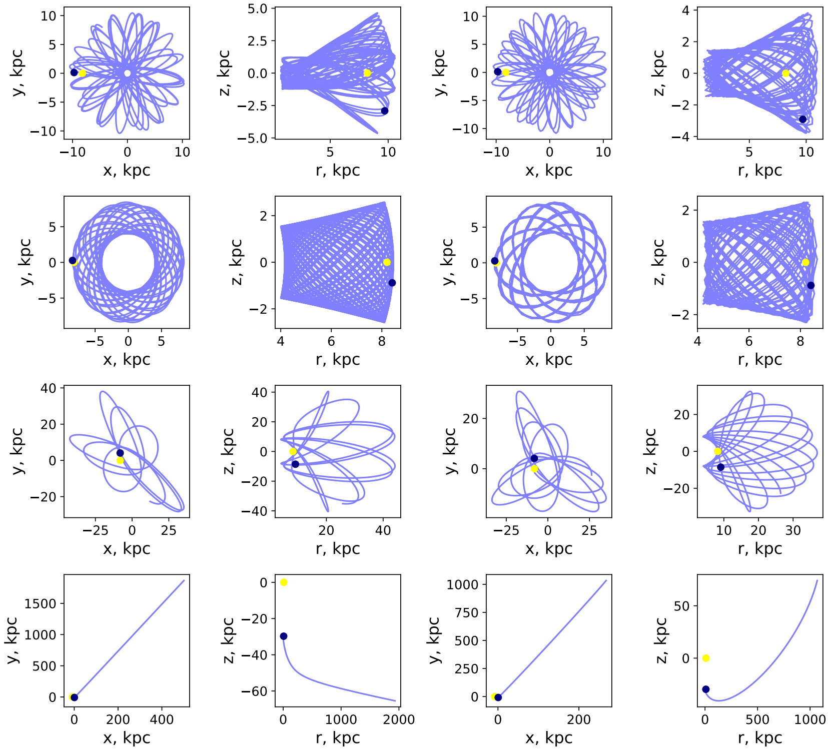

Figure 26: Orbits belonging to the bar/bulge, the thick disk, the halo and unknown groups respectively, obtained in the axisymmetric potential (*two left-hand columns*) and in a barred potential (*two right-hand columns*). Blue dote is a position of star nowadays, yellow dote is the Sun.

stats $R_{max} < 3.5$ kpc. In reality, these stars' kinematics only affected by bar/bulge gravitational potential.

In Fig.28 colored stars show clear separation into groups: bar/bulge, disk and halo showing the same result as Bajkova et al. (2020) obtained. Disk stars populate left and right borders of the cone bulge and halo stars are dispersed around $L_z = 0$ axis.

5.5.2 $\frac{L_z}{e}$ distribution

The last method which Bajkova et al. (2020) proposed to separate disk and halo stars is bimodality in distribution of ratio of angular momentum along z direction and eccentricity $\frac{L_z}{e}$. In our case disk and halo population overlap each other but

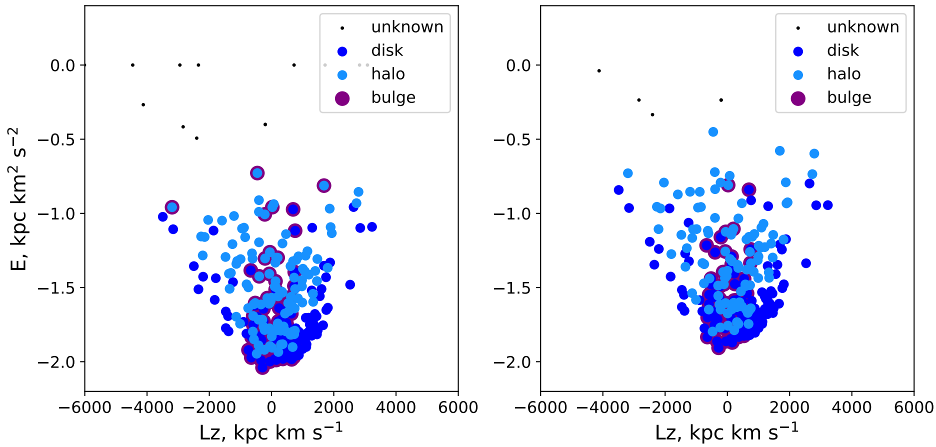

Figure 27: Relationships between the total energy E versus angular momentum along z direction L_z in axisymmetric (*first row*) and barred (*second row*) potentials for all stars colored according to orbits separation with criteria.

peacks are clearly separated and show similar values as Bajkova et al. (2020) showed for halo $L_{z\,peak} \approx 0$ kpc km s$^-1$, for disk $L_{z\,peak} \approx 1000$ kpc km s$^-1$ (see Fig.30).

5.5.3 L_z/e diagram

Another testing technique is L_z/e diagram. Yeh et al. (2020) demonstrated that the location in L_z/e diagram can not precisely tell us the origin of the star but can be used as a test.

Fig.31, 32 show the distribution of angular momentum L_z in relationship with eccentricity e. It is clearly seen that very metal-poor stars exhibit both prograde and retrograde motion and have mostly elongated orbits. Also, we can see that disk stars on average have higher angular momentum than halo stars and halo stars are more dispersed. High eccentricity and low angular momentum tails are possibly explained due to the bulge/bar potential effect. Collisions with high-density clouds in the bulge region help to lose angular momentum and increase eccentricity.

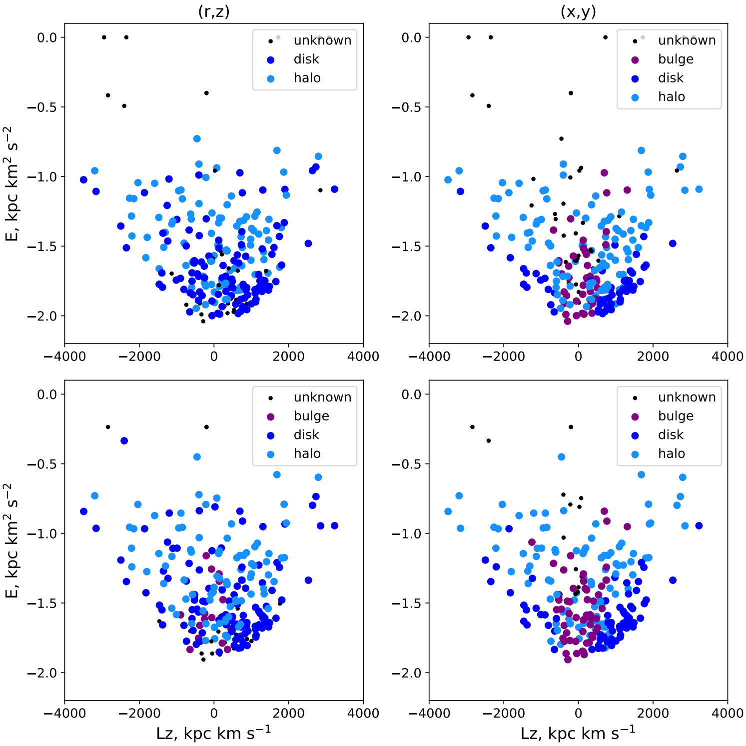

Figure 28: Relationships between the total energy E versus angular momentum along z direction L_z in axisymmetric (*first row*) and barred (*second row*) potentials for all stars colored according to orbits separation in (r,z) plane (*left column*), in (x,y) plane (*right column*).

5.5.4 Borders of the orbits

Also as a consequence of the spherical symmetry of the halo potential we can predict that stars belonging to the halo have a maximum height which is equal or close to the apogalactic distance $z_{max} \approx R_{max}$. For the disk stars instead $R_{max} \gg z_{max}$. R_{min} orbital parameter can mark the effect of the bulge potential showing attendance of the star in the Galactic bulge. Consequently, diagrams z_{max}/R_{min}, z_{max}/R_{max}, R_{max}/R_{min} can be used for checking separation into groups.

In Fig.35, 37, 39 we can see following pattern: (1) orbits affected by bulge have low perigalactic distance ($R_{min} < 2$ kpc); (2) it is clear separation between disk and halo stars in z_{max}/R_{max} plane, there $\frac{z_{max}}{R_{max}} \approx 0.75$

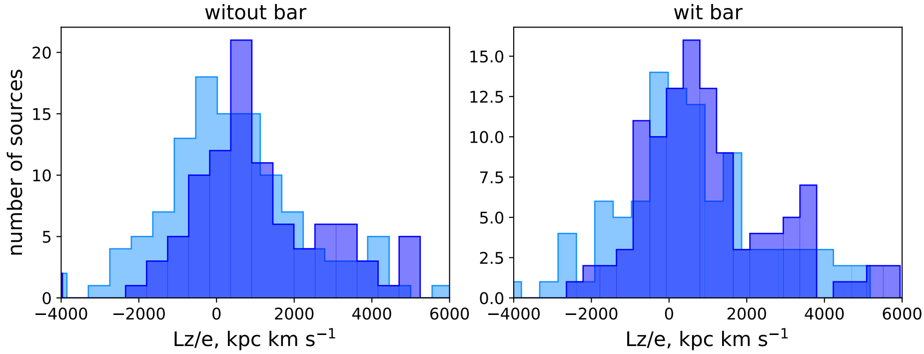

Figure 29: Distribution of the ratio of angular momentum along z direction L_z and eccentricity e for the disk (blue) and the halo (light blue) separated with criteria in axisymmetric (*left*) and barred (*right*).

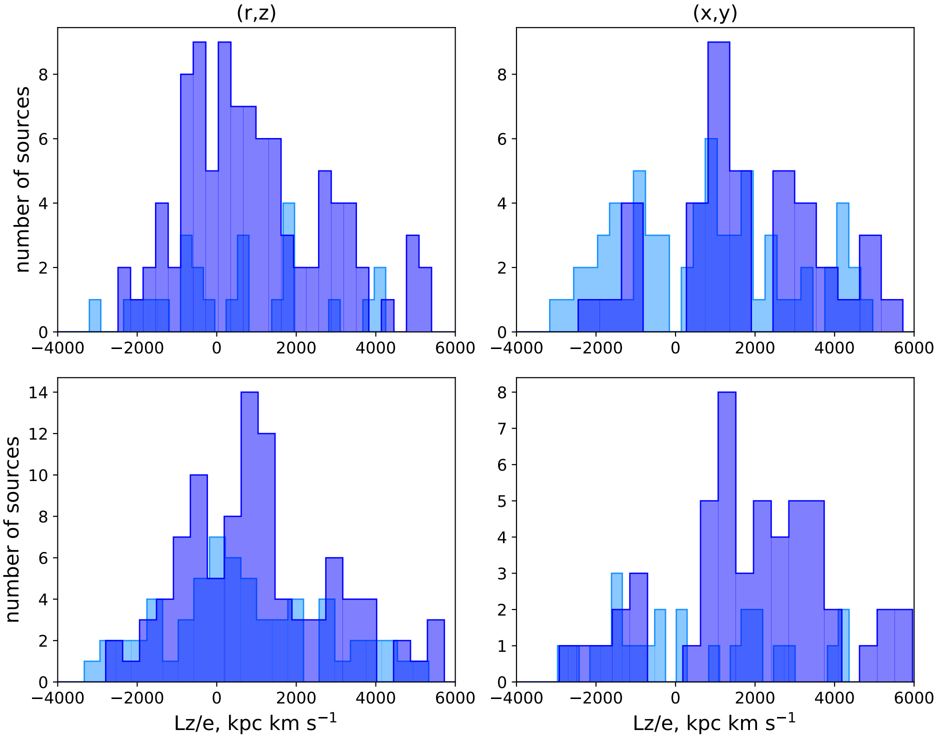

Figure 30: Distribution of the ratio of angular momentum along z direction L_z and eccentricity e for the disk (blue) and the halo (light blue) separated by orbit in axisymmetric (*top row*) and barred (*bottom row*).

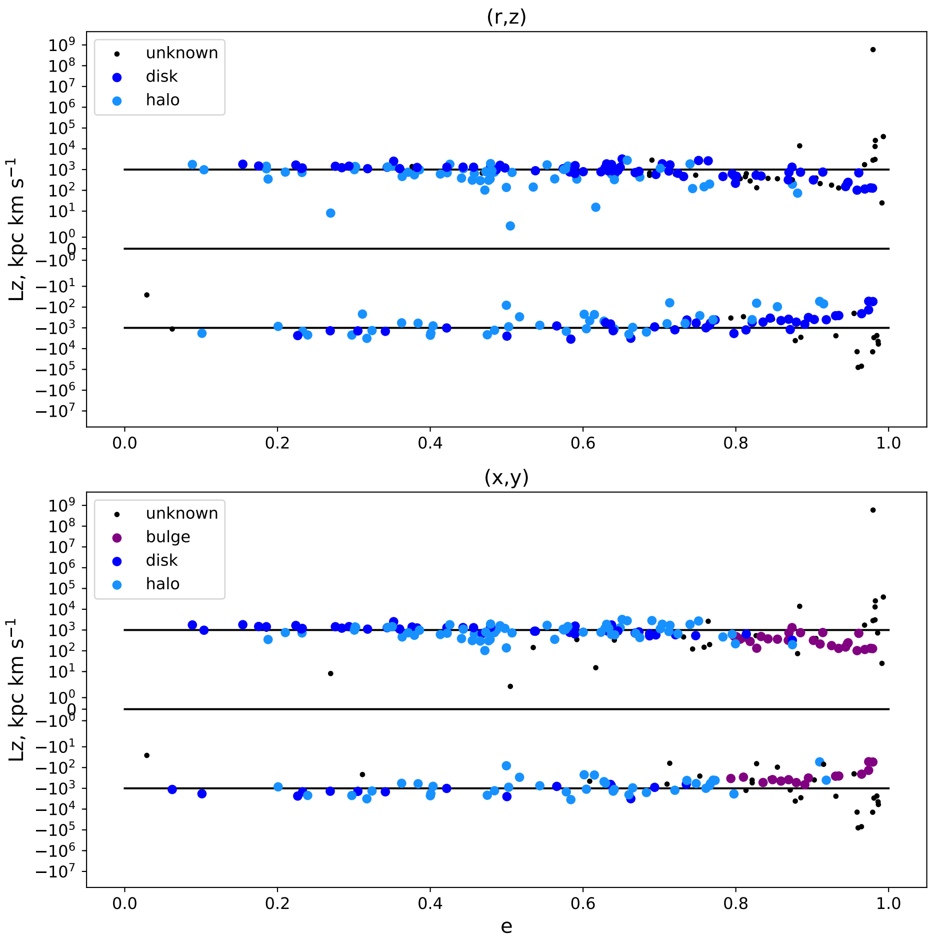

Figure 31: Relationships between the angular momentum along z direction L_z versus eccentricity e in axisymmetric potential for all stars colored according to orbits separation in (r,z) plane (*top*), in (x,y) plane (*bottom*).

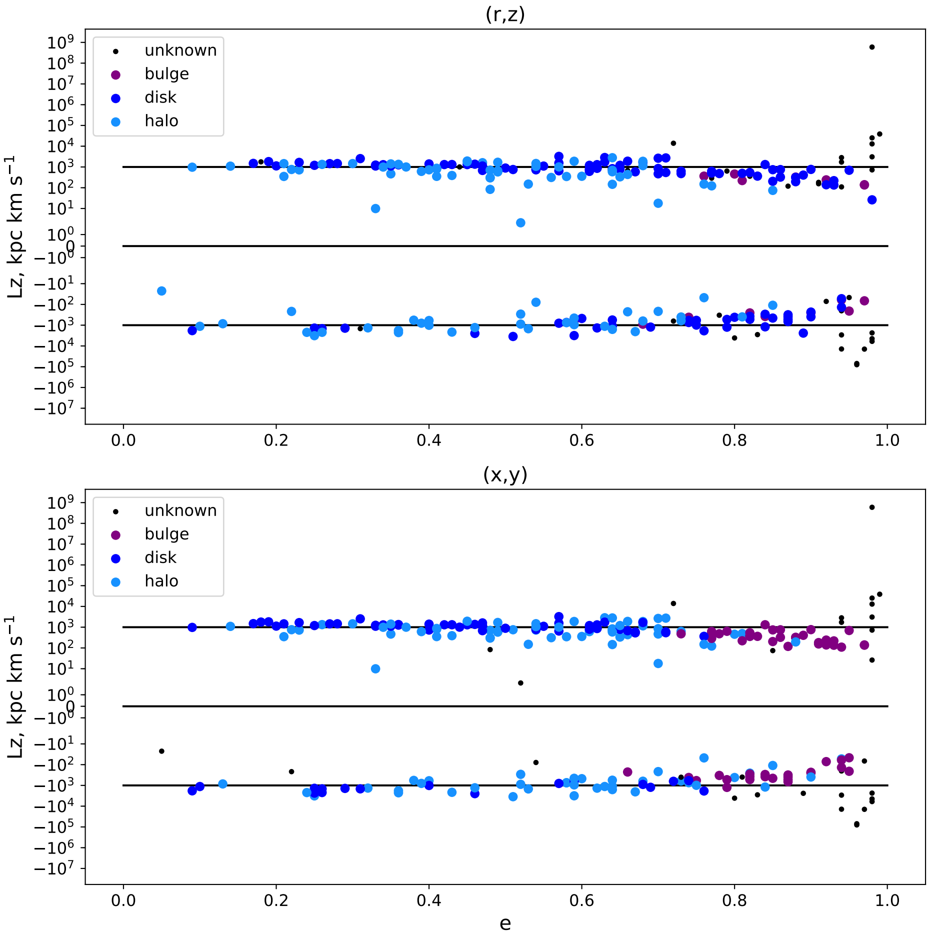

Figure 32: Relationships between the angular momentum along z direction L_z versus eccentricity e in barred potential for all stars colored according to orbits separation in (r,z) plane (*top*), in (x,y) plane (*bottom*).

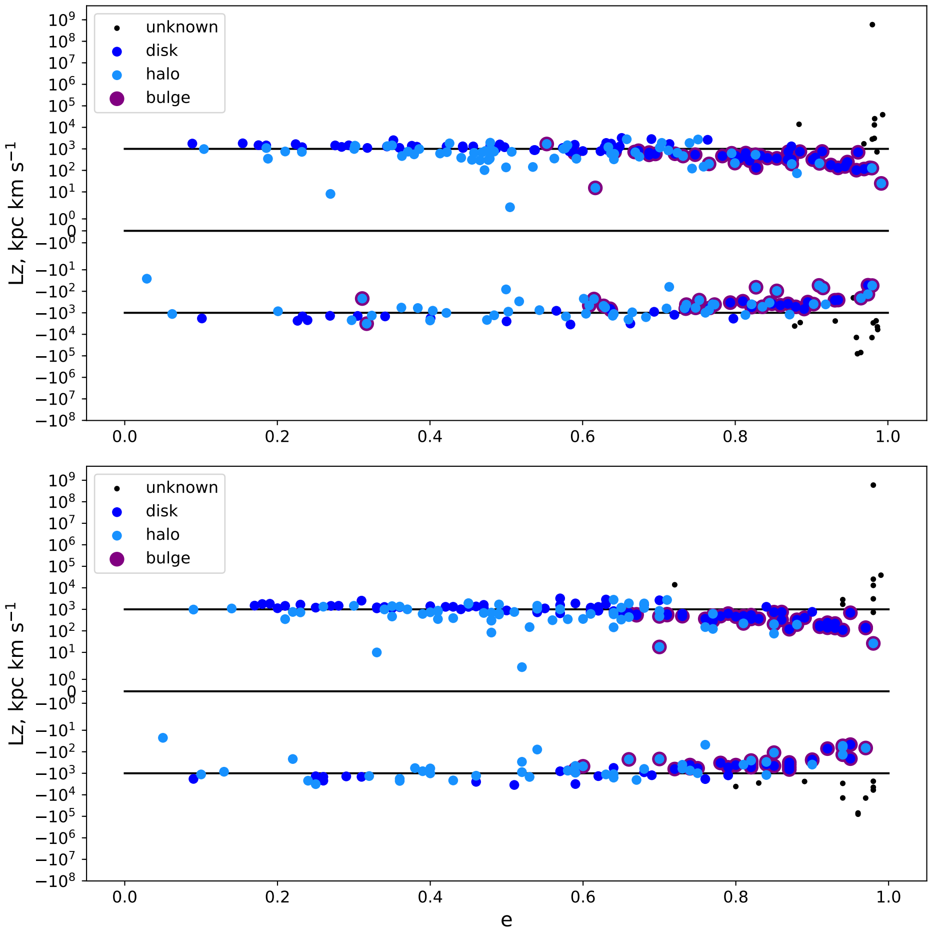

Figure 33: Relationships between the angular momentum along z direction L_z versus eccentricity e in axisymmetric (*top*) and barred (*bottom*) potential for all stars colored according to orbits separation with criteria.

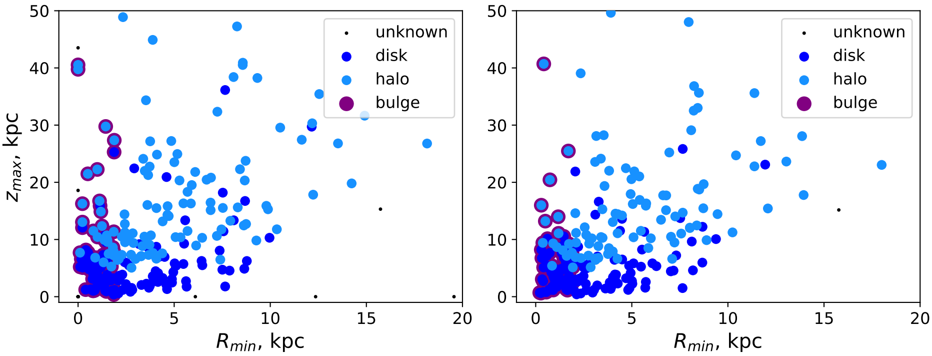

Figure 34: Relationships between the maximum height under the Galactic plane z_{max} versus perigalactic distances R_{min} in axisymmetric (*first row*) and barred (*second row*) potentials for all stars colored according to orbits separation with criteria.

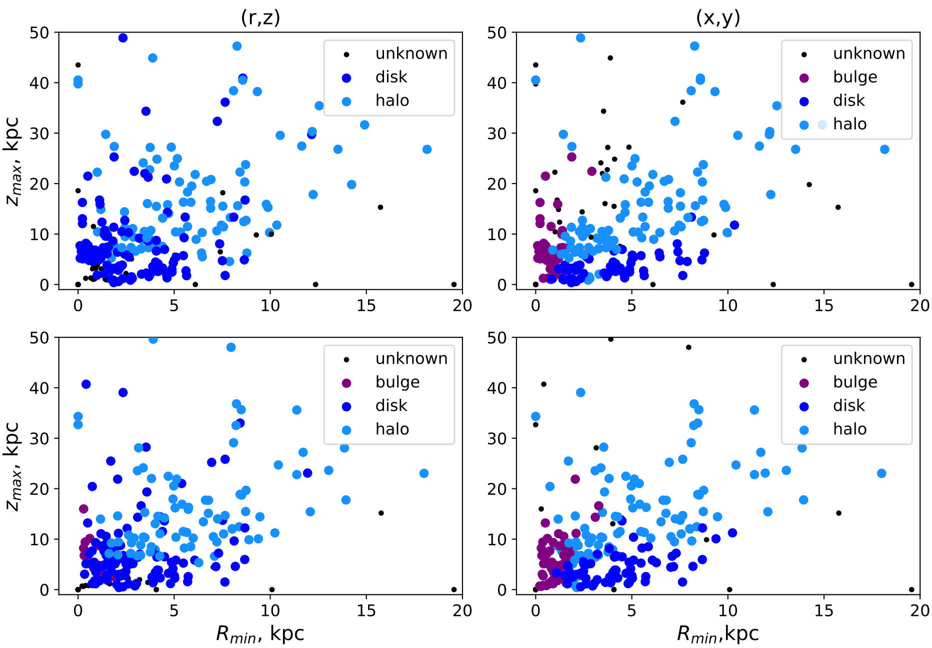

Figure 35: Relationships between the maximum height under the Galactic plane z_{max} versus perigalactic distances R_{min} in axisymmetric (*first row*) and barred (*second row*) potentials for all stars colored according to orbits separation in (r,z) plane (*left column*), in (x,y) plane (*right column*).

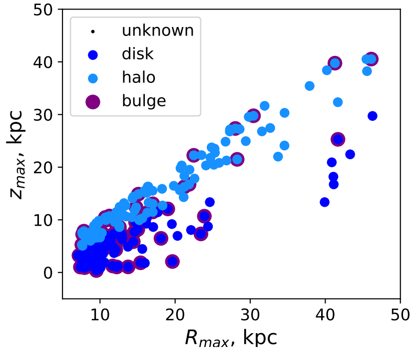

Figure 36: Relationships between the maximum height under the Galactic plane z_{max} versus apogalactic distances R_{max} in axisymmetric (*first row*) and barred (*second row*) potentials for all stars colored according to orbits separation with criteria.

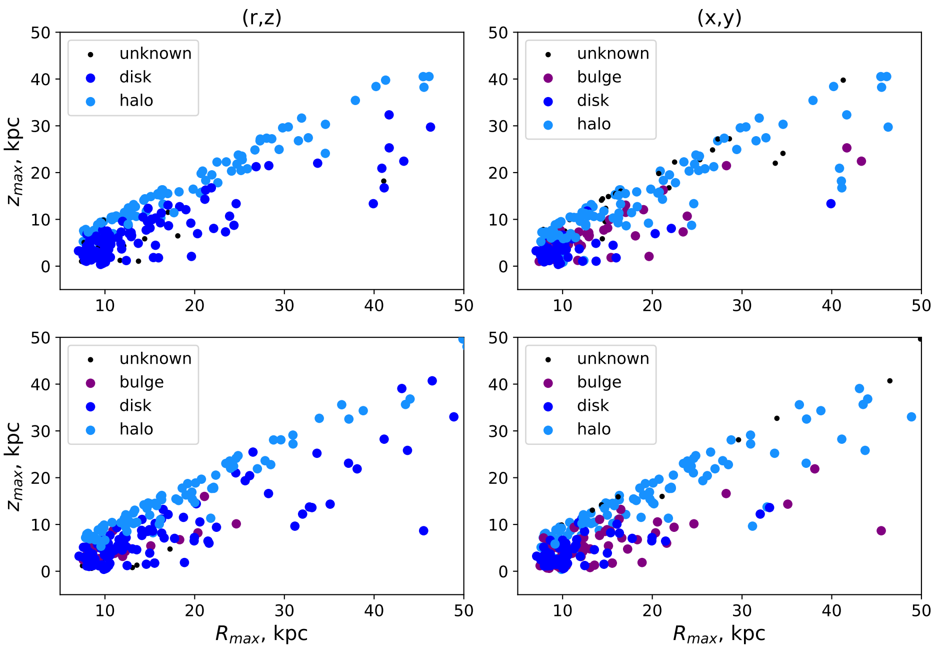

Figure 37: Relationships between the maximum height under the Galactic plane z_{max} versus apogalactic distances R_{max} in axisymmetric (*first row*) and barred (*second row*) potentials for all stars colored according to orbits separation in (r,z) plane (*left column*), in (x,y) plane (*right column*).

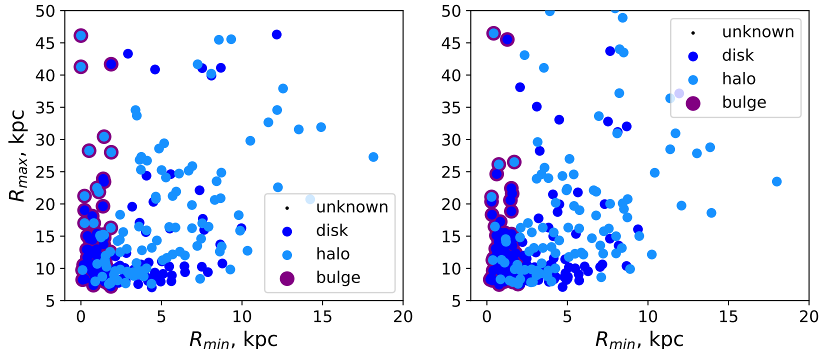

Figure 38: Relationships between the apogalactic distances R_{max} versus perigalactic distances R_{min} in axisymmetric (*first row*) and barred (*second row*) potentials for all stars colored according to orbits separation with criteria.

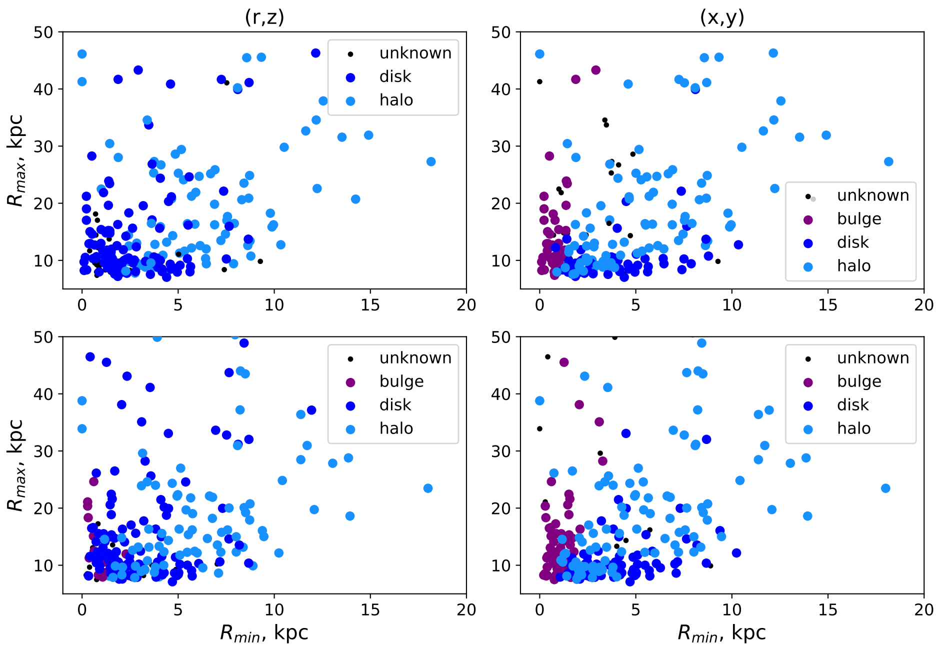

Figure 39: Relationships between the apogalactic distances R_{max} versus perigalactic distances R_{min} in axisymmetric (*first row*) and barred (*second row*) potentials for all stars colored according to orbits separation in (r,z) plane (*left column*), in (x,y) plane (*right column*).

5.5.5 Separation criteria

Finally, to improve and automatize separation by orbit technique. We propose the following procedure. We know that disk stars exhibit quasi-circular motion close to the Galactic plane with relatively small eccentricities, large circular velocities consequently large angular momentum L_z and small maximum height under the Galactic plane compare with apogalactic distance in the Galactic plane $z_{max} \ll r_{max}$. The halo stars instead have more elongated orbits with lower circular velocities, as a consequence lower angular momentum L_z, and due to spherical symmetry of the halo potential, there are no constraints on the orbit location.

Using this information we adopted following criteria to separate orbits:

1. *Presence of the bulge potential effect:* $R_{min} < 2kpc$.

   According to the potential model which we used (Yeh et al. (2020)) the bulge potential is mostly effective in the sphere of 2 kpc. It let us consider that all stars that reach this sphere during their motion are affected by axisymmetric bulge potential.

2. *Disk/halo separation:* $\frac{z_{max}}{R_{max}} < \frac{\sqrt{2}}{2}$.

   Due to cylindrical symmetry of the disk potential stars belonging to the Galactic disk are moving close to the Galactic plane $z_{max} \ll r_{max}$. $z_{max} = r_{max}$ than $z_{max} = R_{max} \cdot \sin 45^o \Rightarrow \frac{z_{max}}{R_{max}} < \frac{\sqrt{2}}{2}$

This result is in good agreement with found patterns in Fig.35, 37, 39 where stars was separated by orbits. To test found criteria we used all listed before methods: E/L_z diagram (Fig.27), $\frac{L_z}{e}$ distribution (Fig.29), L_z/e diagram (Fig.33). Than applied separation were tested with close look at individual orbits of the stars. It confirms that the splitting of the stars was done consistently. Only few percents of stars were related to the wrong group. All of them have $\frac{z_{max}}{R_{max}} \approx \frac{\sqrt{2}}{2}$. That means that close look to objects with $\frac{z_{max}}{R_{max}} \approx \frac{\sqrt{2}}{2}$ needed to improve automatic separation accuracy.

5.6 Origin

If we want to understand was these stars formed inside the Milky Way or outside orbital parameters can not give us a clear view. But it can say about the possibility of stars to be accreted.

Firstly, according to Yeh et al. (2020) in L_z/e diagram highly eccentric tails with low angular momentum L_z are mostly populated with members of past accreted events. But we can not separate in-situ and accreted stars only with orbital parameters L_z, e. To do it better an additional chemical analysis is needed.

Secondly, Koppelman et al. (2019) showed that clustering in E/L_z diagram can tell us about the accretion event. However, our stars do not show any significant clustering in the diagram. That means that our stars do not show clear evidence of accretion event as a group in their past history.

To test it more we can use the O-Na relation. Villanova et al. (2019) showed that globular cluster which was formed inside the Milky Way usually indicates O-Na anti-correlation. But, unfortunately, we do not have the abundance of sodium in our spectroscopic data.

5.7 Two populations

Going back to the two populations in CMD in the lower and upper parts of the Galactic halo with different age and metallicity according to isochrone fitting technique (section 4.3), Fig.40 shows the distribution of angular momentum L_z in relationship with eccentricity e colored with galactic latitude. We can see that stars from both populations show prograde and retrograde motion. Furthermore, stars located in upper ($b > 0^o$) and lower ($b < 0^o$) Galactic halo are mixed in this diagram and orbital parameters do not show any difference between the kinematics of these two populations.

The same result Fig.41 show. E/L_z diagram the correlation between angular momentum L_z and total energy of the star E colored with galactic latitude. Two groups for $b < 0^o$ (blue) and $b > 0^o$ (yellow) do not show any significant clustering in the diagram. That means that both populations do not show clear evidence of accretion event as a group in their past history.

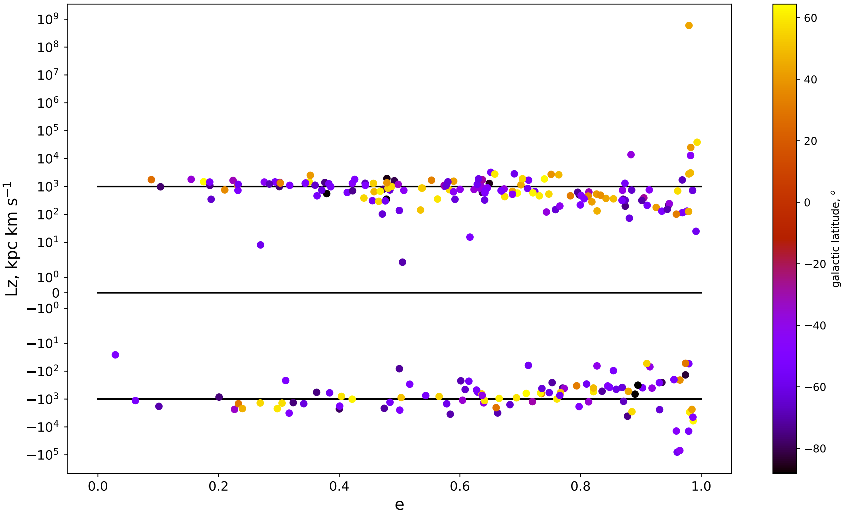

Figure 40: Relationships between the angular momentum along z direction L_z versus eccentricity e for all stars colored with galactic latitude.

6 Chemical composition

Correlation and scatter of chemical elements can provide constraints on mixing and the diversity of supernovae at early epochs. For our stars, the main trends were tested. In Fig.42 we see correlation between $\left[\frac{Al}{Fe}\right]$ and $\left[\frac{Fe}{H}\right]$ and anti-correlation between $\left[\frac{Mg}{Fe}\right]$ and $\left[\frac{Fe}{H}\right]$. Our diagrams have different scaling compare with results published by Koppelman et al. (2019) but they show the same trend.

Dispersion of metallicity of two groups: the disk and halo stars separated in section 5 were studied. In Fig.43 we can see that on average halo stars are more metal-poor than disk stars. However, the difference between peaks is around ~ 0.1 dex.

Additionally, in section 4.3.5 we found the group of Blue Stragglers in bluer population. According to Ferraro et al. (2006) they should be oxygen and carbon depleted which was considered as the signature of the mass-transfer formation process. However it is only partly true for stars under consideration (Fig.44).

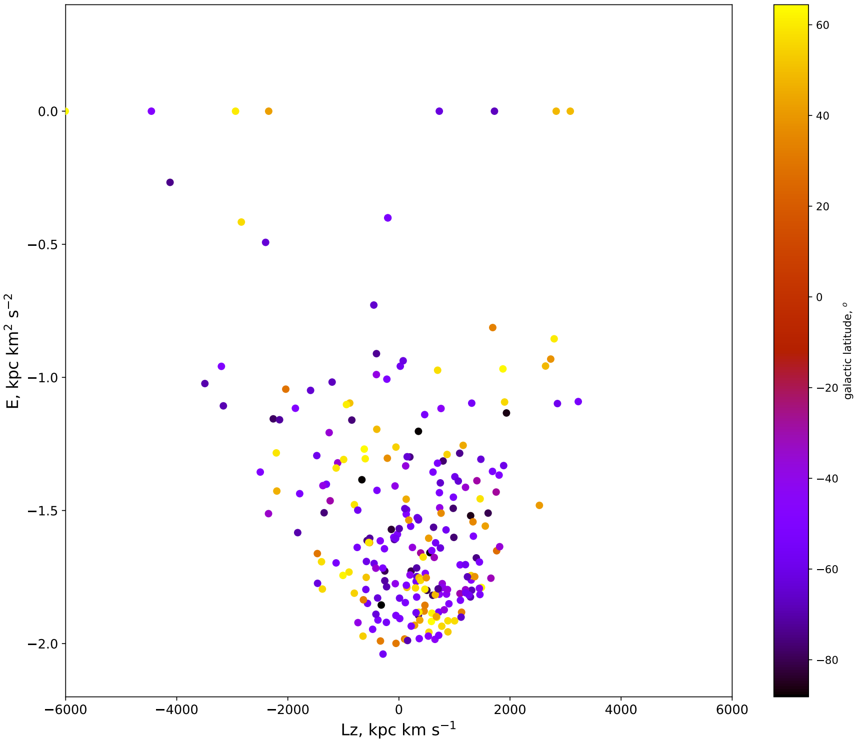

Figure 41: Relationships between the total energy E versus angular momentum along z direction L_z for all stars colored with galactic latitude.

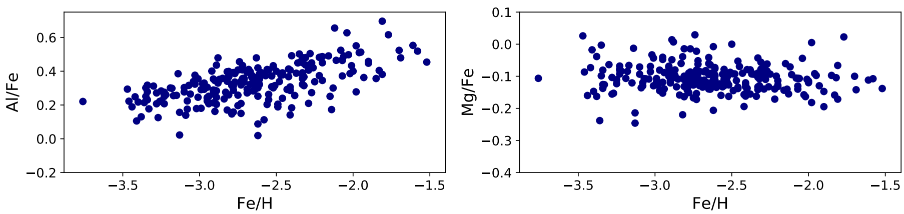

Figure 42: Relationships between the $\left[\frac{Al}{Fe}\right]$ and $\left[\frac{Mg}{Fe}\right]$ versus metallicity $\left[\frac{Fe}{H}\right]$.

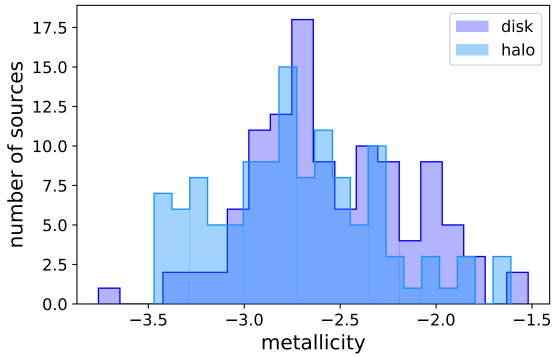

Figure 43: Distribution of metallicity for the disk and bulge stars.

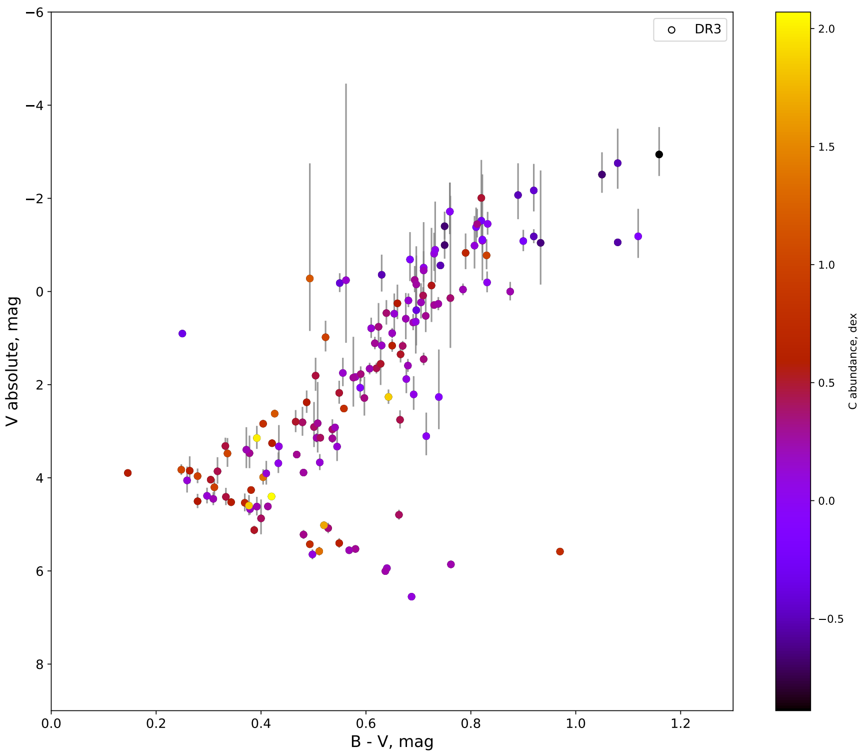

Figure 44: CMD in Johnson photometry colored with carbon abundace.

7 Conclusion

In this thesis, a data set of 253 very metal-poor stars spectroscopically studied by Barklem2005 was analyzed with the aim to understand the origin of these stars.

We demonstrated that the best estimate of the stars' distances for this data set is the original parallaxes from Gaia EDR3. Corrections from Lindegren2021 and Bailer-Jones et al. (2021) are found to be incorrect for some stars and responsible for the unexpected location of stars below the red giant branch locus as implied by their age and metallicity. That is why they were not used in the main analysis.

We studied the color-magnitude diagram (CMD) in two photometric systems: Johnson and Gaia EDR3, taking into consideration that they have similar ages. The isochrones for old metal-poor populations such as Padova isochrones [5] and a suite of Stellar Tracks and Isochrones (BaSTI) (Hidalgo et al. (2018)) were taken. They were chosen because they used the most modern stellar models taking into account low metallicities. The study of CMD showed that our data set consists of two populations with different metallicity and age (bluer and redder according to color B-V). The best fit isochrones for redder group located mostly in the redder turn-off point with only few dots in red giant branch with average metallicity $\left[\frac{Fe}{H}\right] \approx -2$ is 14 Gyr isochrone with $\left[\frac{Fe}{H}\right] = -1.9$ for BaSTI and $\left[\frac{Fe}{H}\right] = -2$ for Padova. These are very old but relatively metal-reach stars. Their age is close the age of the Universe that means that they were formed recently after the Big Bang. And, therefore can be used to probe the first epoch of cosmic star formation. This group was found to be sligthly older than globular clusters: NGC 6397 (12.6 Gyr), M 30 (13.0 Gyr), M92 (12.5 Gyr).

The bluer group with metallicity in range $\left[\frac{Fe}{H}\right] \approx -2.2 - -2.5$ populates, then, the bluer turn-off region and the lower part of red giant branch. The best fit is 11 Gyr with metallicity $\left[\frac{Fe}{H}\right] = -2.2$ for Padova and BaSTI isochrones. This group is younger than the previous one but more metal-poor. An important feature of this group is that stars that lie on the blue side of the turn-off point should hold younger ages (Fig.20) but due to their low metallicity they can not have such young ages (3-5 Gyr). These stars are usually called Blue Stragglers. According to Ferraro et al. (2006) they should be oxygen and carbon depleted which was considered as the signature of the mass-transfer formation process. However, it is only partly true for stars under consideration.

Actually, we found a third population in metallicity $\left[\frac{Fe}{H}\right] \approx -3.2$ but the majority of the stars are located in the red giant branch which makes impossible the age determination from isochrone fitting. The turn-off point is the main indicator for age and we have just a few stars there. That is why the chosen best

[5] http://stev.oapd.inaf.it/cmd

fit isochrone 14 Gyr with $\left[\frac{Fe}{H}\right] = -3.2$ is not accurate and is meant as just an estimate.

All results are listed in Tab.7 and shown in Fig.19

The best fit isochrone was obtained by eye-balling the star distribution because there are not enough stars for statistical analysis.

Also, we should mention that the split into two populations in turn-off point is well explained with Galactic latitude (Fig.10). The blue group is coming from upper Galactic halo, the redder group instead is located in the lower part. But reddening is not playing any role in this dichotomy.

Later, with proper motion, radial velocity and parallaxes from Gaia EDR3 orbits and orbital parameters were numerically calculated in two types of the Galactic potential: with and without bar. Further, different techniques of separation were applied. First, we separated the stars according to the shape of their orbit (Bajkova et al. (2020)), then an automatic technique was obtained. The separation by orbits and the automatic one give results in good agreement. Both separations were additionally tested with the methods: E/L_z diagram (Fig.27), $\frac{L_z}{e}$ distribution (Fig.29), L_z/e diagram (Fig.33). As a result, very metal-poor stars were divided into two groups with the disk and the halo kinematics. A part of both groups is found to be affected by bulge potential which reduced their angular momentum L_z.

Two populations from the photometric analysis are non distinguishable with orbital parameters and are not showing any substantial difference between each other (Fig.40, 41).

Unfortunately, only with orbits and orbital parameters we cannot say if our stars were formed inside or outside our Galaxy. However, we have well-populated tails of low angular momentum L_z and high eccentricity which is typically but not necessary populated by accreted parts (Yeh et al. (2020)). Although, E/L_z diagram does not show any significant clustering that can be a signature that they were not accreted as a group (Koppelman et al. (2019)).

Stars following disk kinematics are on average more metal-rich than halo stars but the difference is not always significant. Also, stars under investigation show correlation between $\left[\frac{Al}{Fe}\right]$ and $\left[\frac{Fe}{H}\right]$ and anti-correlation between $\left[\frac{Mg}{Fe}\right]$ and $\left[\frac{Fe}{H}\right]$ (Fig.42). Our diagrams have different scaling compared with results published by Koppelman et al. (2019). However, the trend is the same.

Acknowledgements

I would like to thank my supervisors Giovanni Carraro and Sergio Ortolani for the opportunity to work on this intriguing topic and the support they gave me. Their warm science group helped me to work and enjoy working.

A big thank you goes to the University of Padova and its professors that helped me to obtain the necessary knowledge and hone my research skills.

And finally thanks to my family and friends who supported me during my whole education time.

References

Ade, P. A. R., N. Aghanim, C. Armitage-Caplan, M. Arnaud, M. Ashdown, F. Atrio-Barandela, J. Aumont, C. Baccigalupi, A. J. Banday & et al. 2014. Planck2013 results. xvi. cosmological parameters. *Astronomy Astrophysics* 571. A16. DOI: 10.1051/0004-6361/201321591. http://dx.doi.org/10.1051/0004-6361/201321591.

Allen, C. & M. A. Martos. 1986. A simple, realistic model of the galactic mass distribution for orbitcomputations. 13. 137–147.

Allen, Christine & Alfredo Santillan. 1991. An improved model of the galactic mass distribution for orbit computations. 22. 255.

El-Badry, Kareem, Hans-Walter Rix & Tyler M. Heintz. 2021. A million binaries from Gaia eDR3: sample selection and validation of Gaia parallax uncertainties. DOI: 10.1093/mnras/stab323.

Bailer-Jones, C. A. L., J. Rybizki, M. Fouesneau, M. Demleitner & R. Andrae. 2021. Estimating Distances from Parallaxes. V. Geometric and Photogeometric Distances to 1.47 Billion Stars in Gaia Early Data Release 3. 161(3), 147. 147. DOI: 10.3847/1538-3881/abd806.

Bajkova, A. T., G. Carraro, V. I. Korchagin, N. O. Budanova & V. V. Bobylev. 2020. Milky Way Subsystems from Globular Cluster Kinematics Using Gaia DR2 and HST Data. 895(1), 69. 69. DOI: 10.3847/1538-4357/ab8ea7.

Barklem, P. S., N. Christlieb, T. C. Beers, V. Hill, M. S. Bessell, J. Holmberg, B. Marsteller, S. Rossi, F. -J. Zickgraf & D. Reimers. 2005. The Hamburg/ESO R-process enhanced star survey (HERES). II. Spectroscopic analysis of the survey sample. 439(1). 129–151. DOI: 10.1051/0004-6361:20052967.

Beers, Timothy C., Silvia Rossi, John E. Norris, Sean G. Ryan & Thomas Shefler. 1999. Estimation of Stellar Metal Abundance. II. A Recalibration of the Ca II K Technique, and the Autocorrelation Function Method. 117(2). 981–1009. DOI: 10.1086/300727.

Belokurov, V., D. Erkal, N. W. Evans, S. E. Koposov & A. J. Deason. 2018. Co-formation of the disc and the stellar halo. 478(1). 611–619. DOI: 10.1093/mnras/sty982.

Bennett, C. L., D. Larson, J. L. Weiland, N. Jarosik, G. Hinshaw, N. Odegard, K. M. Smith, R. S. Hill, B. Gold, M. Halpern & et al. 2013. Nine-year wilkinson microwave anisotropy probe (wmap) observations: final maps and results. *The Astrophysical Journal Supplement Series* 208(2). 20. DOI: 10.1088/0067-0049/208/2/20. http://dx.doi.org/10.1088/0067-0049/208/2/20.

Bhattacharjee, Pijushpani, Soumini Chaudhury & Susmita Kundu. 2014. Rotation Curve of the Milky Way out to ~200 kpc. 785(1), 63. 63. DOI: 10.1088/0004-637X/785/1/63.

Bond, Howard E., Edmund P. Nelan, Don A. VandenBerg, Gail H. Schaefer & Dianne Harmer. 2013. HD 140283: A Star in the Solar Neighborhood that Formed Shortly after the Big Bang. 765(1), L12. L12. DOI: 10.1088/2041-8205/765/1/L12.

Bovy, Jo, Henry W. Leung, Jason A. S. Hunt, J. Ted Mackereth, Domingo A. García-Hernández & Alexandre Roman-Lopes. 2019. Life in the fast lane: a direct view of the dynamics, formation, and evolution of the Milky Way's bar. 490(4). 4740–4747. DOI: 10.1093/mnras/stz2891.

Bromm, Volker & Richard B. Larson. 2004. The First Stars. 42(1). 79–118. DOI: 10.1146/annurev.astro.42.053102.134034.

Bullock, James S. & Kathryn V. Johnston. 2005. Tracing Galaxy Formation with Stellar Halos. I. Methods. 635(2). 931–949. DOI: 10.1086/497422.

Cayrel, R., E. Depagne, M. Spite, V. Hill, F. Spite, P. François, B. Plez, T. Beers, F. Primas, J. Andersen, B. Barbuy, P. Bonifacio, P. Molaro & B. Nordström. 2004. First stars V - Abundance patterns from C to Zn and supernova yields in the early Galaxy. 416. 1117–1138. DOI: 10.1051/0004-6361:20034074.

Christlieb, N., T. C. Beers, P. S. Barklem, M. Bessell, V. Hill, J. Holmberg, A. J. Korn, B. Marsteller, L. Mashonkina, Y. -Z. Qian, S. Rossi, G. J. Wasserburg, F. -J. Zickgraf, K. -L. Kratz, B. Nordström, B. Pfeiffer, J. Rhee & S. G. Ryan. 2004. The Hamburg/ESO R-process Enhanced Star survey (HERES). I. Project description, and discovery of two stars with strong enhancements of neutron-capture elements. 428. 1027–1037. DOI: 10.1051/0004-6361:20041536.

Correnti, Matteo, Mario Gennaro, Jason S. Kalirai, Roger E. Cohen & Thomas M. Brown. 2018. The Age of the Old Metal-poor Globular Cluster NGC 6397 Using WFC3/IR Photometry. 864(2), 147. 147. DOI: 10.3847/1538-4357/aad805.

Courteau, Stephane, Roelof S. de Jong & Adrick H. Broeils. 1996. Evidence for Secular Evolution in Late-Type Spirals. 457. L73. DOI: 10.1086/309906.

De Propris, Roberto, Matthew Colless, Simon P. Driver, Michael B. Pracy & Warrick J. Couch. 2005. Internal colour gradients for E/S0 galaxies in Abell 2218. 357(2). 590–598. DOI: 10.1111/j.1365-2966.2005.08662.x.

Eggen, O. J., D. Lynden-Bell & A. R. Sandage. 1962. Evidence from the motions of old stars that the Galaxy collapsed. 136. 748. DOI: 10.1086/147433.

Frebel, Anna & John E. Norris. 2015. Near-Field Cosmology with Extremely Metal-Poor Stars. 53. 631–688. DOI: 10.1146/annurev-astro-082214-122423.

Gadotti, D. A. & S. dos Anjos. 2001. Homogenization of the Stellar Population along Late-Type Spiral Galaxies. 122(3). 1298–1318. DOI: 10.1086/322126.

Gaia Collaboration. 2021. Gaia Early Data Release 3. Summary of the contents and survey properties. 649, A1. A1. DOI: 10.1051/0004-6361/202039657.

Gilmore, Gerard. 1996. Early and Late Evolution of the Milky Way. In Heather L. Morrison & Ata Sarajedini (eds.), *Formation of the galactic halo...inside and out*, vol. 92 (Astronomical Society of the Pacific Conference Series), 161.

Grillmair, Carl J. 2017. At a Crossroads: Stellar Streams in the South Galactic Cap. 847(2), 119. 119. DOI: 10.3847/1538-4357/aa8872.

Helmi, A. 2002. Signatures of galaxy mergers in the Milky Way: Here, there and everywhere. 281(1). 351–354. DOI: 10.1023/A:1019590831169.

Hidalgo, Sebastian L., Adriano Pietrinferni, Santi Cassisi, Maurizio Salaris, Alessio Mucciarelli, Alessandro Savino, Antonio Aparicio, Victor Silva Aguirre & Kuldeep Verma. 2018. The Updated BaSTI Stellar Evolution Models and Isochrones. I. Solar-scaled Calculations. 856(2), 125. 125. DOI: 10.3847/1538-4357/aab158.

Hill, V., B. Plez, R. Cayrel, T. C. Beers, B. Nordström, J. Andersen, M. Spite, F. Spite, B. Barbuy, P. Bonifacio, E. Depagne, P. François & F. Primas. 2002. First stars. I. The extreme r-element rich, iron-poor halo giant CS 31082-001. Implications for the r-process site(s) and radioactive cosmochronology. 387. 560–579. DOI: 10.1051/0004-6361:20020434.

Ibata, R. A., G. F. Lewis, M. J. Irwin & L. Cambrésy. 2002. Substructure of the outer Galactic halo from the 2-Micron All-Sky Survey. 332(4). 921–927. DOI: 10.1046/j.1365-8711.2002.05360.x.

Irrgang, A., B. Wilcox, E. Tucker & L. Schiefelbein. 2013. Milky Way mass models for orbit calculations. 549, A137. A137. DOI: 10.1051/0004-6361/201220540.

Jordi, C., M. Gebran, J. M. Carrasco, J. de Bruijne, H. Voss, C. Fabricius, J. Knude, A. Vallenari, R. Kohley & A. Mora. 2010a. Gaia broad band photometry. 523, A48. A48. DOI: 10.1051/0004-6361/201015441.

Jordi, C., M. Gebran, J. M. Carrasco, J. de Bruijne, H. Voss, C. Fabricius, J. Knude, A. Vallenari, R. Kohley & A. Mora. 2010b. VizieR Online Data Catalog:

Gaia photometry (Jordi+, 2010). *VizieR Online Data Catalog*, J/A+A/523/A48. J/A+A/523/A48.

Kains, N., D. M. Bramich, A. Arellano Ferro, R. Figuera Jaimes, U. G. Jørgensen, S. Giridhar, M. T. Penny, K. A. Alsubai, J. M. Andersen, V. Bozza, P. Browne, M. Burgdorf, S. Calchi Novati, Y. Damerdji, C. Diehl, P. Dodds, M. Dominik, A. Elyiv, X. -S. Fang, E. Giannini, S. -H. Gu, S. Hardis, K. Harpsøe, T. C. Hinse, A. Hornstrup, M. Hundertmark, J. Jessen-Hansen, D. Juncher, E. Kerins, H. Kjeldsen, H. Korhonen, C. Liebig, M. N. Lund, M. Lundkvist, L. Mancini, R. Martin, M. Mathiasen, M. Rabus, S. Rahvar, D. Ricci, K. Sahu, G. Scarpetta, J. Skottfelt, C. Snodgrass, J. Southworth, J. Surdej, J. Tregloan-Reed, C. Vilela, O. Wertz & A. Williams. 2013. Estimating the parameters of globular cluster M 30 (NGC 7099) from time-series photometry. 555, A36. A36. DOI: 10.1051/0004-6361/201321819.

Koppelman, Helmer H., Amina Helmi, Davide Massari, Adrian M. Price-Whelan & Tjitske K. Starkenburg. 2019. Multiple retrograde substructures in the Galactic halo: A shattered view of Galactic history. 631, L9. L9. DOI: 10.1051/0004-6361/201936738.

Limberg, Guilherme, Rafael M. Santucci, Silvia Rossi, Derek Shank, Vinicius M. Placco, Timothy C. Beers, Kevin C. Schlaufman, Andrew R. Casey, Hélio D. Perottoni & Young Sun Lee. 2021. Targeting Bright Metal-poor Stars in the Disk and Halo Systems of the Galaxy. 913(1), 11. 11. DOI: 10.3847/1538-4357/abeefe.

Lindegren, L., U. Bastian, M. Biermann, A. Bombrun, A. de Torres, E. Gerlach, R. Geyer, J. Hernández, T. Hilger, D. Hobbs, S. A. Klioner, U. Lammers, P. J. McMillan, M. Ramos-Lerate, H. Steidelmüller, C. A. Stephenson & F. van Leeuwen. 2021. Gaia Early Data Release 3. Parallax bias versus magnitude, colour, and position. 649, A4. A4. DOI: 10.1051/0004-6361/202039653.

Madau, Piero & Mark Dickinson. 2014. Cosmic Star-Formation History. 52. 415–486. DOI: 10.1146/annurev-astro-081811-125615.

McWilliam, Andrew, George W. Preston, Christopher Sneden & Leonard Searle. 1995. Spectroscopic Analysis of 33 of the Most Metal Poor Stars. II. 109. 2757. DOI: 10.1086/117486.

McWilliam, Andrew, George W. Preston, Christopher Sneden & Stephen Shectman. 1995. A Spectroscopic Analysis of 33 of the Most Metal-Poor Stars.I. 109. 2736. DOI: 10.1086/117485.

Miyamoto, M. & R. Nagai. 1975. Three-dimensional models for the distribution of mass in galaxies. 27. 533–543.

Myeong, G. C., E. Vasiliev, G. Iorio, N. W. Evans & V. Belokurov. 2019. Evidence for two early accretion events that built the Milky Way stellar halo. 488(1). 1235–1247. DOI: 10.1093/mnras/stz1770.

Norris, John E., Sean G. Ryan & Timothy C. Beers. 2001. Extremely Metal-Poor Stars. VIII. High-Resolution, High Signal-to-Noise Ratio Analysis of Five Stars with [Fe/H]<~-3.5. 561(2). 1034–1059. DOI: 10.1086/323429.

Pichardo, Bárbara, Marco Martos & Edmundo Moreno. 2004. Models for the Gravitational Field of the Galactic Bar: An Application to Stellar Orbits in the Galactic Plane and Orbits of Some Globular Clusters. 609(1). 144–165. DOI: 10.1086/421008.

Queiroz, A. B. A., F. Anders, C. Chiappini, A. Khalatyan, B. X. Santiago, M. Steinmetz, M. Valentini, A. Miglio, D. Bossini, B. Barbuy, I. Minchev, D. Minniti, D. A. García Hernández, M. Schultheis, R. L. Beaton, T. C. Beers, D. Bizyaev, J. R. Brownstein, K. Cunha, J. G. Fernández-Trincado, P. M. Frinchaboy, R. R. Lane, S. R. Majewski, D. Nataf, C. Nitschelm, K. Pan, A. Roman-Lopes, J. S. Sobeck, G. Stringfellow & O. Zamora. 2019. From the bulge to the outer disc: StarHorse stellar parameters, distances, and extinctions for stars in APOGEE DR16 and other spectroscopic surveys. *arXiv e-prints*, arXiv:1912.09778. arXiv:1912.09778.

Ritter, Jeremy S., Chalence Safranek-Shrader, Orly Gnat, Miloš Milosavljević & Volker Bromm. 2012. Confined Population III Enrichment and the Prospects for Prompt Second-generation Star Formation. 761(1), 56. 56. DOI: 10.1088/0004-637X/761/1/56.

Safranek-Shrader, C., M. Milosavljevic & V. Bromm. 2014. Formation of the first low-mass stars from cosmological initial conditions. 440. L76–L80. DOI: 10.1093/mnrasl/slu027.

Schlafly, Edward F. & Douglas P. Finkbeiner. 2011. Measuring Reddening with Sloan Digital Sky Survey Stellar Spectra and Recalibrating SFD. 737(2), 103. 103. DOI: 10.1088/0004-637X/737/2/103.

Schlaufman, Kevin C. & Andrew R. Casey. 2014. The Best and Brightest Metal-poor Stars. 797(1), 13. 13. DOI: 10.1088/0004-637X/797/1/13.

Searle, L. & R. Zinn. 1978. Composition of halo clusters and the formation of the galactic halo. 225. 357–379. DOI: 10.1086/156499.

Sneden, Christopher, John J. Cowan, James E. Lawler, Inese I. Ivans, Scott Burles, Timothy C. Beers, Francesca Primas, Vanessa Hill, James W. Truran, George M. Fuller, Bernd Pfeiffer & Karl-Ludwig Kratz. 2003. The Extremely Metal-poor, Neutron Capture-rich Star CS 22892-052: A Comprehensive Abundance Analysis. 591(2). 936–953. DOI: 10.1086/375491.

Valenti, J. A. & N. Piskunov. 1996. Spectroscopy made easy: A new tool for fitting observations with synthetic spectra. 118. 595–603.

VandenBerg, Don A., Howard E. Bond, Edmund P. Nelan, P. E. Nissen, Gail H. Schaefer & Dianne Harmer. 2014. Three Ancient Halo Subgiants: Precise Parallaxes, Compositions, Ages, and Implications for Globular Clusters. 792(2), 110. 110. DOI: 10.1088/0004-637X/792/2/110.

VandenBerg, Don A., P. A. Denissenkov & Márcio Catelan. 2016. Constraints on the Distance Moduli, Helium and Metal Abundances, and Ages of Globular Clusters from their RR Lyrae and Non-variable Horizontal-branch Stars. I. M3, M15, and M92. 827(1), 2. 2. DOI: 10.3847/0004-637X/827/1/2.

Vasiliev, Eugene & Holger Baumgardt. 2021. Gaia EDR3 view on Galactic globular clusters. *arXiv e-prints*, arXiv:2102.09568. arXiv:2102.09568.

Villanova, Sandro, Lorenzo Monaco, Doug Geisler, Julia O'Connell, Dante Minniti, Paulina Assmann & Rodolfo Barbá. 2019. Detailed Chemical Composition and Orbit of the Newly Discovered Globular Cluster FSR 1758: Implications for the Accretion of the Sequoia Dwarf Galaxy onto the Milky Way. 882(2), 174. 174. DOI: 10.3847/1538-4357/ab3722.

Yeh, Fu-Chi, Giovanni Carraro, Vladimir I. Korchagin, Camilla Pianta & Sergio Ortolani. 2020. The origin of globular cluster FSR 1758. 635, A125. A125. DOI: 10.1051/0004-6361/201937093.

Yuan, Zhen, G. C. Myeong, Timothy C. Beers, N. W. Evans, Young Sun Lee, Projjwal Banerjee, Dmitrii Gudin, Kohei Hattori, Haining Li, Tadafumi Matsuno, Vinicius M. Placco, M. C. Smith, Devin D. Whitten & Gang Zhao. 2020. Dynamical Relics of the Ancient Galactic Halo. 891(1), 39. 39. DOI: 10.3847/1538-4357/ab6ef7.

Appendix

target ID	RA o	DEC o	l o	b o
CS 22175-007	34.36097	-9.01262	175.25085	-62.78035
CS 22186-023	64.93977	-36.86000	239.06462	-45.32794
CS 22186-025	66.13667	-37.15072	239.54900	-44.38974
CS 22886-042	335.10758	-10.38894	50.79948	-50.74862
CS 22892-052	334.25696	-16.65754	41.14543	-52.84838
CS 22945-028	352.80643	-66.49947	314.89398	-48.72372
CS 22957-013	358.95441	-5.38141	89.11769	-64.53712
CS 22958-083	33.92799	-53.99899	278.71927	-58.98780
CS 22960-010	332.10484	-44.89928	353.25953	-53.07420
CS 29491-069	337.75916	-32.64363	14.01451	-59.21435
CS 29491-109	336.25505	-32.24483	14.79017	-57.94676
CS 29497-004	7.02886	-26.05118	43.28777	-84.67655
CS 29510-058	35.44411	-24.03305	209.33340	-69.42411
CS 30308-035	311.47568	-44.84154	355.71671	-38.59224
CS 30315-001	354.41178	-26.36479	31.38231	-73.52313
CS 30315-029	353.61123	-26.70392	29.94526	-72.84841
CS 30337-097	330.33959	-30.96606	16.60609	-52.85257
CS 30339-041	5.80390	-37.02412	332.25129	-78.44734
CS 30343-063	326.32293	-37.37182	6.16641	-49.75697
CS 31060-047	2.03256	-15.90106	78.90427	-74.93387
CS 31062-041	8.76257	-15.90818	103.37911	-78.15317
CS 31072-118	77.22321	-59.30603	268.23129	-36.06180
CS 31082-001	22.37977	-16.01283	163.33959	-75.80312
HD 20	1.31451	-27.27188	29.48755	-79.73436
HD 221170	352.36995	30.43250	102.70452	-29.19991
HE 0005-0002	2.02821	0.23580	100.33556	-60.72103
HE 0008-3842	2.73349	-38.43614	337.26334	-75.86637
HE 0017-4838	4.95138	-48.35661	316.99505	-67.89877
HE 0018-1349	5.21824	-13.54164	93.69719	-74.65127
HE 0023-4825	6.45986	-48.14086	314.59066	-68.40378
HE 0029-1839	8.03227	-18.37691	94.99778	-80.18462
HE 0037-2657	9.96581	-26.69221	41.86657	-87.38315
HE 0039-4154	10.43086	-41.63263	310.13041	-75.35956
HE 0043-2845	11.48350	-28.48831	344.43735	-88.17493

HE 0044-2459	11.64957	-24.71733	98.37293	-87.35493
HE 0044-4023	11.62242	-40.12302	307.12927	-76.96487
HE 0045-2430	11.91908	-24.23392	106.40524	-86.98419
HE 0049-5700	13.02885	-56.74380	302.74398	-60.38421
HE 0051-2304	13.46467	-22.79838	130.28311	-85.63553
HE 0054-0657	14.33664	-6.68328	127.12586	-69.50691
HE 0057-4541	14.99699	-45.41490	298.16541	-71.63414
HE 0104-4007	16.73337	-39.86429	289.74145	-76.86447
HE 0104-5300	16.71638	-52.73628	297.55650	-64.23065
HE 0105-6141	16.90773	-61.42163	299.50517	-55.59875
HE 0109-0742	17.94618	-7.44228	137.63329	-69.73117
HE 0109-3711	17.91005	-36.92150	280.62065	-79.31625
HE 0111-1454	18.45456	-14.63970	146.70594	-76.46737
HE 0121-2826	20.90476	-28.17447	223.13947	-82.79863
HE 0131-2740	23.35750	-27.42447	217.15605	-80.66736
HE 0131-3953	23.40197	-39.63130	270.57582	-74.73403
HE 0143-1135	26.54338	-11.33681	164.72919	-69.63419
HE 0143-4108	26.33312	-40.89342	267.48723	-72.31908
HE 0143-4146	26.32516	-41.52962	268.89599	-71.85318
HE 0157-3335	30.00094	-33.35618	239.92584	-73.96172
HE 0200-0955	30.81760	-9.68024	170.48937	-65.67846
HE 0202-2204	31.20842	-21.83625	199.32883	-72.50334
HE 0231-4016	38.43514	-40.06183	250.91865	-65.21511
HE 0240-0807	40.74053	-7.90984	182.07468	-57.34598
HE 0240-6105	40.52551	-60.88419	281.68379	-51.43499
HE 0243-0753	41.55896	-7.68144	182.69301	-56.57395
HE 0243-5238	41.40088	-52.43279	270.65514	-56.94059
HE 0244-4111	41.48945	-40.98525	250.83281	-62.71699
HE 0248+0039	42.74606	0.85874	173.57394	-49.88129
HE 0256-1109	44.79261	-10.96730	190.85675	-55.92021
HE 0300-0751	45.76699	-7.66180	187.09264	-53.25557
HE 0305-4520	46.75911	-45.15015	255.71636	-57.59115
HE 0308-1154	47.79051	-11.72263	194.65048	-53.81113
HE 0315+0000	49.41256	0.18461	181.13925	-45.51708
HE 0316+0214	49.78848	2.41504	179.14357	-43.75635
HE 0317-4640	49.73440	-46.49104	256.59974	-55.17100
HE 0323-4529	51.37592	-45.32542	254.03873	-54.47348
HE 0328-1047	52.68905	-10.61947	196.96151	-49.09482
HE 0330-4004	53.03083	-39.91392	244.48254	-54.50688

HE 0330-4144	53.06760	-41.58030	247.29301	-54.19833
HE 0331-4939	53.17434	-49.48593	259.93303	-51.95369
HE 0333-4001	53.85748	-39.86297	244.24142	-53.88639
HE 0336-3829	54.63248	-38.33726	241.56696	-53.46227
HE 0337-5127	54.80474	-51.30453	262.04177	-50.32966
HE 0338-3945	54.97928	-39.59527	243.61252	-53.06426
HE 0339-4027	55.20706	-40.29319	244.72651	-52.80585
HE 0340-3430	55.51998	-34.34728	234.86455	-52.90444
HE 0340-5355	55.39403	-53.77169	265.36046	-49.06134
HE 0341-4024	55.78412	-40.25818	244.57941	-52.37333
HE 0344+0139	56.81575	1.81720	185.74748	-38.74781
HE 0347-1819	57.32664	-18.17817	210.22037	-48.21902
HE 0353-6024	58.49721	-60.25429	272.93804	-44.80073
HE 0400-2917	60.52651	-29.14666	227.29035	-48.20592
HE 0401-0138	60.95786	-1.50070	192.23397	-37.30946
HE 0417-0821	64.88143	-8.23901	202.03656	-37.39842
HE 0430-4404	67.90879	-43.96359	249.00651	-43.11962
HE 0430-4901	67.87979	-48.91151	255.75021	-42.76556
HE 0432-0923	68.60698	-9.28071	205.26890	-34.60405
HE 0436-4008	69.54636	-40.05051	243.70802	-41.87974
HE 0441-4343	70.83514	-43.63905	248.52751	-41.01267
HE 0442-1234	71.21547	-12.47937	210.09021	-33.67107
HE 0447-4858	72.25427	-48.89341	255.40090	-39.90235
HE 0450-4705	72.88998	-47.00118	252.92215	-39.54547
HE 0454-4758	73.86146	-47.89480	254.05959	-38.87213
HE 0501-5139	75.70090	-51.59341	258.71745	-37.56711
HE 0501-5644	75.64698	-56.67249	265.09420	-37.20016
HE 0512-3835	78.49793	-38.53183	242.68139	-34.83634
HE 0513-4557	78.80100	-45.90300	251.67192	-35.44691
HE 0516-3820	79.55386	-38.29242	242.55774	-33.98108
HE 0517-1952	79.82825	-19.82031	221.72628	-28.82767
HE 0519-5525	79.99652	-55.37824	263.28324	-34.86877
HE 0520-1748	80.60779	-17.76864	219.86457	-27.39321
HE 0524-2055	81.76852	-20.87836	223.57787	-27.49938
HE 0534-4615	83.97065	-46.22660	252.48136	-31.90957
HE 0538-4515	84.94228	-45.22583	251.42797	-31.10027
HE 0547-4539	87.30750	-45.65110	252.22017	-29.52951
HE 0858-0016	135.38485	-0.46723	229.59886	28.34557
HE 0926-0508	142.23062	-5.36158	238.67586	31.29729

HE 0938+0114	145.18068	1.00595	234.44064	37.38225
HE 0951-1152	148.57211	-12.10436	249.46365	31.82416
HE 1006-2218	152.25277	-22.55846	260.65586	26.68279
HE 1015-0027	154.39882	-0.70692	243.54533	43.72624
HE 1044-2509	161.81867	-25.42177	270.56912	29.53550
HE 1052-2548	163.83544	-26.08016	272.75346	29.90202
HE 1054-0059	164.19899	-1.25820	254.11759	50.42069
HE 1059-0118	165.51403	-1.57078	256.00386	51.05395
HE 1100-0137	165.73127	-1.89477	256.60011	50.94753
HE 1105+0027	166.95622	0.19397	255.91701	53.33233
HE 1120-0153	170.68125	-2.16068	263.30229	53.74219
HE 1122-1429	171.27781	-14.76787	273.74966	43.15894
HE 1124-2335	171.86225	-23.86823	279.31487	35.12239
HE 1126-1735	172.21411	-17.86188	276.63537	40.75524
HE 1127-1143	172.46095	-12.00352	273.45434	46.14592
HE 1128-0823	172.68466	-8.66524	271.46993	49.21342
HE 1131+0141	173.63386	1.41157	264.06827	58.35668
HE 1132+0125	173.69461	1.15012	264.44075	58.17321
HE 1132+0204	173.71249	1.79106	263.78559	58.71503
HE 1135+0139	174.54105	1.37889	265.55675	58.82780
HE 1135-0344	174.58761	-4.02345	270.61330	54.19744
HE 1148-0037	177.81216	-0.90336	273.18991	58.44915
HE 1207-2031	182.46195	-20.79558	290.00797	41.03012
HE 1210+0048	183.36592	0.53643	282.44309	61.88817
HE 1210-1956	183.21197	-20.21628	290.76476	41.74196
HE 1212-0127	183.82605	-1.73188	284.72079	59.85611
HE 1214-1819	184.25652	-18.59853	291.65738	43.51860
HE 1215+0149	184.42978	1.54242	283.98759	63.16724
HE 1217-0540	184.97347	-5.95451	288.78897	56.04862
HE 1219-0312	185.39225	-3.47772	288.53317	58.55653
HE 1221-0522	186.03199	-5.65316	290.53523	56.55984
HE 1221-1948	185.94896	-20.07941	294.14065	42.32000
HE 1222-0200	186.37235	-2.28992	289.91349	59.92432
HE 1222-0336	186.21828	-3.88516	290.23622	58.33026
HE 1225+0155	187.01982	1.64245	289.56262	63.90622
HE 1225-0515	187.05173	-5.52800	292.31407	56.86406
HE 1230-1724	188.23779	-17.69102	296.70410	44.95707
HE 1237-3103	190.06097	-31.33568	300.12924	31.47515
HE 1243-1425	191.61687	-14.69262	301.12978	48.16173

HE 1245-1616	191.98648	-16.54559	301.72020	46.31794
HE 1246-1344	192.33434	-14.01158	302.15750	48.85701
HE 1247-2114	192.52131	-21.51322	302.51277	41.35743
HE 1248-1800	192.86641	-18.27502	302.94116	44.59673
HE 1249-2932	193.07650	-29.81577	303.15657	33.05560
HE 1249-3121	193.02137	-31.62921	303.09314	31.24234
HE 1251-0104	193.46694	-1.34324	304.20566	61.52250
HE 1252+0044	193.84205	0.46686	305.12074	63.32190
HE 1252-0117	193.74930	-1.55975	304.78437	61.29920
HE 1254+0009	194.30375	-0.11099	306.08485	62.72539
HE 1256-0228	194.66026	-2.73822	306.54022	60.08306
HE 1256-0651	194.80439	-7.12231	306.35780	55.69769
HE 1259-0621	195.46305	-6.62064	307.57920	56.15710
HE 1300+0157	195.73432	1.69779	309.59963	64.42057
HE 1300-0641	195.89224	-6.95579	308.29168	55.78967
HE 1300-0642	195.84745	-6.97315	308.21032	55.77606
HE 1300-2201	195.82217	-22.29385	306.53737	40.49492
HE 1300-2431	195.75015	-24.78674	306.26321	38.01021
HE 1305-0331	196.99554	-3.79459	310.92227	58.82025
HE 1311-1412	198.42496	-14.47354	311.00710	48.04885
HE 1314-3036	199.37174	-30.86409	309.50065	31.67520
HE 1320-1339	200.68370	-13.92539	314.37721	48.24964
HE 1330-0354	203.29438	-4.16852	322.36708	57.11984
HE 1330-0607	203.23570	-6.37521	321.12712	55.02357
HE 1332-0309	203.65782	-3.41469	323.43508	57.72739
HE 1333-0340	203.96403	-3.93011	323.67330	57.14207
HE 1335+0135	204.47442	1.34085	328.23759	61.90829
HE 1337+0012	205.00937	-0.03890	328.17626	60.42878
HE 1337-0453	204.99258	-5.14215	324.71722	55.66331
HE 1343-0640	206.53754	-6.92970	326.15060	53.45752
HE 1345-0206	207.06664	-2.36303	330.07295	57.48313
HE 1351-1049	208.48800	-11.07346	326.64575	48.89856
HE 1413-1954	214.01954	-20.14836	328.58034	38.47147
HE 1419-1759	215.57373	-18.22492	331.34810	39.58125
HE 1421-2006	215.95998	-20.33629	330.56981	37.52687
HE 1430+0053	218.31879	0.68018	349.91215	53.99040
HE 1430-0026	218.31777	-0.66336	348.45936	52.96197
HE 1430-1123	218.39015	-11.61875	338.87511	44.01087
HE 1431-2142	218.52795	-21.92146	332.31903	35.02447

HE 1500-1628	225.73596	-16.66868	342.82251	35.82057
HE 2133-1432	324.09390	-14.32236	38.50148	-42.93710
HE 2134+0001	324.28412	0.25124	55.10562	-35.93320
HE 2139-1851	325.62298	-18.63077	33.67755	-45.91306
HE 2143+0030	326.55031	0.74605	57.23755	-37.50169
HE 2145-3025	327.18057	-30.18566	17.38038	-50.06456
HE 2150-0825	328.25062	-8.18843	48.56836	-43.79529
HE 2151-2858	328.50665	-28.73902	19.88543	-51.00861
HE 2153-2719	329.01700	-27.08051	22.60868	-51.17926
HE 2154-2838	329.43248	-28.40857	20.60452	-51.76286
HE 2155+0136	329.40650	1.83888	60.53442	-39.13224
HE 2156-3130	329.77409	-31.27005	16.03770	-52.39678
HE 2158-3112	330.33959	-30.96606	16.60609	-52.85257
HE 2200-2030	330.76059	-20.26632	33.76196	-51.02547
HE 2201-0637	330.93644	-6.37823	52.67447	-45.13301
HE 2204-1703	331.79959	-16.81965	39.42743	-50.74225
HE 2206-2245	332.28932	-22.50456	30.96303	-53.04363
HE 2216-0621	334.69144	-6.11397	55.99873	-48.09862
HE 2216-1548	334.87650	-15.56012	43.20848	-52.94815
HE 2217-0706	335.07500	-6.85461	55.40020	-48.83094
HE 2217-1523	335.14054	-15.14301	44.01484	-53.00335
HE 2219-0713	335.56573	-6.97628	55.66380	-49.30243
HE 2221-4150	336.19708	-41.59422	357.53853	-56.78498
HE 2222-4156	336.36940	-41.68273	357.32395	-56.88814
HE 2224+0143	336.84636	1.97581	67.12897	-44.72836
HE 2224-4103	336.95125	-40.80692	358.69851	-57.52392
HE 2226-4102	337.26792	-40.78126	358.63905	-57.76292
HE 2227-4044	337.57938	-40.48710	359.07128	-58.06239
HE 2228-3806	337.76075	-37.84466	3.95723	-58.73362
HE 2229-4153	338.20435	-41.64045	356.73014	-58.22213
HE 2231-0622	338.58376	-6.10854	59.49386	-51.24013
HE 2234-0521	339.15715	-5.10153	61.32173	-51.07989
HE 2238-2152	340.29292	-21.60564	36.31450	-59.91177
HE 2240-0412	340.74199	-3.94305	64.35780	-51.56883
HE 2242-1930	341.32163	-19.24773	41.40002	-60.04850
HE 2243-0151	341.53692	-1.59866	67.98221	-50.59709
HE 2244-1503	341.85763	-14.79171	49.76577	-58.64817
HE 2247-3705	342.62295	-36.82123	4.52471	-62.72270
HE 2248-3345	342.93661	-33.49038	11.71490	-63.49563

HE 2250-2132	343.41876	-21.27344	38.80765	-62.58390
HE 2252-4157	343.89257	-41.69148	353.81841	-62.21839
HE 2252-4225	343.74403	-42.15540	352.99535	-61.93750
HE 2258-3456	345.24903	-34.67828	8.38156	-65.22797
HE 2259-3407	345.56560	-33.85317	10.23650	-65.62062
HE 2301-4024	346.05842	-40.13908	355.63292	-64.32146
HE 2301-4126	345.95907	-41.17396	353.52222	-63.84628
HE 2304-4153	346.77373	-41.62503	351.99961	-64.21003
HE 2311+0129	348.58908	1.75673	80.07341	-52.84147
HE 2314-1554	349.25471	-15.63046	55.79376	-65.26056
HE 2319-0852	350.57220	-8.60472	70.07234	-61.93984
HE 2325-0755	351.99846	-7.65396	73.64980	-62.24778
HE 2326+0038	352.23744	0.91010	84.31347	-55.65075
HE 2327-5642	352.65464	-56.43737	323.64233	-57.32154
HE 2329-3702	353.07578	-36.76616	358.05627	-70.70066
HE 2333-1358	353.95222	-13.69188	66.44214	-67.81558
HE 2334-0604	354.36953	-5.79908	80.09687	-62.35007
HE 2335-5958	354.58038	-59.70146	318.98299	-55.08955
HE 2338-1311	355.28486	-12.91937	70.29512	-68.26682
HE 2338-1618	355.15169	-16.02417	63.37700	-70.17787
HE 2345-1919	356.98160	-19.04398	58.58188	-73.32844
HE 2347-1254	357.54190	-12.63093	75.22835	-69.60442
HE 2347-1334	357.61178	-13.29422	74.05910	-70.13612
HE 2347-1448	357.49319	-14.53771	71.18074	-70.93624

Table 13: Equatorial an Galactic coordinates of 253 very metal-poor stars under investigation Barklem et al. (2005).

target ID	D_π kpc	D_L kpc	D_{BJg} kpc	D_{BJpg} kpc
CS 22175-007	$3.3\ ^{+0.18}_{-0.16}$	$2.89\ ^{+0.21}_{-0.19}$	$2.91\ ^{+0.14}_{-0.13}$	$2.96\ ^{+0.1}_{-0.17}$
CS 22186-023	$3.24\ ^{+0.12}_{-0.11}$	$3.08\ ^{+0.21}_{-0.19}$	$3.06\ ^{+0.1}_{-0.08}$	$3.05\ ^{+0.11}_{-0.07}$
CS 22186-025	$11.15\ ^{+1.87}_{-1.4}$	$7.99\ ^{+1.72}_{-1.2}$	$7.61\ ^{+0.97}_{-0.63}$	$7.36\ ^{+1.22}_{-0.39}$
CS 22886-042	$4.94\ ^{+0.56}_{-0.46}$	$4.25\ ^{+0.56}_{-0.44}$	$4.2\ ^{+0.38}_{-0.35}$	$4.4\ ^{+0.18}_{-0.55}$
CS 22892-052	$6.24\ ^{+1.08}_{-0.8}$	$5.26\ ^{+0.97}_{-0.71}$	$5.19\ ^{+0.63}_{-0.49}$	$4.83\ ^{+1.0}_{-0.13}$
CS 22945-028	$4.07\ ^{+0.28}_{-0.24}$	$3.54\ ^{+0.33}_{-0.28}$	$3.53\ ^{+0.2}_{-0.19}$	$3.52\ ^{+0.21}_{-0.17}$
CS 22957-013	$9.52\ ^{+2.18}_{-1.5}$	$6.72\ ^{+1.47}_{-1.02}$	$6.59\ ^{+1.02}_{-0.74}$	$5.71\ ^{+1.9}_{--0.13}$

CS 22958-083	$4.52^{+0.3}_{-0.26}$	$3.9^{+0.38}_{-0.32}$	$3.94^{+0.2}_{-0.22}$	$3.8^{+0.34}_{-0.08}$
CS 22960-010	$0.44^{+0.0}_{-0.0}$	$0.43^{+0.0}_{-0.0}$	$0.43^{+0.0}_{-0.0}$	$0.44^{+0.0}_{-0.01}$
CS 29491-069	$2.43^{+0.11}_{-0.1}$	$2.29^{+0.14}_{-0.13}$	$2.27^{+0.1}_{-0.09}$	$2.26^{+0.12}_{-0.08}$
CS 29491-109	$8.29^{+1.77}_{-1.24}$	$6.84^{+1.61}_{-1.09}$	$6.59^{+0.91}_{-0.82}$	$5.97^{+1.52}_{-0.21}$
CS 29497-004	$4.8^{+0.42}_{-0.35}$	$3.99^{+0.43}_{-0.36}$	$3.93^{+0.28}_{-0.26}$	$3.92^{+0.29}_{-0.25}$
CS 29510-058	$2.97^{+0.15}_{-0.13}$	$2.65^{+0.18}_{-0.16}$	$2.65^{+0.1}_{-0.1}$	$2.61^{+0.14}_{-0.06}$
CS 30308-035	$7.81^{+1.38}_{-1.02}$	$5.87^{+1.07}_{-0.79}$	$5.93^{+0.73}_{-0.55}$	$4.91^{+1.75}_{--0.46}$
CS 30315-001	$14.66^{+5.41}_{-3.11}$	$9.06^{+2.75}_{-1.71}$	$8.47^{+1.29}_{-1.03}$	$7.85^{+1.9}_{-0.42}$
CS 30315-029	$14.52^{+4.35}_{-2.72}$	$9.01^{+2.49}_{-1.6}$	$8.34^{+1.32}_{-0.98}$	$7.72^{+1.95}_{-0.35}$
CS 30337-097	$9.71^{+3.23}_{-1.94}$	$7.53^{+2.33}_{-1.44}$	$7.24^{+1.04}_{-1.09}$	$6.62^{+1.67}_{-0.47}$
CS 30339-041	$6.46^{+0.66}_{-0.55}$	$5.11^{+0.68}_{-0.54}$	$5.16^{+0.4}_{-0.39}$	$4.95^{+0.62}_{-0.18}$
CS 30343-063	$12.59^{+3.1}_{-2.08}$	$10.48^{+3.5}_{-2.1}$	$10.29^{+1.74}_{-1.37}$	$10.49^{+1.53}_{-1.57}$
CS 31060-047	$11.59^{+2.54}_{-1.76}$	$7.73^{+1.74}_{-1.2}$	$7.34^{+0.83}_{-0.72}$	$8.18^{+-0.01}_{-1.55}$
CS 31062-041	$15.44^{+7.04}_{-3.68}$	$9.27^{+3.11}_{-1.86}$	$8.77^{+2.49}_{-1.15}$	$7.53^{+3.73}_{--0.1}$
CS 31072-118	$6.0^{+0.45}_{-0.39}$	$5.78^{+0.81}_{-0.63}$	$5.84^{+0.33}_{-0.49}$	$5.34^{+0.82}_{--0.01}$
CS 31082-001	$2.17^{+0.13}_{-0.12}$	$2.03^{+0.14}_{-0.12}$	$2.03^{+0.12}_{-0.09}$	$1.93^{+0.22}_{--0.01}$
HD 20	$0.5^{+0.01}_{-0.01}$	$0.49^{+0.01}_{-0.01}$	$0.49^{+0.01}_{-0.0}$	$0.49^{+0.01}_{-0.0}$
HD 221170	$0.55^{+0.01}_{-0.01}$	$0.54^{+0.01}_{-0.01}$	$0.54^{+0.01}_{-0.01}$	$0.54^{+0.01}_{-0.01}$
HE 0005-0002	$13.45^{+12.46}_{-4.37}$	$8.48^{+4.37}_{-2.15}$	$6.93^{+1.83}_{-1.43}$	$6.04^{+2.73}_{-0.54}$
HE 0008-3842	$18.32^{+5.7}_{-3.52}$	$11.06^{+3.59}_{-2.18}$	$11.06^{+1.43}_{-1.22}$	$10.1^{+2.38}_{-0.26}$
HE 0017-4838	$32.12^{+-454.99}_{-16.65}$	$14.17^{+16.54}_{-4.96}$	$10.05^{+4.13}_{-2.21}$	$11.48^{+2.7}_{-3.64}$
HE 0018-1349	$1.36^{+0.07}_{-0.07}$	$1.28^{+0.07}_{-0.06}$	$1.29^{+0.06}_{-0.07}$	$1.29^{+0.06}_{-0.07}$
HE 0023-4825	$1.16^{+0.02}_{-0.02}$	$1.11^{+0.03}_{-0.03}$	$1.11^{+0.02}_{-0.02}$	$1.11^{+0.01}_{-0.02}$
HE 0029-1839	$6.22^{+1.31}_{-0.92}$	$4.9^{+0.95}_{-0.69}$	$4.74^{+0.65}_{-0.52}$	$5.56^{+-0.18}_{-1.35}$
HE 0037-2657	$7.2^{+1.07}_{-0.82}$	$5.53^{+0.9}_{-0.68}$	$5.43^{+0.6}_{-0.46}$	$4.99^{+1.04}_{-0.02}$
HE 0039-4154	$9.76^{+1.58}_{-1.19}$	$7.09^{+1.38}_{-0.99}$	$6.84^{+0.67}_{-0.62}$	$7.09^{+0.42}_{-0.86}$
HE 0043-2845	$0.75^{+0.02}_{-0.02}$	$0.73^{+0.02}_{-0.02}$	$0.73^{+0.02}_{-0.02}$	$0.74^{+0.0}_{-0.03}$
HE 0044-2459	$2.78^{+0.16}_{-0.14}$	$2.49^{+0.17}_{-0.15}$	$2.48^{+0.11}_{-0.11}$	$2.5^{+0.09}_{-0.13}$
HE 0044-4023	$4.44^{+1.25}_{-0.8}$	$3.8^{+0.95}_{-0.63}$	$3.63^{+0.59}_{-0.52}$	$3.29^{+0.94}_{-0.17}$
HE 0045-2430	$3.9^{+0.46}_{-0.37}$	$3.34^{+0.4}_{-0.33}$	$3.35^{+0.34}_{-0.27}$	$3.16^{+0.52}_{-0.09}$
HE 0049-5700	$2.08^{+0.13}_{-0.11}$	$1.92^{+0.13}_{-0.11}$	$1.93^{+0.11}_{-0.09}$	$1.96^{+0.08}_{-0.13}$
HE 0051-2304	$17.47^{+18.26}_{-5.91}$	$10.04^{+5.29}_{-2.57}$	$8.64^{+2.78}_{-1.48}$	$7.78^{+3.64}_{-0.62}$

HE 0054-0657	$0.97^{+0.03}_{-0.03}$	$0.93^{+0.03}_{-0.03}$	$0.93^{+0.02}_{-0.02}$	$0.94^{+0.01}_{-0.03}$
HE 0057-4541	$5.92^{+0.73}_{-0.58}$	$4.81^{+0.68}_{-0.53}$	$4.8^{+0.5}_{-0.41}$	$4.56^{+0.74}_{-0.17}$
HE 0104-4007	$7.6^{+2.3}_{-1.43}$	$5.8^{+1.51}_{-0.99}$	$5.35^{+0.85}_{-0.72}$	$5.46^{+0.74}_{-0.82}$
HE 0104-5300	$10.01^{+1.26}_{-1.01}$	$7.38^{+1.37}_{-1.0}$	$7.28^{+0.6}_{-0.55}$	$7.31^{+0.57}_{-0.58}$
HE 0105-6141	$2.3^{+0.06}_{-0.06}$	$2.13^{+0.1}_{-0.09}$	$2.14^{+0.05}_{-0.05}$	$2.12^{+0.06}_{-0.03}$
HE 0109-0742	$9.54^{+2.97}_{-1.83}$	$6.73^{+1.76}_{-1.15}$	$6.15^{+1.12}_{-0.82}$	$5.58^{+1.68}_{-0.25}$
HE 0109-3711	$3.66^{+0.7}_{-0.51}$	$3.26^{+0.6}_{-0.44}$	$3.26^{+0.46}_{-0.47}$	$3.11^{+0.61}_{-0.32}$
HE 0111-1454	$6.35^{+0.75}_{-0.6}$	$5.66^{+0.91}_{-0.69}$	$5.58^{+0.61}_{-0.44}$	$5.39^{+0.8}_{-0.25}$
HE 0121-2826	$13.18^{+10.12}_{-3.99}$	$8.49^{+3.98}_{-2.05}$	$7.28^{+1.39}_{-1.17}$	$5.61^{+3.05}_{--0.5}$
HE 0131-2740	$3.73^{+0.3}_{-0.26}$	$3.23^{+0.31}_{-0.26}$	$3.2^{+0.2}_{-0.13}$	$3.05^{+0.34}_{--0.02}$
HE 0131-3953	$1.42^{+0.1}_{-0.08}$	$1.34^{+0.09}_{-0.08}$	$1.35^{+0.1}_{-0.07}$	$1.36^{+0.09}_{-0.08}$
HE 0143-1135	$0.97^{+0.03}_{-0.03}$	$0.93^{+0.03}_{-0.03}$	$0.93^{+0.03}_{-0.03}$	$0.93^{+0.02}_{-0.04}$
HE 0143-4108	$8.37^{+1.99}_{-1.35}$	$6.3^{+1.42}_{-0.98}$	$6.07^{+0.77}_{-0.78}$	$7.98^{+-1.14}_{-2.69}$
HE 0143-4146	$13.78^{+4.69}_{-2.79}$	$9.03^{+2.74}_{-1.7}$	$8.61^{+1.43}_{-1.23}$	$7.23^{+2.8}_{--0.14}$
HE 0157-3335	$23.18^{+17.48}_{-6.97}$	$12.17^{+5.59}_{-2.91}$	$10.35^{+2.34}_{-1.76}$	$7.45^{+5.25}_{--1.15}$
HE 0200-0955	$4.15^{+0.45}_{-0.37}$	$3.52^{+0.41}_{-0.33}$	$3.44^{+0.3}_{-0.25}$	$3.17^{+0.57}_{--0.02}$
HE 0202-2204	$10.77^{+5.46}_{-2.71}$	$7.4^{+2.69}_{-1.56}$	$6.52^{+1.31}_{-1.03}$	$6.33^{+1.5}_{-0.84}$
HE 0231-4016	$2.63^{+0.22}_{-0.19}$	$2.39^{+0.21}_{-0.18}$	$2.37^{+0.14}_{-0.16}$	$2.4^{+0.11}_{-0.19}$
HE 0240-0807	$111.43^{+-164.67}_{-84.21}$	$19.32^{+34.25}_{-7.54}$	$11.83^{+3.98}_{-2.23}$	$10.86^{+4.94}_{-1.27}$
HE 0240-6105	$21.35^{+10.2}_{-5.22}$	$12.44^{+5.14}_{-2.81}$	$11.4^{+1.74}_{-1.57}$	$10.67^{+2.46}_{-0.84}$
HE 0243-0753	$6.63^{+0.64}_{-0.54}$	$5.17^{+0.68}_{-0.54}$	$5.17^{+0.36}_{-0.34}$	$4.9^{+0.63}_{-0.07}$
HE 0243-5238	$3.65^{+0.2}_{-0.18}$	$3.24^{+0.26}_{-0.22}$	$3.25^{+0.15}_{-0.15}$	$3.21^{+0.19}_{-0.12}$
HE 0244-4111	$2.38^{+0.11}_{-0.1}$	$2.18^{+0.13}_{-0.12}$	$2.18^{+0.1}_{-0.08}$	$2.1^{+0.18}_{-0.0}$
HE 0248+0039	$10.23^{+6.01}_{-2.76}$	$7.05^{+2.81}_{-1.56}$	$5.75^{+1.46}_{-0.7}$	$6.69^{+0.52}_{-1.64}$
HE 0256-1109	$1.1^{+0.06}_{-0.05}$	$1.05^{+0.05}_{-0.05}$	$1.05^{+0.05}_{-0.05}$	$1.07^{+0.03}_{-0.07}$
HE 0300-0751	$21.78^{+-2258.27}_{-10.94}$	$12.03^{+17.94}_{-4.51}$	$7.13^{+2.22}_{-1.37}$	$5.9^{+3.45}_{-0.14}$
HE 0305-4520	$12.16^{+1.98}_{-1.5}$	$8.55^{+1.91}_{-1.32}$	$8.28^{+0.82}_{-0.7}$	$7.33^{+1.77}_{--0.26}$
HE 0308-1154	$15.12^{+26.43}_{-5.88}$	$9.18^{+6.66}_{-2.72}$	$6.38^{+1.46}_{-0.99}$	$7.32^{+0.52}_{-1.93}$
HE 0315+0000	$49.03^{+-90.79}_{-33.58}$	$15.63^{+46.33}_{-6.69}$	$9.47^{+3.95}_{-2.83}$	$8.8^{+4.61}_{-2.17}$
HE 0316+0214	$112.06^{+-152.05}_{-88.72}$	$19.08^{+52.39}_{-8.07}$	$9.79^{+2.3}_{-1.72}$	$8.39^{+3.7}_{-0.32}$
HE 0317-4640	$7.33^{+11.16}_{-2.76}$	$5.97^{+6.06}_{-2.0}$	$5.08^{+1.52}_{-1.5}$	$3.49^{+3.11}_{--0.09}$
HE 0323-4529	$7.15^{+0.98}_{-0.77}$	$5.69^{+0.93}_{-0.7}$	$5.45^{+0.53}_{-0.42}$	$6.08^{+-0.1}_{-1.04}$

HE 0328-1047	$5.18^{+0.58}_{-0.47}$	$4.25^{+0.54}_{-0.43}$	$4.22^{+0.28}_{-0.24}$	$4.85^{+-0.34}_{-0.86}$
HE 0330-4004	$3.59^{+0.84}_{-0.57}$	$3.19^{+0.69}_{-0.48}$	$3.41^{+0.69}_{-0.6}$	$2.97^{+1.13}_{-0.16}$
HE 0330-4144	$1.85^{+0.11}_{-0.1}$	$1.73^{+0.11}_{-0.1}$	$1.74^{+0.09}_{-0.1}$	$1.74^{+0.09}_{-0.1}$
HE 0331-4939	$7.55^{+1.5}_{-1.08}$	$5.93^{+1.2}_{-0.86}$	$5.6^{+0.52}_{-0.61}$	$5.73^{+0.39}_{-0.74}$
HE 0333-4001	$1.5^{+0.07}_{-0.06}$	$1.42^{+0.07}_{-0.07}$	$1.41^{+0.06}_{-0.06}$	$1.45^{+0.02}_{-0.09}$
HE 0336-3829	$4.83^{+1.21}_{-0.8}$	$4.2^{+0.98}_{-0.67}$	$4.01^{+0.65}_{-0.54}$	$3.7^{+0.96}_{-0.23}$
HE 0337-5127	$6.34^{+1.03}_{-0.78}$	$5.15^{+0.88}_{-0.66}$	$5.09^{+0.4}_{-0.51}$	$4.84^{+0.64}_{-0.26}$
HE 0338-3945	$1.54^{+0.05}_{-0.05}$	$1.45^{+0.06}_{-0.06}$	$1.45^{+0.04}_{-0.05}$	$1.45^{+0.05}_{-0.04}$
HE 0339-4027	$0.85^{+0.01}_{-0.01}$	$0.82^{+0.02}_{-0.02}$	$0.82^{+0.01}_{-0.01}$	$0.82^{+0.02}_{-0.01}$
HE 0340-3430	$1.78^{+0.06}_{-0.06}$	$1.67^{+0.07}_{-0.07}$	$1.67^{+0.08}_{-0.06}$	$1.67^{+0.08}_{-0.06}$
HE 0340-5355	$24.72^{+25.78}_{-8.35}$	$13.31^{+7.63}_{-3.55}$	$11.14^{+1.98}_{-1.75}$	$9.12^{+4.0}_{--0.26}$
HE 0341-4024	$0.64^{+0.0}_{-0.0}$	$0.62^{+0.01}_{-0.01}$	$0.62^{+0.0}_{-0.0}$	$0.62^{+0.01}_{-0.0}$
HE 0344+0139	$1.36^{+0.07}_{-0.06}$	$1.29^{+0.07}_{-0.06}$	$1.28^{+0.06}_{-0.05}$	$1.27^{+0.06}_{-0.05}$
HE 0347-1819	$0.7^{+0.02}_{-0.02}$	$0.68^{+0.02}_{-0.02}$	$0.68^{+0.02}_{-0.02}$	$0.7^{+0.0}_{-0.03}$
HE 0353-6024	$8.76^{+4.36}_{-2.18}$	$6.97^{+2.88}_{-1.58}$	$6.44^{+1.71}_{-1.26}$	$5.32^{+2.82}_{-0.15}$
HE 0400-2917	$5.23^{+0.38}_{-0.33}$	$4.37^{+0.47}_{-0.39}$	$4.27^{+0.2}_{-0.19}$	$4.36^{+0.11}_{-0.28}$
HE 0401-0138	$5.87^{+0.59}_{-0.49}$	$4.7^{+0.59}_{-0.47}$	$4.71^{+0.31}_{-0.32}$	$4.49^{+0.52}_{-0.11}$
HE 0417-0821	$0.58^{+0.01}_{-0.01}$	$0.56^{+0.01}_{-0.01}$	$0.56^{+0.01}_{-0.01}$	$0.57^{+0.01}_{-0.01}$
HE 0430-4404	$1.57^{+0.08}_{-0.07}$	$1.48^{+0.08}_{-0.07}$	$1.47^{+0.09}_{-0.06}$	$1.5^{+0.05}_{-0.1}$
HE 0430-4901	$2.47^{+0.09}_{-0.09}$	$2.28^{+0.13}_{-0.11}$	$2.29^{+0.08}_{-0.06}$	$2.29^{+0.08}_{-0.06}$
HE 0432-0923	$9.16^{+2.63}_{-1.67}$	$6.62^{+1.66}_{-1.11}$	$6.24^{+0.92}_{-0.93}$	$6.88^{+0.28}_{-1.58}$
HE 0436-4008	$4.85^{+0.62}_{-0.49}$	$4.11^{+0.57}_{-0.44}$	$4.04^{+0.5}_{-0.38}$	$4.15^{+0.39}_{-0.48}$
HE 0441-4343	$3.51^{+0.28}_{-0.24}$	$3.11^{+0.3}_{-0.25}$	$3.1^{+0.2}_{-0.17}$	$3.0^{+0.29}_{-0.08}$
HE 0442-1234	$5.74^{+0.62}_{-0.51}$	$5.39^{+0.83}_{-0.63}$	$5.4^{+0.36}_{-0.46}$	$5.12^{+0.64}_{-0.18}$
HE 0447-4858	$3.26^{+0.37}_{-0.3}$	$2.96^{+0.35}_{-0.29}$	$2.92^{+0.26}_{-0.22}$	$2.92^{+0.26}_{-0.22}$
HE 0450-4705	$2.31^{+0.08}_{-0.07}$	$2.14^{+0.11}_{-0.1}$	$2.15^{+0.06}_{-0.06}$	$2.1^{+0.11}_{-0.01}$
HE 0454-4758	$1.7^{+0.03}_{-0.03}$	$1.61^{+0.06}_{-0.05}$	$1.61^{+0.03}_{-0.02}$	$1.6^{+0.04}_{-0.01}$
HE 0501-5139	$4.54^{+0.75}_{-0.56}$	$3.93^{+0.65}_{-0.49}$	$3.87^{+0.58}_{-0.46}$	$3.61^{+0.83}_{-0.2}$
HE 0501-5644	$13.35^{+6.11}_{-3.19}$	$9.17^{+3.42}_{-1.96}$	$8.25^{+1.76}_{-1.52}$	$9.0^{+1.01}_{-2.28}$
HE 0512-3835	$18.01^{+8.48}_{-4.37}$	$10.95^{+4.19}_{-2.37}$	$9.41^{+1.44}_{-1.14}$	$8.66^{+2.19}_{-0.39}$
HE 0513-4557	$3.6^{+0.38}_{-0.31}$	$3.18^{+0.36}_{-0.29}$	$3.2^{+0.31}_{-0.24}$	$3.06^{+0.44}_{-0.1}$
HE 0516-3820	$3.0^{+0.12}_{-0.11}$	$2.71^{+0.17}_{-0.15}$	$2.72^{+0.07}_{-0.09}$	$2.68^{+0.11}_{-0.05}$

HE 0517-1952	$9.95^{+2.19}_{-1.52}$	$7.13^{+1.59}_{-1.1}$	$6.53^{+0.75}_{-0.6}$	$6.56^{+0.72}_{-0.62}$
HE 0519-5525	$2.38^{+0.11}_{-0.1}$	$2.2^{+0.13}_{-0.12}$	$2.19^{+0.09}_{-0.08}$	$2.15^{+0.13}_{-0.04}$
HE 0520-1748	$3.39^{+0.33}_{-0.28}$	$2.98^{+0.31}_{-0.26}$	$2.9^{+0.25}_{-0.23}$	$2.83^{+0.33}_{-0.15}$
HE 0524-2055	$10.45^{+1.78}_{-1.33}$	$7.48^{+1.53}_{-1.09}$	$7.32^{+0.67}_{-0.5}$	$7.32^{+0.67}_{-0.49}$
HE 0534-4615	$2.27^{+0.1}_{-0.09}$	$2.1^{+0.12}_{-0.11}$	$2.11^{+0.1}_{-0.09}$	$2.08^{+0.12}_{-0.07}$
HE 0538-4515	$1.67^{+0.06}_{-0.06}$	$1.57^{+0.07}_{-0.07}$	$1.58^{+0.05}_{-0.05}$	$1.58^{+0.05}_{-0.06}$
HE 0547-4539	$2.07^{+0.04}_{-0.04}$	$2.02^{+0.09}_{-0.08}$	$2.01^{+0.04}_{-0.03}$	$2.02^{+0.03}_{-0.04}$
HE 0858-0016	$30.47^{+87.55}_{-12.98}$	$13.18^{+8.75}_{-3.76}$	$10.05^{+1.93}_{-1.57}$	$9.58^{+2.41}_{-1.09}$
HE 0926-0508	$0.46^{+0.01}_{-0.01}$	$0.45^{+0.01}_{-0.01}$	$0.45^{+0.01}_{-0.01}$	$0.45^{+0.01}_{-0.02}$
HE 0938+0114	$0.18^{+0.0}_{-0.0}$	$0.18^{+0.0}_{-0.0}$	$0.18^{+0.0}_{-0.0}$	$0.18^{+0.0}_{-0.0}$
HE 0951-1152	$0.67^{+0.02}_{-0.02}$	$0.65^{+0.02}_{-0.02}$	$0.65^{+0.02}_{-0.02}$	$0.67^{+0.01}_{-0.03}$
HE 1006-2218	$0.93^{+0.02}_{-0.01}$	$0.89^{+0.02}_{-0.02}$	$0.89^{+0.02}_{-0.01}$	$0.89^{+0.02}_{-0.01}$
HE 1015-0027	$1.89^{+0.15}_{-0.13}$	$1.74^{+0.14}_{-0.12}$	$1.74^{+0.1}_{-0.1}$	$1.72^{+0.12}_{-0.09}$
HE 1044-2509	$3.97^{+0.36}_{-0.31}$	$3.41^{+0.36}_{-0.29}$	$3.44^{+0.26}_{-0.22}$	$3.3^{+0.4}_{-0.08}$
HE 1052-2548	$0.68^{+0.01}_{-0.01}$	$0.66^{+0.01}_{-0.01}$	$0.66^{+0.01}_{-0.01}$	$0.66^{+0.01}_{-0.01}$
HE 1054-0059	$27.74^{+46.34}_{-10.67}$	$12.56^{+7.15}_{-3.34}$	$10.4^{+2.01}_{-1.76}$	$9.58^{+2.83}_{-0.93}$
HE 1059-0118	$0.97^{+0.04}_{-0.04}$	$0.93^{+0.04}_{-0.04}$	$0.94^{+0.03}_{-0.04}$	$0.95^{+0.02}_{-0.06}$
HE 1100-0137	$1.88^{+0.17}_{-0.15}$	$1.74^{+0.16}_{-0.14}$	$1.78^{+0.14}_{-0.13}$	$1.8^{+0.13}_{-0.14}$
HE 1105+0027	$3.16^{+0.4}_{-0.32}$	$2.78^{+0.35}_{-0.28}$	$2.81^{+0.23}_{-0.32}$	$2.68^{+0.36}_{-0.19}$
HE 1120-0153	$0.51^{+0.01}_{-0.01}$	$0.5^{+0.01}_{-0.01}$	$0.5^{+0.01}_{-0.01}$	$0.5^{+0.01}_{-0.01}$
HE 1122-1429	$2.8^{+0.42}_{-0.32}$	$2.55^{+0.37}_{-0.29}$	$2.54^{+0.31}_{-0.24}$	$2.59^{+0.25}_{-0.29}$
HE 1124-2335	$4.67^{+0.54}_{-0.44}$	$3.89^{+0.49}_{-0.39}$	$3.83^{+0.35}_{-0.29}$	$3.88^{+0.29}_{-0.34}$
HE 1126-1735	$4.12^{+0.77}_{-0.56}$	$3.48^{+0.6}_{-0.45}$	$3.51^{+0.51}_{-0.47}$	$3.14^{+0.88}_{-0.1}$
HE 1127-1143	$13.11^{+15.82}_{-4.63}$	$8.31^{+5.04}_{-2.28}$	$6.76^{+1.81}_{-1.52}$	$5.76^{+2.81}_{-0.52}$
HE 1128-0823	$2.41^{+0.21}_{-0.18}$	$2.18^{+0.19}_{-0.16}$	$2.2^{+0.15}_{-0.16}$	$2.12^{+0.23}_{-0.08}$
HE 1131+0141	$9.37^{+8.69}_{-3.04}$	$6.84^{+4.07}_{-1.86}$	$5.45^{+1.17}_{-0.98}$	$3.88^{+2.74}_{--0.59}$
HE 1132+0125	$1.73^{+0.17}_{-0.15}$	$1.61^{+0.16}_{-0.13}$	$1.61^{+0.16}_{-0.11}$	$1.66^{+0.11}_{-0.16}$
HE 1132+0204	$6.88^{+1.52}_{-1.06}$	$5.29^{+1.08}_{-0.76}$	$5.16^{+0.74}_{-0.56}$	$4.98^{+0.92}_{-0.37}$
HE 1135+0139	$16.66^{+35.36}_{-6.74}$	$9.65^{+7.29}_{-2.9}$	$7.32^{+2.24}_{-1.66}$	$7.02^{+2.54}_{-1.36}$
HE 1135-0344	$3.08^{+0.51}_{-0.38}$	$2.71^{+0.42}_{-0.32}$	$2.68^{+0.44}_{-0.28}$	$2.55^{+0.57}_{-0.15}$
HE 1148-0037	$1.43^{+0.04}_{-0.04}$	$1.34^{+0.05}_{-0.04}$	$1.34^{+0.03}_{-0.03}$	$1.34^{+0.04}_{-0.02}$
HE 1207-2031	$2.9^{+0.44}_{-0.34}$	$2.63^{+0.39}_{-0.3}$	$2.63^{+0.36}_{-0.28}$	$2.6^{+0.39}_{-0.25}$

HE 1210+0048	$1.75^{+0.13}_{-0.12}$	$1.63^{+0.13}_{-0.11}$	$1.66^{+0.14}_{-0.1}$	$1.65^{+0.15}_{-0.09}$
HE 1210-1956	$2.47^{+0.33}_{-0.26}$	$2.28^{+0.3}_{-0.24}$	$2.38^{+0.3}_{-0.27}$	$2.31^{+0.36}_{-0.21}$
HE 1212-0127	$36.69^{+-80.24}_{-23.78}$	$14.43^{+48.26}_{-6.28}$	$7.74^{+3.09}_{-1.93}$	$10.4^{+0.43}_{-4.59}$
HE 1214-1819	$-16835.02^{+16804.71}_{--16865.43}$	$22.93^{+141.69}_{-10.61}$	$11.21^{+3.16}_{-2.5}$	$8.59^{+5.77}_{--0.11}$
HE 1215+0149	$18.65^{+111.61}_{-8.61}$	$10.71^{+11.99}_{-3.7}$	$7.46^{+2.12}_{-1.57}$	$7.55^{+2.04}_{-1.65}$
HE 1217-0540	$0.81^{+0.02}_{-0.02}$	$0.78^{+0.02}_{-0.02}$	$0.78^{+0.02}_{-0.02}$	$0.78^{+0.01}_{-0.02}$
HE 1219-0312	$11.19^{+9.94}_{-3.58}$	$7.52^{+3.94}_{-1.93}$	$5.88^{+1.6}_{-0.87}$	$5.72^{+1.76}_{-0.71}$
HE 1221-0522	$1.76^{+0.16}_{-0.14}$	$1.66^{+0.15}_{-0.13}$	$1.67^{+0.14}_{-0.13}$	$1.74^{+0.06}_{-0.21}$
HE 1221-1948	$3.21^{+0.49}_{-0.37}$	$2.81^{+0.4}_{-0.31}$	$2.86^{+0.37}_{-0.31}$	$2.65^{+0.59}_{-0.09}$
HE 1222-0200	$8.88^{+7.94}_{-2.85}$	$6.58^{+3.86}_{-1.78}$	$5.35^{+2.32}_{-1.16}$	$4.46^{+3.21}_{-0.27}$
HE 1222-0336	$1.77^{+0.12}_{-0.11}$	$1.64^{+0.12}_{-0.1}$	$1.64^{+0.09}_{-0.1}$	$1.65^{+0.08}_{-0.1}$
HE 1225+0155	$3.35^{+0.23}_{-0.2}$	$3.09^{+0.28}_{-0.23}$	$3.15^{+0.22}_{-0.15}$	$3.03^{+0.34}_{-0.02}$
HE 1225-0515	$2.41^{+0.23}_{-0.19}$	$2.18^{+0.21}_{-0.17}$	$2.16^{+0.18}_{-0.16}$	$2.17^{+0.17}_{-0.17}$
HE 1230-1724	$1.9^{+0.16}_{-0.14}$	$1.75^{+0.15}_{-0.13}$	$1.78^{+0.13}_{-0.1}$	$1.77^{+0.13}_{-0.09}$
HE 1237-3103	$8.69^{+2.02}_{-1.38}$	$6.37^{+1.39}_{-0.97}$	$6.08^{+0.95}_{-0.76}$	$5.06^{+1.97}_{--0.26}$
HE 1243-1425	$7.98^{+3.7}_{-1.92}$	$5.9^{+2.05}_{-1.21}$	$5.65^{+1.42}_{-1.08}$	$5.14^{+1.92}_{-0.58}$
HE 1245-1616	$4.18^{+1.19}_{-0.76}$	$3.65^{+0.94}_{-0.62}$	$3.55^{+0.68}_{-0.62}$	$3.34^{+0.9}_{-0.4}$
HE 1246-1344	$37.81^{+125.7}_{-16.43}$	$14.26^{+9.01}_{-3.98}$	$11.99^{+4.11}_{-2.42}$	$8.59^{+7.51}_{--0.98}$
HE 1247-2114	$27.69^{+87.16}_{-11.95}$	$12.54^{+8.75}_{-3.65}$	$10.45^{+2.75}_{-1.89}$	$7.81^{+5.39}_{--0.75}$
HE 1248-1800	$13.75^{+20.3}_{-5.14}$	$8.56^{+5.75}_{-2.45}$	$7.49^{+2.55}_{-1.51}$	$5.84^{+4.2}_{--0.14}$
HE 1249-2932	$31.26^{+54.94}_{-12.17}$	$13.48^{+7.8}_{-3.61}$	$11.74^{+3.01}_{-2.09}$	$10.67^{+4.07}_{-1.02}$
HE 1249-3121	$2.58^{+0.2}_{-0.17}$	$2.32^{+0.19}_{-0.16}$	$2.32^{+0.14}_{-0.12}$	$2.32^{+0.14}_{-0.12}$
HE 1251-0104	$7.0^{+2.05}_{-1.29}$	$5.38^{+1.34}_{-0.89}$	$5.15^{+1.12}_{-0.71}$	$4.45^{+1.82}_{-0.01}$
HE 1252+0044	$3.6^{+0.45}_{-0.36}$	$3.12^{+0.39}_{-0.31}$	$3.08^{+0.35}_{-0.23}$	$2.77^{+0.66}_{--0.07}$
HE 1252-0117	$9.9^{+2.54}_{-1.68}$	$6.94^{+1.62}_{-1.11}$	$6.65^{+0.97}_{-0.73}$	$6.67^{+0.95}_{-0.75}$
HE 1254+0009	$11.78^{+3.68}_{-2.27}$	$7.82^{+2.1}_{-1.37}$	$7.42^{+1.17}_{-0.76}$	$7.57^{+1.02}_{-0.91}$
HE 1256-0228	$7.93^{+4.05}_{-2.0}$	$5.91^{+2.23}_{-1.27}$	$5.67^{+1.99}_{-1.07}$	$5.88^{+1.78}_{-1.28}$
HE 1256-0651	$1.2^{+0.05}_{-0.05}$	$1.14^{+0.05}_{-0.05}$	$1.13^{+0.04}_{-0.04}$	$1.14^{+0.04}_{-0.04}$
HE 1259-0621	$13.24^{+40.07}_{-5.68}$	$9.14^{+10.93}_{-3.22}$	$7.39^{+4.8}_{-2.06}$	$5.21^{+6.98}_{--0.11}$
HE 1300+0157	$1.98^{+0.08}_{-0.07}$	$1.83^{+0.09}_{-0.08}$	$1.83^{+0.06}_{-0.05}$	$1.8^{+0.1}_{-0.02}$
HE 1300-0641	$6.24^{+1.02}_{-0.77}$	$4.91^{+0.81}_{-0.61}$	$4.84^{+0.62}_{-0.45}$	$4.58^{+0.87}_{-0.2}$
HE 1300-0642	$7.49^{+1.98}_{-1.3}$	$5.65^{+1.31}_{-0.89}$	$5.42^{+1.0}_{-0.76}$	$6.0^{+0.41}_{-1.34}$

HE 1300-2201	$1.41^{+0.07}_{-0.07}$	$1.33^{+0.07}_{-0.07}$	$1.34^{+0.09}_{-0.08}$	$1.35^{+0.08}_{-0.09}$
HE 1300-2431	$19.48^{+13.77}_{-5.7}$	$10.58^{+4.42}_{-2.41}$	$9.66^{+2.21}_{-1.52}$	$9.34^{+2.52}_{-1.2}$
HE 1305-0331	$3.97^{+1.01}_{-0.67}$	$3.51^{+0.82}_{-0.56}$	$3.25^{+0.58}_{-0.39}$	$3.28^{+0.55}_{-0.42}$
HE 1311-1412	$19.15^{+11.28}_{-5.18}$	$10.44^{+3.98}_{-2.26}$	$10.07^{+2.99}_{-1.58}$	$7.83^{+5.23}_{--0.66}$
HE 1314-3036	$5.69^{+0.66}_{-0.53}$	$4.82^{+0.68}_{-0.53}$	$4.96^{+0.64}_{-0.45}$	$4.34^{+1.25}_{--0.17}$
HE 1320-1339	$1.77^{+0.06}_{-0.06}$	$1.67^{+0.08}_{-0.07}$	$1.67^{+0.04}_{-0.05}$	$1.67^{+0.05}_{-0.05}$
HE 1330-0354	$1.72^{+0.1}_{-0.09}$	$1.6^{+0.1}_{-0.09}$	$1.62^{+0.09}_{-0.08}$	$1.6^{+0.11}_{-0.06}$
HE 1330-0607	$9.59^{+4.24}_{-2.25}$	$6.78^{+2.25}_{-1.35}$	$6.43^{+1.64}_{-0.88}$	$5.79^{+2.28}_{-0.23}$
HE 1332-0309	$-44.47^{+29.53}_{--90.03}$	$49.39^{+-85.49}_{-34.72}$	$15.41^{+13.12}_{-4.68}$	$14.13^{+14.4}_{-3.4}$
HE 1333-0340	$1.82^{+0.16}_{-0.13}$	$1.69^{+0.15}_{-0.12}$	$1.69^{+0.13}_{-0.12}$	$1.69^{+0.13}_{-0.12}$
HE 1335+0135	$3.73^{+0.68}_{-0.5}$	$3.3^{+0.57}_{-0.43}$	$3.3^{+0.42}_{-0.39}$	$3.1^{+0.62}_{-0.19}$
HE 1337+0012	$0.27^{+0.0}_{-0.0}$	$0.27^{+0.0}_{-0.0}$	$0.27^{+0.0}_{-0.0}$	$0.27^{+0.0}_{-0.0}$
HE 1337-0453	$2.65^{+0.39}_{-0.3}$	$2.44^{+0.35}_{-0.27}$	$2.42^{+0.32}_{-0.25}$	$2.43^{+0.31}_{-0.26}$
HE 1343-0640	$1.8^{+0.17}_{-0.15}$	$1.67^{+0.16}_{-0.13}$	$1.7^{+0.17}_{-0.12}$	$1.76^{+0.11}_{-0.18}$
HE 1345-0206	$10.16^{+6.97}_{-2.94}$	$7.1^{+3.22}_{-1.69}$	$7.55^{+2.5}_{-1.74}$	$6.32^{+3.74}_{-0.51}$
HE 1351-1049	$10.61^{+8.54}_{-3.27}$	$7.26^{+3.61}_{-1.81}$	$6.61^{+1.97}_{-1.05}$	$5.08^{+3.5}_{--0.48}$
HE 1413-1954	$1.97^{+0.19}_{-0.16}$	$1.81^{+0.17}_{-0.15}$	$1.84^{+0.24}_{-0.16}$	$1.79^{+0.29}_{-0.11}$
HE 1419-1759	$44.94^{+-274.1}_{-24.47}$	$15.19^{+14.48}_{-4.98}$	$12.61^{+3.33}_{-2.84}$	$10.34^{+5.6}_{-0.57}$
HE 1421-2006	$1.98^{+0.25}_{-0.2}$	$1.85^{+0.23}_{-0.18}$	$1.84^{+0.24}_{-0.16}$	$1.95^{+0.13}_{-0.26}$
HE 1430+0053	$3.24^{+0.21}_{-0.19}$	$2.85^{+0.23}_{-0.2}$	$2.89^{+0.16}_{-0.14}$	$2.84^{+0.21}_{-0.08}$
HE 1430-0026	$1.23^{+0.05}_{-0.05}$	$1.17^{+0.06}_{-0.05}$	$1.18^{+0.06}_{-0.04}$	$1.19^{+0.05}_{-0.04}$
HE 1430-1123	$2.02^{+0.22}_{-0.18}$	$1.88^{+0.21}_{-0.17}$	$1.88^{+0.24}_{-0.18}$	$1.91^{+0.21}_{-0.22}$
HE 1431-2142	$1.42^{+0.13}_{-0.11}$	$1.33^{+0.12}_{-0.1}$	$1.36^{+0.11}_{-0.1}$	$1.4^{+0.07}_{-0.15}$
HE 1500-1628	$17.6^{+18.77}_{-5.99}$	$9.98^{+5.22}_{-2.55}$	$8.61^{+3.36}_{-1.45}$	$6.58^{+5.38}_{--0.57}$
HE 2133-1432	$2.17^{+0.19}_{-0.16}$	$1.98^{+0.17}_{-0.15}$	$2.0^{+0.15}_{-0.11}$	$1.96^{+0.19}_{-0.07}$
HE 2134+0001	$6.21^{+1.7}_{-1.1}$	$4.94^{+1.18}_{-0.8}$	$5.11^{+1.02}_{-0.68}$	$4.83^{+1.3}_{-0.4}$
HE 2139-1851	$7.6^{+1.75}_{-1.2}$	$5.71^{+1.2}_{-0.84}$	$5.68^{+1.39}_{-0.78}$	$5.17^{+1.89}_{-0.28}$
HE 2143+0030	$-67.12^{+45.63}_{--126.85}$	$37.54^{+-139.95}_{-21.68}$	$13.93^{+6.01}_{-2.97}$	$8.98^{+10.96}_{--1.98}$
HE 2145-3025	$6.02^{+1.07}_{-0.79}$	$4.76^{+0.82}_{-0.61}$	$4.82^{+0.73}_{-0.49}$	$5.14^{+0.41}_{-0.8}$
HE 2150-0825	$1.54^{+0.08}_{-0.07}$	$1.45^{+0.08}_{-0.07}$	$1.46^{+0.06}_{-0.07}$	$1.46^{+0.06}_{-0.06}$
HE 2151-2858	$1.22^{+0.06}_{-0.06}$	$1.16^{+0.06}_{-0.06}$	$1.16^{+0.05}_{-0.05}$	$1.22^{+-0.01}_{-0.11}$
HE 2153-2719	$9.5^{+3.76}_{-2.1}$	$6.71^{+2.05}_{-1.27}$	$6.48^{+1.0}_{-1.06}$	$7.35^{+0.12}_{-1.94}$

HE 2154-2838	$4.74^{+0.94}_{-0.67}$	$3.92^{+0.71}_{-0.52}$	$3.81^{+0.47}_{-0.44}$	$3.66^{+0.62}_{-0.29}$
HE 2155+0136	$3.87^{+1.01}_{-0.67}$	$3.34^{+0.78}_{-0.53}$	$3.47^{+0.64}_{-0.6}$	$2.73^{+1.38}_{--0.14}$
HE 2156-3130	$9.55^{+2.02}_{-1.42}$	$6.77^{+1.42}_{-1.0}$	$6.61^{+0.88}_{-0.72}$	$5.54^{+1.95}_{--0.35}$
HE 2158-3112	$9.71^{+3.23}_{-1.94}$	$7.53^{+2.33}_{-1.44}$	$7.24^{+1.04}_{-1.09}$	$6.62^{+1.67}_{-0.47}$
HE 2200-2030	$2.24^{+0.18}_{-0.15}$	$2.04^{+0.17}_{-0.14}$	$2.05^{+0.15}_{-0.11}$	$2.02^{+0.19}_{-0.08}$
HE 2201-0637	$63.03^{+-101.19}_{-45.77}$	$17.03^{+60.2}_{-7.46}$	$8.96^{+2.99}_{-1.83}$	$9.31^{+2.64}_{-2.18}$
HE 2204-1703	$12.28^{+7.52}_{-3.38}$	$7.99^{+3.19}_{-1.77}$	$7.38^{+1.45}_{-1.15}$	$7.11^{+1.71}_{-0.89}$
HE 2206-2245	$7.56^{+2.81}_{-1.61}$	$5.67^{+1.67}_{-1.05}$	$5.65^{+2.07}_{-0.97}$	$7.26^{+0.46}_{-2.58}$
HE 2216-0621	$28.6^{+45.55}_{-10.88}$	$12.82^{+7.19}_{-3.39}$	$10.52^{+2.0}_{-1.67}$	$8.51^{+4.02}_{--0.35}$
HE 2216-1548	$11.13^{+7.97}_{-3.28}$	$7.48^{+3.38}_{-1.77}$	$6.48^{+1.14}_{-1.08}$	$6.19^{+1.43}_{-0.79}$
HE 2217-0706	$13.56^{+6.62}_{-3.35}$	$8.56^{+2.97}_{-1.75}$	$8.11^{+1.84}_{-1.31}$	$7.64^{+2.31}_{-0.84}$
HE 2217-1523	$14.62^{+8.93}_{-4.02}$	$8.91^{+3.49}_{-1.96}$	$8.73^{+2.92}_{-1.9}$	$7.04^{+4.62}_{-0.2}$
HE 2219-0713	$4.33^{+0.41}_{-0.35}$	$3.65^{+0.4}_{-0.33}$	$3.68^{+0.3}_{-0.24}$	$3.75^{+0.23}_{-0.31}$
HE 2221-4150	$2.43^{+0.36}_{-0.28}$	$2.25^{+0.32}_{-0.25}$	$2.26^{+0.27}_{-0.23}$	$2.38^{+0.16}_{-0.34}$
HE 2222-4156	$2.77^{+0.26}_{-0.22}$	$2.48^{+0.24}_{-0.2}$	$2.47^{+0.2}_{-0.19}$	$2.31^{+0.37}_{-0.02}$
HE 2224+0143	$2.99^{+0.2}_{-0.17}$	$2.65^{+0.21}_{-0.18}$	$2.6^{+0.13}_{-0.11}$	$2.71^{+0.02}_{-0.22}$
HE 2224-4103	$7.33^{+2.12}_{-1.34}$	$5.59^{+1.39}_{-0.93}$	$5.26^{+0.8}_{-0.64}$	$6.49^{+-0.43}_{-1.87}$
HE 2226-4102	$6.91^{+1.31}_{-0.95}$	$5.35^{+0.99}_{-0.72}$	$5.3^{+0.73}_{-0.57}$	$6.26^{+-0.23}_{-1.54}$
HE 2227-4044	$0.96^{+0.02}_{-0.02}$	$0.92^{+0.03}_{-0.02}$	$0.92^{+0.02}_{-0.02}$	$0.92^{+0.02}_{-0.02}$
HE 2228-3806	$5.19^{+0.93}_{-0.69}$	$4.24^{+0.73}_{-0.54}$	$4.3^{+0.53}_{-0.54}$	$3.93^{+0.9}_{-0.18}$
HE 2229-4153	$2.63^{+0.11}_{-0.1}$	$2.37^{+0.14}_{-0.12}$	$2.4^{+0.09}_{-0.09}$	$2.36^{+0.13}_{-0.05}$
HE 2231-0622	$6.58^{+3.94}_{-1.79}$	$5.37^{+2.54}_{-1.31}$	$4.89^{+1.75}_{-1.09}$	$3.63^{+3.02}_{--0.18}$
HE 2234-0521	$4.7^{+0.75}_{-0.57}$	$3.91^{+0.6}_{-0.46}$	$3.88^{+0.48}_{-0.41}$	$3.54^{+0.82}_{-0.07}$
HE 2238-2152	$3.92^{+0.66}_{-0.49}$	$3.34^{+0.53}_{-0.4}$	$3.36^{+0.54}_{-0.45}$	$2.96^{+0.94}_{-0.05}$
HE 2240-0412	$1.11^{+0.05}_{-0.05}$	$1.06^{+0.05}_{-0.05}$	$1.09^{+0.05}_{-0.06}$	$1.11^{+0.04}_{-0.07}$
HE 2242-1930	$5.18^{+0.91}_{-0.67}$	$4.22^{+0.71}_{-0.53}$	$4.19^{+0.45}_{-0.47}$	$4.1^{+0.53}_{-0.38}$
HE 2243-0151	$2.05^{+0.17}_{-0.15}$	$1.89^{+0.16}_{-0.14}$	$1.86^{+0.16}_{-0.14}$	$1.85^{+0.17}_{-0.13}$
HE 2244-1503	$4.15^{+0.71}_{-0.53}$	$3.51^{+0.57}_{-0.43}$	$3.37^{+0.45}_{-0.35}$	$3.36^{+0.46}_{-0.34}$
HE 2247-3705	$12.38^{+14.38}_{-4.33}$	$8.06^{+4.92}_{-2.21}$	$7.69^{+4.87}_{-1.87}$	$10.92^{+1.65}_{-5.1}$
HE 2248-3345	$7.75^{+1.61}_{-1.14}$	$5.82^{+1.16}_{-0.83}$	$5.66^{+0.67}_{-0.55}$	$6.2^{+0.13}_{-1.09}$
HE 2250-2132	$1.78^{+0.06}_{-0.06}$	$1.65^{+0.08}_{-0.07}$	$1.66^{+0.07}_{-0.06}$	$1.65^{+0.08}_{-0.05}$
HE 2252-4157	$24.32^{+-150.67}_{-13.23}$	$13.42^{+31.43}_{-5.53}$	$8.75^{+6.19}_{-2.59}$	$12.36^{+2.58}_{-6.2}$

HE 2252-4225	16.45 $^{+15.66}_{-5.39}$	9.78 $^{+5.02}_{-2.48}$	8.58 $^{+1.47}_{-1.69}$	7.67 $^{+2.39}_{-0.77}$
HE 2258-3456	-48.52 $^{+33.9}_{--85.3}$	76.4 $^{+-102.73}_{-60.82}$	10.68 $^{+2.39}_{-2.21}$	11.87 $^{+1.19}_{-3.4}$
HE 2259-3407	2.5 $^{+0.52}_{-0.36}$	2.31 $^{+0.45}_{-0.32}$	2.28 $^{+0.38}_{-0.33}$	2.67 $^{+-0.0}_{-0.72}$
HE 2301-4024	5.3 $^{+2.67}_{-1.33}$	4.51 $^{+1.9}_{-1.03}$	3.98 $^{+1.22}_{-0.79}$	3.34 $^{+1.86}_{-0.15}$
HE 2301-4126	6.06 $^{+2.05}_{-1.22}$	4.81 $^{+1.34}_{-0.86}$	4.5 $^{+0.88}_{-0.75}$	3.51 $^{+1.87}_{--0.25}$
HE 2304-4153	-17.23 $^{+8.98}_{--210.59}$	-43.36 $^{+32.1}_{--66.81}$	10.69 $^{+3.69}_{-3.12}$	6.93 $^{+7.46}_{--0.64}$
HE 2311+0129	3.69 $^{+0.32}_{-0.27}$	3.19 $^{+0.31}_{-0.26}$	3.11 $^{+0.23}_{-0.2}$	2.98 $^{+0.35}_{-0.08}$
HE 2314-1554	7.73 $^{+1.57}_{-1.12}$	5.77 $^{+1.13}_{-0.81}$	5.56 $^{+0.82}_{-0.67}$	5.71 $^{+0.67}_{-0.82}$
HE 2319-0852	14.73 $^{+10.67}_{-4.36}$	8.96 $^{+3.88}_{-2.08}$	7.76 $^{+1.79}_{-1.5}$	7.75 $^{+1.8}_{-1.5}$
HE 2325-0755	1.6 $^{+0.06}_{-0.05}$	1.49 $^{+0.07}_{-0.06}$	1.5 $^{+0.04}_{-0.04}$	1.5 $^{+0.04}_{-0.05}$
HE 2326+0038	3.19 $^{+0.19}_{-0.17}$	2.8 $^{+0.21}_{-0.19}$	2.77 $^{+0.14}_{-0.11}$	2.94 $^{+-0.03}_{-0.27}$
HE 2327-5642	5.74 $^{+0.49}_{-0.42}$	4.72 $^{+0.56}_{-0.46}$	4.7 $^{+0.37}_{-0.27}$	4.72 $^{+0.34}_{-0.29}$
HE 2329-3702	2.42 $^{+0.32}_{-0.25}$	2.19 $^{+0.28}_{-0.22}$	2.19 $^{+0.27}_{-0.21}$	2.26 $^{+0.2}_{-0.28}$
HE 2333-1358	9.3 $^{+3.8}_{-2.09}$	6.6 $^{+2.06}_{-1.27}$	6.37 $^{+1.3}_{-1.07}$	5.05 $^{+2.63}_{--0.25}$
HE 2334-0604	8.63 $^{+1.34}_{-1.02}$	6.66 $^{+1.25}_{-0.91}$	6.44 $^{+0.99}_{-0.61}$	5.72 $^{+1.71}_{--0.11}$
HE 2335-5958	5.07 $^{+1.74}_{-1.03}$	4.37 $^{+1.33}_{-0.83}$	3.9 $^{+0.97}_{-0.47}$	3.84 $^{+1.03}_{-0.42}$
HE 2338-1311	4.65 $^{+1.09}_{-0.74}$	3.85 $^{+0.8}_{-0.57}$	3.68 $^{+0.48}_{-0.4}$	3.22 $^{+0.94}_{--0.06}$
HE 2338-1618	5.13 $^{+0.99}_{-0.72}$	4.18 $^{+0.75}_{-0.55}$	4.15 $^{+0.98}_{-0.51}$	3.54 $^{+1.59}_{--0.1}$
HE 2345-1919	0.7 $^{+0.02}_{-0.02}$	0.68 $^{+0.02}_{-0.02}$	0.68 $^{+0.02}_{-0.02}$	0.69 $^{+0.02}_{-0.02}$
HE 2347-1254	0.78 $^{+0.01}_{-0.01}$	0.76 $^{+0.01}_{-0.01}$	0.76 $^{+0.01}_{-0.01}$	0.76 $^{+0.01}_{-0.01}$
HE 2347-1334	11.98 $^{+4.86}_{-2.68}$	10.29 $^{+4.61}_{-2.43}$	8.85 $^{+2.09}_{-1.28}$	8.57 $^{+2.38}_{-0.99}$
HE 2347-1448	3.06 $^{+0.37}_{-0.3}$	2.7 $^{+0.32}_{-0.26}$	2.66 $^{+0.24}_{-0.21}$	2.62 $^{+0.28}_{-0.18}$

Table 14: Distances for 253 very metal-poor stars from Gaia EDR3 parallaxies - D_π, from corrected parallaxies by Lindegren et al. 2021 - D_L, from paper Bailer-Jones et al. 2021 - D_{BJgeo}, $D_{BLphotogro}$. All distances are in kpc.

target ID	G mag	G_{BP}-G_{RP} mag	V mag	B-V mag	J-H mag	H-K mag
CS 22175-007	13.2	1.0	13.5	0.7	0.5	0.1
CS 22186-023	12.7	1.0	12.8	0.7	0.4	0.1
CS 22186-025	14.0	1.1	14.2	0.8	0.5	0.0
CS 22886-042	13.0	1.1	13.3	0.8	0.5	0.1

CS 22892-052	12.9	1.1	13.2	0.8	0.5	0.1
CS 22945-028	14.4	0.9	14.6	0.7	0.5	0.0
CS 22957-013	13.8	1.1	14.1	0.7	0.5	0.1
CS 22958-083	14.2	1.0	14.4	0.7	0.4	0.1
CS 22960-010	14.0	0.8	13.8	1.0	0.4	0.0
CS 29491-069	12.9	0.9	13.1	0.6	0.4	0.0
CS 29491-109	12.9	1.1	13.2	0.8	0.6	0.1
CS 29497-004	13.8	1.0	14.1	0.7	0.5	0.1
CS 29510-058	13.3	1.0	13.5	0.7	0.4	0.1
CS 30308-035	13.7	1.0	13.9	0.7	0.5	0.0
CS 30315-001	13.4	1.2	13.8	0.9	0.5	0.1
CS 30315-029	13.3	1.2	13.6	0.9	0.6	0.1
CS 30337-097	13.0	1.1	13.2	0.8	0.5	0.1
CS 30339-041	13.7	0.8	13.9	0.6	0.4	0.1
CS 30343-063	12.6	1.4	13.0	1.0	0.6	0.1
CS 31060-047	13.5	1.1	13.8	0.8	0.5	0.1
CS 31062-041	13.8	1.1	13.9	0.8	0.5	0.1
CS 31072-118	12.4	1.2	12.7	0.9	0.5	0.1
CS 31082-001	11.4	1.1	11.6	0.8	0.4	0.1
HD 20	8.9	0.9	9.4	0.2	0.4	0.1
HD 221170	7.3	1.4	7.7	1.1	0.5	0.2
HE 0005-0002	14.4	1.1	14.6	0.8	0.5	0.1
HE 0008-3842	13.1	1.4	13.4	1.2	0.6	0.2
HE 0017-4838	15.9	1.0	16.1	0.7	0.5	-0.0
HE 0018-1349	15.6	0.8	15.7	0.5	0.3	0.1
HE 0023-4825	13.7	0.7	13.8	0.5	0.3	0.0
HE 0029-1839	14.4	1.0	14.5	0.7	0.5	0.1
HE 0037-2657	13.9	1.0	14.0	0.7	0.5	0.1
HE 0039-4154	13.6	1.1	13.8	0.8	0.5	0.1
HE 0043-2845	15.2	0.8	15.3	0.6	0.3	0.1
HE 0044-2459	13.7	0.9	13.9	0.6	0.5	0.0
HE 0044-4023	16.0	0.7	16.1	0.5	0.3	0.2
HE 0045-2430	14.9	0.8	15.0	0.6	0.4	0.1
HE 0049-5700	15.8	0.7	15.92	-	0.3	-0.0
HE 0051-2304	14.9	1.2	15.2	0.9	0.6	0.1
HE 0054-0657	15.3	0.8	15.5	0.6	0.3	0.1
HE 0057-4541	14.7	1.0	14.83	-	0.4	0.1
HE 0104-4007	15.7	1.0	16.0	0.6	0.5	-0.1
HE 0104-5300	13.4	1.1	13.6	0.8	0.5	0.1

HE 0105-6141	13.4	0.9	13.6	0.6	0.4	0.1
HE 0109-0742	14.1	1.0	14.2	0.7	0.4	0.1
HE 0109-3711	16.2	0.6	16.3	0.4	0.2	0.2
HE 0111-1454	12.6	1.2	12.9	0.9	0.6	0.1
HE 0121-2826	15.3	1.0	15.5	0.7	0.5	0.1
HE 0131-2740	14.4	0.9	14.6	0.6	0.4	0.1
HE 0131-3953	15.8	0.7	15.98	-	0.2	-0.0
HE 0143-1135	15.3	0.8	15.5	0.6	0.4	-0.0
HE 0143-4108	15.1	0.9	15.19	-	0.5	0.1
HE 0143-4146	14.5	1.1	14.7	0.8	0.5	0.1
HE 0157-3335	14.2	1.1	14.4	0.8	0.5	0.1
HE 0200-0955	14.7	0.9	14.91	-	0.4	0.1
HE 0202-2204	15.3	0.9	15.38	-	0.4	0.0
HE 0231-4016	15.9	0.7	16.1	0.4	0.3	-0.0
HE 0240-0807	14.8	1.2	15.0	0.9	0.5	0.1
HE 0240-6105	14.5	1.2	14.68	-	0.5	0.1
HE 0243-0753	13.3	1.0	13.56	-	0.4	0.1
HE 0243-5238	13.8	0.9	13.93	-	0.5	0.1
HE 0244-4111	14.8	0.8	15.0	0.5	0.3	0.0
HE 0248+0039	15.6	1.0	15.7	0.7	0.5	0.2
HE 0256-1109	15.4	0.8	15.6	0.5	0.4	-0.1
HE 0300-0751	16.0	1.0	16.26	-	0.3	0.1
HE 0305-4520	13.7	1.1	14.0	0.8	0.5	0.1
HE 0308-1154	15.8	1.1	16.0	0.8	0.4	0.2
HE 0315+0000	15.3	1.1	15.52	-	0.5	0.1
HE 0316+0214	15.2	1.4	15.54	-	0.6	0.1
HE 0317-4640	16.5	0.7	16.63	-	0.3	0.0
HE 0323-4529	14.5	0.9	14.7	0.6	0.4	0.1
HE 0328-1047	14.2	0.9	14.4	0.6	0.4	0.1
HE 0330-4004	16.0	0.6	16.1	0.4	0.4	-0.1
HE 0330-4144	15.9	0.7	16.0	0.4	0.2	-0.1
HE 0331-4939	15.3	1.0	15.50	-	0.5	-0.0
HE 0333-4001	15.9	0.7	16.1	0.5	0.3	0.1
HE 0336-3829	16.7	0.7	16.8	0.4	0.1	0.2
HE 0337-5127	15.6	0.9	15.8	0.6	0.4	0.0
HE 0338-3945	15.2	0.6	15.3	0.4	0.3	0.0
HE 0339-4027	14.3	0.7	14.45	-	0.3	0.0
HE 0340-3430	14.7	0.7	14.78	-	0.3	0.1
HE 0340-5355	15.1	1.1	15.2	0.8	0.5	0.1

HE 0341-4024	13.5	0.7	13.6	0.4	0.3	0.0
HE 0344+0139	15.3	0.9	15.5	0.7	0.3	-0.0
HE 0347-1819	15.5	0.9	15.59	-	0.4	0.2
HE 0353-6024	16.4	1.0	16.6	0.6	0.4	0.2
HE 0400-2917	13.6	1.0	13.8	0.7	0.4	0.1
HE 0401-0138	13.6	1.2	13.8	0.9	0.5	0.2
HE 0417-0821	14.7	0.9	14.8	0.6	0.3	0.1
HE 0430-4404	15.6	0.6	15.72	-	0.2	0.2
HE 0430-4901	14.5	0.9	14.57	-	0.4	0.1
HE 0432-0923	15.0	1.1	15.16	-	0.5	0.1
HE 0436-4008	15.4	0.9	15.6	0.5	0.4	-0.0
HE 0441-4343	15.4	0.8	15.56	-	0.4	-0.0
HE 0442-1234	12.5	1.4	12.91	-	0.6	0.2
HE 0447-4858	16.1	0.7	16.3	0.4	0.3	0.1
HE 0450-4705	14.2	0.9	14.3	0.6	0.3	0.1
HE 0454-4758	13.3	0.9	13.48	-	0.4	0.1
HE 0501-5139	16.0	0.7	16.1	0.5	0.4	-0.0
HE 0501-5644	15.2	1.0	15.5	0.7	0.4	0.1
HE 0512-3835	14.9	1.0	15.12	-	0.5	0.1
HE 0513-4557	15.6	0.8	15.7	0.5	0.4	0.2
HE 0516-3820	14.2	0.9	14.38	-	0.4	0.0
HE 0517-1952	14.5	0.9	14.6	0.6	0.4	0.1
HE 0519-5525	14.9	0.8	15.0	0.5	0.4	0.0
HE 0520-1748	15.3	0.9	15.4	0.7	0.4	0.1
HE 0524-2055	13.8	1.2	14.01	-	0.5	0.1
HE 0534-4615	14.9	0.8	15.06	-	0.4	0.1
HE 0538-4515	15.6	0.7	15.70	-	0.3	0.1
HE 0547-4539	12.7	1.0	12.91	-	0.5	0.1
HE 0858-0016	14.4	1.4	14.72	-	0.6	0.1
HE 0926-0508	12.1	0.6	12.2	0.1	0.3	0.1
HE 0938+0114	10.3	0.6	-	-	0.2	0.1
HE 0951-1152	15.5	1.0	15.7	0.7	0.4	0.1
HE 1006-2218	13.7	0.6	13.77	-	0.2	0.1
HE 1015-0027	15.3	0.7	15.3	0.3	0.3	0.0
HE 1044-2509	14.2	1.0	14.3	0.7	0.4	0.1
HE 1052-2548	13.1	0.7	13.2	0.3	0.2	0.0
HE 1054-0059	14.1	1.3	14.33	-	0.6	0.1
HE 1059-0118	15.7	0.8	15.81	-	0.3	0.1
HE 1100-0137	15.7	0.7	15.8	0.3	0.2	0.0

HE 1105+0027	15.6	0.7	15.6	0.4	0.2	0.3
HE 1120-0153	11.6	0.6	11.8	0.4	0.3	0.0
HE 1122-1429	16.1	0.6	16.1	0.3	0.2	-0.1
HE 1124-2335	14.5	1.0	14.63	-	0.4	0.2
HE 1126-1735	15.9	0.7	15.96	-	0.4	-0.1
HE 1127-1143	15.8	1.0	15.88	-	0.4	-0.0
HE 1128-0823	15.1	0.7	15.2	0.3	0.4	0.1
HE 1131+0141	16.0	0.9	16.10	-	0.5	-0.0
HE 1132+0125	15.7	0.7	15.8	0.4	0.3	0.1
HE 1132+0204	14.5	1.0	14.7	0.7	0.5	0.1
HE 1135+0139	15.7	0.8	15.8	0.5	0.4	0.1
HE 1135-0344	15.9	0.6	15.9	0.3	0.2	-0.1
HE 1148-0037	13.5	0.7	13.6	0.4	0.3	0.0
HE 1207-2031	16.1	0.6	16.2	0.3	0.3	-0.1
HE 1210+0048	15.7	0.6	15.7	0.3	0.4	0.0
HE 1210-1956	16.2	0.7	16.25	-	0.1	0.1
HE 1212-0127	15.6	1.1	15.8	0.8	0.5	0.1
HE 1214-1819	15.1	1.1	15.3	0.8	0.5	0.1
HE 1215+0149	16.0	0.9	16.1	0.6	0.4	0.2
HE 1217-0540	14.9	0.8	15.0	0.5	0.3	0.1
HE 1219-0312	15.8	1.0	15.94	-	0.5	0.1
HE 1221-0522	16.1	0.7	16.18	-	0.4	0.2
HE 1221-1948	15.8	0.7	15.90	-	0.3	-0.2
HE 1222-0200	16.0	0.9	16.13	-	0.4	0.0
HE 1222-0336	15.6	0.6	15.7	0.3	0.3	0.1
HE 1225+0155	12.7	1.1	12.9	0.7	0.5	0.1
HE 1225-0515	15.5	0.6	15.58	-	0.2	0.2
HE 1230-1724	15.7	0.7	15.8	0.3	0.4	-0.0
HE 1237-3103	13.6	1.2	13.82	-	0.5	0.1
HE 1243-1425	15.7	0.9	15.84	-	0.5	-0.0
HE 1245-1616	16.1	0.6	16.16	-	0.4	0.0
HE 1246-1344	14.2	1.1	14.39	-	0.5	0.2
HE 1247-2114	14.8	1.1	15.01	-	0.5	0.0
HE 1248-1800	15.8	1.0	15.90	-	0.3	0.3
HE 1249-2932	13.7	1.3	13.96	-	0.5	0.1
HE 1249-3121	14.2	1.0	14.3	0.6	0.4	0.1
HE 1251-0104	14.9	1.0	15.07	-	0.5	0.0
HE 1252+0044	15.0	0.9	15.2	0.5	0.4	0.1
HE 1252-0117	13.9	1.1	14.10	-	0.5	0.1

HE 1254+0009	14.0	1.1	14.2	1.1	0.4	0.2
HE 1256-0228	15.8	1.0	-	-	0.6	0.1
HE 1256-0651	14.9	0.7	14.9	0.3	0.3	0.0
HE 1259-0621	16.1	0.8	16.19	-	0.3	0.3
HE 1300+0157	13.9	0.8	14.1	0.4	0.4	0.1
HE 1300-0641	14.7	1.0	14.80	-	0.4	0.0
HE 1300-0642	15.0	1.0	15.1	0.6	0.4	0.0
HE 1300-2201	15.4	0.7	15.47	-	0.3	-0.0
HE 1300-2431	14.3	1.2	14.54	-	0.6	0.1
HE 1305-0331	16.3	0.6	16.38	-	0.3	-0.1
HE 1311-1412	13.8	1.2	13.98	-	0.5	0.1
HE 1314-3036	13.0	1.2	13.21	-	0.5	0.1
HE 1320-1339	10.4	1.1	10.7	0.7	0.5	0.1
HE 1330-0354	14.9	0.6	15.0	0.2	0.2	0.0
HE 1330-0607	15.3	1.0	15.44	-	0.5	0.1
HE 1332-0309	15.3	1.0	15.4	0.6	0.5	0.1
HE 1333-0340	15.5	0.6	15.5	0.3	0.3	-0.0
HE 1335+0135	16.1	0.9	16.2	0.5	0.5	0.1
HE 1337+0012	11.3	0.6	11.5	0.4	0.2	0.1
HE 1337-0453	16.1	0.6	16.2	0.3	0.4	0.2
HE 1343-0640	15.7	0.7	15.8	0.4	0.3	0.0
HE 1345-0206	15.5	1.1	-	-	0.6	0.0
HE 1351-1049	15.5	1.0	15.66	-	0.5	0.1
HE 1413-1954	15.2	0.7	15.23	-	0.2	0.1
HE 1419-1759	14.4	1.2	14.58	-	0.6	0.1
HE 1421-2006	16.3	0.8	16.39	-	0.4	-0.1
HE 1430+0053	13.5	0.9	13.7	0.6	0.4	0.1
HE 1430-0026	15.5	0.7	15.6	0.4	0.4	0.0
HE 1430-1123	16.0	0.8	16.1	0.4	0.3	-0.2
HE 1431-2142	15.7	0.7	15.86	-	0.3	-0.0
HE 1500-1628	14.5	1.1	14.73	-	0.5	0.1
HE 2133-1432	15.2	0.8	15.3	0.5	0.3	0.0
HE 2134+0001	15.6	1.0	15.79	-	0.5	0.0
HE 2139-1851	14.0	1.0	14.11	-	0.5	0.1
HE 2143+0030	15.2	1.3	15.5	0.9	0.6	0.1
HE 2145-3025	14.8	0.8	14.9	0.5	0.4	0.0
HE 2150-0825	14.8	0.7	14.96	-	0.2	0.1
HE 2151-2858	15.9	0.8	16.1	0.5	0.3	0.0
HE 2153-2719	14.9	1.1	15.04	-	0.5	0.0

HE 2154-2838	15.4	0.9	15.6	0.7	0.4	0.1
HE 2155+0136	15.9	0.9	16.0	0.7	0.4	0.1
HE 2156-3130	13.8	1.1	14.1	0.8	0.5	0.1
HE 2158-3112	13.0	1.1	13.2	0.8	0.5	0.1
HE 2200-2030	15.5	0.7	15.64	-	0.3	-0.0
HE 2201-0637	15.5	1.1	15.7	0.7	0.4	0.1
HE 2204-1703	14.7	1.1	15.0	0.7	0.5	0.0
HE 2206-2245	15.4	1.0	15.53	-	0.5	0.0
HE 2216-0621	14.1	1.3	14.5	1.0	0.6	0.1
HE 2216-1548	15.5	1.0	15.6	0.7	0.5	0.2
HE 2217-0706	14.6	1.4	14.96	-	0.6	0.1
HE 2217-1523	14.7	1.1	14.9	0.7	0.5	0.1
HE 2219-0713	13.8	1.1	14.21	-	0.5	0.1
HE 2221-4150	16.6	0.7	16.70	-	0.4	0.3
HE 2222-4156	15.3	0.8	15.33	-	0.3	0.2
HE 2224+0143	13.5	1.0	13.8	0.7	0.5	0.1
HE 2224-4103	14.8	1.0	14.9	0.7	0.5	0.1
HE 2226-4102	14.5	0.9	14.63	-	0.4	0.1
HE 2227-4044	14.9	0.7	14.9	0.5	0.3	0.1
HE 2228-3806	14.7	0.9	14.84	-	0.4	0.1
HE 2229-4153	13.2	0.9	13.32	-	0.4	0.0
HE 2231-0622	16.1	0.9	16.4	0.7	0.4	0.2
HE 2234-0521	15.1	0.9	15.38	-	0.4	0.0
HE 2238-2152	15.6	0.8	15.82	-	0.4	0.1
HE 2240-0412	15.5	0.8	15.8	0.5	0.4	0.0
HE 2242-1930	15.3	0.9	15.5	0.7	0.4	0.1
HE 2243-0151	15.3	0.8	15.57	-	0.2	0.1
HE 2244-1503	15.2	0.9	15.35	-	0.4	0.1
HE 2247-3705	15.8	0.9	16.02	-	0.4	0.0
HE 2248-3345	14.5	1.0	14.7	0.7	0.5	0.1
HE 2250-2132	14.2	0.8	14.4	0.5	0.3	-0.0
HE 2252-4157	16.1	0.9	16.3	0.7	0.5	0.1
HE 2252-4225	14.7	1.1	14.88	-	0.6	0.1
HE 2258-3456	16.1	1.0	16.36	-	0.6	0.1
HE 2259-3407	16.8	0.6	16.9	0.4	0.6	-0.2
HE 2301-4024	16.3	0.8	16.5	0.5	0.2	-0.0
HE 2301-4126	15.8	0.7	15.99	-	0.4	-0.0
HE 2304-4153	16.1	1.1	16.3	0.8	0.6	0.1
HE 2311+0129	14.1	1.0	14.39	-	0.4	0.1

HE 2314-1554	14.5	1.0	14.7	0.7	0.4	0.0
HE 2319-0852	15.0	1.2	15.21	-	0.5	0.2
HE 2325-0755	14.2	0.7	13.9	0.5	0.3	0.1
HE 2326+0038	13.8	1.0	14.2	0.6	0.4	0.1
HE 2327-5642	13.7	1.0	13.9	0.7	0.5	0.0
HE 2329-3702	15.8	0.7	15.8	0.4	0.4	0.1
HE 2333-1358	15.1	0.9	15.41	-	0.5	0.1
HE 2334-0604	13.0	1.1	13.3	0.8	0.5	0.1
HE 2335-5958	16.7	0.7	-	-	0.6	-0.2
HE 2338-1311	15.5	0.8	15.6	0.6	0.4	0.1
HE 2338-1618	15.0	0.9	15.4	0.5	0.4	0.1
HE 2345-1919	14.9	0.8	15.1	0.8	0.4	0.1
HE 2347-1254	13.2	0.7	13.4	0.5	0.2	0.1
HE 2347-1334	12.3	1.3	12.6	1.1	0.6	0.1
HE 2347-1448	15.1	0.7	15.2	0.5	0.3	-0.0

Table 15: Gaia EDR3 and BVJHK photometry of 253 very metal-poor stars Barklem et al. (2005).

target ID	fe/H dex	Mg dex	Al dex	C dex	A_V
CS 22175-007	-2.81	0.37	-1.12	0.19	0.040
CS 22186-023	-2.72	0.14	-0.97	0.30	0.068
CS 22186-025	-2.87	0.28	-1.00	-0.68	0.075
CS 22886-042	-2.68	0.23	-1.10	0.01	0.181
CS 22892-052	-2.95	0.12	-0.72	1.00	0.000
CS 22945-028	-2.66	0.32	-0.97	0.21	0.356
CS 22957-013	-2.64	0.17	-0.94	0.10	0.131
CS 22958-083	-2.79	0.40	-0.88	0.64	0.446
CS 22960-010	-2.65	0.25	-0.92	0.82	0.234
CS 29491-069	-2.81	0.28	-1.03	0.18	0.066
CS 29491-109	-2.90	0.30	-0.83	-0.19	0.142
CS 29497-004	-2.81	0.31	-1.04	0.22	0.192
CS 29510-058	-2.61	0.26	-1.00	0.40	0.234
CS 30308-035	-3.35	0.01	-1.01	0.04	0.099
CS 30315-001	-2.98	0.38	-0.97	-0.50	0.053
CS 30315-029	-3.33	0.42	-0.59	-0.43	0.000
CS 30337-097	-2.73	0.29	-0.57	-0.02	0.307
CS 30339-041	-2.20	0.29	-1.07	-0.41	0.333

CS 30343-063	-2.95	0.45	-0.66	-0.67	0.000
CS 31060-047	-2.72	0.25	-1.11	-0.26	0.121
CS 31062-041	-2.67	0.33	-0.86	0.49	0.413
CS 31072-118	-3.06	0.33	-0.81	-0.50	0.068
CS 31082-001	-2.78	0.36	-0.80	0.22	0.132
HD 20	-1.58	0.17	-0.82	-0.34	0.202
HD 221170	-2.14	0.30	-0.37	-0.55	0.000
HE 0005-0002	-3.09	0.42	-0.43	0.17	0.249
HE 0008-3842	-3.35	0.33	-0.84	-0.89	0.175
HE 0017-4838	-3.23	0.25	-0.89	-0.29	0.000
HE 0018-1349	-2.26	0.30	-0.95	0.36	0.220
HE 0023-4825	-2.06	0.22	-1.01	0.31	0.125
HE 0029-1839	-2.50	0.00	-1.00	0.31	0.000
HE 0037-2657	-3.22	0.27	-0.84	0.31	0.213
HE 0039-4154	-3.38	0.55	-0.44	-0.14	0.047
HE 0043-2845	-2.91	0.29	-0.83	0.19	0.093
HE 0044-2459	-3.28	0.34	-0.89	0.45	0.000
HE 0044-4023	-2.56	0.24	-1.05	0.40	0.092
HE 0045-2430	-1.77	-0.04	-1.09	-0.09	0.218
HE 0049-5700	-2.41	0.37	-0.98	0.39	0.235
HE 0051-2304	-2.41	0.30	-0.70	-0.64	0.238
HE 0054-0657	-2.00	0.23	-0.80	0.29	0.160
HE 0057-4541	-2.32	0.25	-0.85	0.17	0.088
HE 0104-4007	-3.30	0.21	-1.03	0.50	0.087
HE 0104-5300	-3.42	0.25	-0.85	-0.01	0.000
HE 0105-6141	-2.55	0.33	-0.67	0.20	0.000
HE 0109-0742	-2.53	0.30	-0.94	-0.14	0.116
HE 0109-3711	-1.91	9.99	9.99	0.31	0.000
HE 0111-1454	-2.99	0.35	-0.54	-0.22	0.000
HE 0121-2826	-2.97	0.43	-0.87	0.54	0.000
HE 0131-2740	-3.08	0.37	-0.69	0.35	0.296
HE 0131-3953	-2.71	0.30	-0.96	2.45	0.000
HE 0143-1135	-2.13	0.33	-0.64	0.23	0.154
HE 0143-4108	-2.62	0.02	-1.10	0.16	0.226
HE 0143-4146	-2.94	0.41	-0.61	0.11	0.061
HE 0157-3335	-3.08	0.40	-0.54	-0.22	0.093
HE 0200-0955	-2.46	0.34	-0.93	0.41	0.172
HE 0202-2204	-1.98	-0.01	-0.55	1.16	0.238
HE 0231-4016	-2.08	0.22	-1.09	1.36	0.007

HE 0240-0807	-2.68	0.30	-0.75	-0.35	0.806
HE 0240-6105	-3.23	0.30	-0.67	-0.25	0.044
HE 0243-0753	-2.49	0.23	-0.47	0.29	0.000
HE 0243-5238	-3.04	0.33	-1.03	0.40	0.127
HE 0244-4111	-2.56	0.34	9.99	0.25	0.254
HE 0248+0039	-2.53	0.26	-0.78	0.09	0.399
HE 0256-1109	-2.73	0.47	9.99	0.67	0.354
HE 0300-0751	-2.27	0.19	-0.62	0.10	0.254
HE 0305-4520	-2.91	0.20	-0.77	0.33	0.137
HE 0308-1154	-2.82	0.62	-0.48	0.38	0.241
HE 0315+0000	-2.73	0.26	9.99	0.18	0.000
HE 0316+0214	-3.13	0.67	-0.49	-0.71	0.100
HE 0317-4640	-2.33	0.31	-0.91	0.22	0.013
HE 0323-4529	-3.15	0.38	-0.81	0.38	0.000
HE 0328-1047	-2.25	0.21	-0.76	0.15	0.466
HE 0330-4004	-2.20	0.25	-0.99	0.08	0.137
HE 0330-4144	-1.90	0.28	-0.87	0.19	0.135
HE 0331-4939	-2.90	0.33	-1.00	0.34	0.266
HE 0333-4001	-2.64	0.37	-0.89	0.32	0.000
HE 0336-3829	-2.75	0.35	-1.12	0.23	0.137
HE 0337-5127	-2.62	0.33	-0.23	0.16	0.544
HE 0338-3945	-2.41	0.39	-0.69	2.07	nan
HE 0339-4027	-1.81	0.31	-0.69	0.18	0.310
HE 0340-3430	-1.95	0.19	-1.00	0.06	nan
HE 0340-5355	-2.89	-0.04	-1.26	-0.11	0.040
HE 0341-4024	-1.82	0.19	9.99	0.27	0.064
HE 0344+0139	-1.81	0.12	-1.26	0.41	0.024
HE 0347-1819	-2.78	0.42	-0.44	0.03	0.080
HE 0353-6024	-3.17	0.21	-0.81	0.29	0.042
HE 0400-2917	-2.88	-0.02	-1.38	0.15	0.259
HE 0401-0138	-3.34	0.42	-1.06	0.24	0.280
HE 0417-0821	-2.33	0.24	-0.75	0.25	0.567
HE 0430-4404	-2.07	0.29	-0.97	1.44	0.162
HE 0430-4901	-2.72	0.17	-1.18	0.09	0.190
HE 0432-0923	-3.19	0.34	-0.96	0.24	0.000
HE 0436-4008	-2.35	0.22	-1.18	0.49	0.130
HE 0441-4343	-2.52	0.32	-1.09	0.33	0.000
HE 0442-1234	-2.41	0.32	-0.34	-0.61	0.349
HE 0447-4858	-1.69	0.24	-0.81	0.04	0.182

HE 0450-4705	-3.10	0.22	-0.86	0.84	0.104
HE 0454-4758	-3.10	0.29	-0.94	0.44	0.068
HE 0501-5139	-2.38	0.19	9.99	0.40	0.041
HE 0501-5644	-2.41	0.29	-0.74	0.27	0.070
HE 0512-3835	-2.40	0.33	-0.44	-0.22	0.000
HE 0513-4557	-2.79	0.34	9.99	0.39	0.000
HE 0516-3820	-2.33	0.22	-1.12	0.39	0.000
HE 0517-1952	-2.61	0.20	-0.84	-0.52	0.081
HE 0519-5525	-2.52	0.41	-0.76	0.29	0.251
HE 0520-1748	-2.52	0.24	-1.07	0.45	0.241
HE 0524-2055	-2.58	0.32	-0.29	-0.25	0.000
HE 0534-4615	-2.01	0.22	-0.87	0.13	0.005
HE 0538-4515	-1.52	0.21	-0.69	0.15	0.000
HE 0547-4539	-3.01	0.13	-1.07	0.50	0.000
HE 0858-0016	-2.73	0.26	-0.41	-0.80	0.000
HE 0926-0508	-2.78	0.28	-0.90	0.62	0.073
HE 0938+0114	-2.51	0.22	-0.79	0.65	0.145
HE 0951-1152	-2.62	0.54	-0.05	0.10	0.582
HE 1006-2218	-2.69	9.99	-0.79	9.99	0.101
HE 1015-0027	-2.66	0.35	-1.00	9.99	0.134
HE 1044-2509	-2.89	0.29	-0.59	0.52	0.014
HE 1052-2548	-2.29	0.16	-0.48	0.51	0.035
HE 1054-0059	-3.34	0.27	-0.77	-0.73	0.126
HE 1059-0118	-2.81	0.46	-0.73	0.37	0.081
HE 1100-0137	-2.92	9.99	-1.17	0.47	0.079
HE 1105+0027	-2.42	0.47	-0.89	2.00	0.351
HE 1120-0153	-2.77	0.04	-1.07	0.63	0.214
HE 1122-1429	-2.65	0.34	-0.92	0.44	0.066
HE 1124-2335	-2.95	0.35	9.99	0.86	0.198
HE 1126-1735	-2.69	0.31	-1.06	0.23	0.078
HE 1127-1143	-2.73	0.22	-0.87	0.54	0.148
HE 1128-0823	-2.71	0.23	-0.97	0.47	0.076
HE 1131+0141	-2.48	0.23	-0.84	0.12	0.084
HE 1132+0125	-2.42	0.38	-1.00	0.24	0.130
HE 1132+0204	-2.55	0.20	-1.04	0.13	0.131
HE 1135+0139	-2.33	0.33	-0.89	1.19	0.263
HE 1135-0344	-2.63	9.99	-1.26	1.03	0.054
HE 1148-0037	-3.47	-0.09	-1.02	0.84	0.000
HE 1207-2031	-2.82	9.99	-0.96	0.64	0.190

HE 1210+0048	-2.28	0.25	-1.15	0.57	0.000
HE 1210-1956	-2.57	0.41	-0.96	0.22	0.139
HE 1212-0127	-2.15	0.13	-0.54	-0.39	0.101
HE 1214-1819	-3.01	0.39	-0.74	0.35	0.335
HE 1215+0149	-2.90	0.35	-0.47	0.15	0.323
HE 1217-0540	-2.95	0.42	-0.71	0.81	0.259
HE 1219-0312	-2.81	0.04	-1.11	-0.08	0.000
HE 1221-0522	-2.84	0.45	-0.67	0.53	0.000
HE 1221-1948	-3.36	0.80	-0.72	1.42	0.113
HE 1222-0200	-2.45	0.17	9.99	0.23	0.000
HE 1222-0336	-2.04	0.09	-1.28	0.22	0.063
HE 1225+0155	-2.75	0.46	-0.54	0.26	0.152
HE 1225-0515	-1.96	0.18	-1.00	0.52	0.000
HE 1230-1724	-2.30	0.22	-1.00	0.13	0.061
HE 1237-3103	-2.91	0.21	-0.84	-0.06	0.000
HE 1243-1425	-2.67	0.22	-1.06	0.51	0.129
HE 1245-1616	-2.98	9.99	9.99	0.77	0.040
HE 1246-1344	-3.40	0.50	-0.74	-0.06	0.292
HE 1247-2114	-2.61	0.25	-0.96	0.32	0.000
HE 1248-1800	-2.89	0.27	-0.71	0.53	0.444
HE 1249-2932	-2.65	0.11	-0.75	-0.41	0.000
HE 1249-3121	-3.23	0.26	-0.81	1.86	0.128
HE 1251-0104	-2.73	0.06	-1.12	0.25	0.239
HE 1252+0044	-3.28	0.51	-0.68	0.60	0.427
HE 1252-0117	-2.89	0.14	-0.82	-0.16	0.167
HE 1254+0009	-2.94	0.26	-0.74	-0.11	0.000
HE 1256-0228	-2.07	0.27	-0.77	-0.04	0.042
HE 1256-0651	-2.36	0.22	-1.06	0.62	0.098
HE 1259-0621	-2.64	0.32	-0.91	0.41	0.000
HE 1300+0157	-3.76	0.40	-0.83	1.17	0.123
HE 1300-0641	-3.14	0.04	-1.21	1.29	0.185
HE 1300-0642	-3.03	0.26	-1.14	0.34	0.058
HE 1300-2201	-2.61	0.29	-0.92	1.01	0.120
HE 1300-2431	-3.25	0.40	-0.73	-0.16	0.000
HE 1305-0331	-3.26	9.99	-0.72	1.13	0.033
HE 1311-1412	-2.91	0.26	-0.62	-0.15	0.000
HE 1314-3036	-2.99	0.32	-0.87	-0.13	0.047
HE 1320-1339	-2.78	0.25	-0.80	-0.51	0.218
HE 1330-0354	-2.29	0.32	-0.93	1.05	0.063

HE 1330-0607	-2.33	0.10	-0.83	0.21	0.085
HE 1332-0309	-2.46	0.13	-0.96	0.21	0.099
HE 1333-0340	-2.64	0.24	-0.82	9.99	0.041
HE 1335+0135	-2.47	0.28	-0.93	0.13	0.292
HE 1337+0012	-3.44	0.55	-0.65	0.71	0.000
HE 1337-0453	-2.34	0.38	-1.07	0.12	0.220
HE 1343-0640	-1.90	0.37	-0.85	0.77	0.154
HE 1345-0206	-2.82	0.11	-1.12	0.34	0.115
HE 1351-1049	-3.46	0.30	-0.77	1.55	0.048
HE 1413-1954	-3.22	9.99	9.99	1.45	0.000
HE 1419-1759	-3.18	0.27	-0.95	-0.20	0.167
HE 1421-2006	-2.65	0.37	-0.97	0.30	0.164
HE 1430+0053	-3.03	0.21	-0.98	0.29	0.165
HE 1430-0026	-2.79	0.29	-0.89	0.52	0.000
HE 1430-1123	-2.71	0.35	-0.91	1.84	0.074
HE 1431-2142	-2.60	0.35	-1.02	0.48	0.296
HE 1500-1628	-2.31	0.18	-1.01	0.13	0.000
HE 2133-1432	-2.02	0.33	-0.78	0.12	0.063
HE 2134+0001	-2.22	0.38	-0.83	0.20	0.221
HE 2139-1851	-3.25	0.36	-0.92	0.49	0.000
HE 2143+0030	-2.43	0.22	-0.71	-0.36	0.208
HE 2145-3025	-2.69	0.36	-0.73	9.99	0.423
HE 2150-0825	-1.98	0.36	-1.09	1.35	0.027
HE 2151-2858	-2.38	0.37	-0.61	0.10	0.166
HE 2153-2719	-2.49	0.36	-0.51	0.12	0.056
HE 2154-2838	-1.85	0.18	-0.66	0.05	0.111
HE 2155+0136	-2.07	0.22	-0.96	0.00	0.076
HE 2156-3130	-3.13	0.77	-0.07	0.74	0.000
HE 2158-3112	-2.75	0.29	-0.71	-0.04	0.000
HE 2200-2030	-2.00	0.24	9.99	0.10	0.375
HE 2201-0637	-2.61	0.19	-0.96	0.14	0.086
HE 2204-1703	-2.79	0.36	-0.41	0.21	0.037
HE 2206-2245	-2.73	0.32	-0.92	0.21	0.256
HE 2216-0621	-3.23	0.22	-0.84	-0.66	0.109
HE 2216-1548	-1.70	0.17	-0.89	-0.38	0.162
HE 2217-0706	-2.56	0.33	-0.52	-0.55	0.175
HE 2217-1523	-2.62	0.32	-0.66	0.04	0.000
HE 2219-0713	-2.91	0.25	-1.03	-0.17	0.000
HE 2221-4150	-2.03	0.32	-1.01	0.23	0.000

HE 2222-4156	-2.73	0.42	-0.93	0.42	0.195
HE 2224+0143	-2.58	0.32	-0.98	0.35	0.016
HE 2224-4103	-2.64	0.36	-0.77	0.23	0.000
HE 2226-4102	-2.87	0.23	-1.01	0.46	0.240
HE 2227-4044	-2.32	0.30	-0.73	1.67	0.257
HE 2228-3806	-3.07	0.33	-0.97	0.42	0.166
HE 2229-4153	-2.62	0.29	-0.79	0.37	0.603
HE 2231-0622	-2.12	0.15	-1.39	-0.08	0.586
HE 2234-0521	-2.78	0.32	-1.09	0.36	0.104
HE 2238-2152	-2.40	0.19	-1.18	0.13	0.050
HE 2240-0412	-2.20	0.28	-0.76	1.35	0.118
HE 2242-1930	-2.21	0.22	-1.07	0.09	0.323
HE 2243-0151	-1.61	0.18	-0.89	0.26	0.050
HE 2244-1503	-2.88	0.30	-0.95	0.15	0.249
HE 2247-3705	-2.27	0.14	-1.02	0.36	0.110
HE 2248-3345	-2.74	-0.08	-1.25	0.21	0.483
HE 2250-2132	-2.22	0.31	-1.07	0.41	0.000
HE 2252-4157	-1.93	0.25	-0.70	-0.15	0.000
HE 2252-4225	-2.83	0.17	-0.78	-0.39	0.000
HE 2258-3456	-2.97	0.24	-0.98	-0.20	0.040
HE 2259-3407	-2.29	0.22	-0.98	0.41	0.120
HE 2301-4024	-2.11	0.20	-0.98	0.30	0.057
HE 2301-4126	-2.37	0.22	-0.92	0.39	0.121
HE 2304-4153	-3.02	0.10	-0.54	-0.65	0.000
HE 2311+0129	-2.78	0.31	-0.87	0.33	0.129
HE 2314-1554	-3.27	0.50	-0.41	0.60	0.037
HE 2319-0852	-3.38	0.13	9.99	-0.32	0.388
HE 2325-0755	-2.85	0.31	-1.02	0.21	0.053
HE 2326+0038	-2.77	0.24	-0.93	0.23	0.339
HE 2327-5642	-2.95	0.14	-0.90	0.43	0.199
HE 2329-3702	-2.16	0.31	-1.06	0.15	0.086
HE 2333-1358	-3.34	0.46	-0.93	0.33	0.259
HE 2334-0604	-3.41	0.06	-0.36	-0.67	0.126
HE 2335-5958	-2.33	0.21	-1.05	0.08	0.000
HE 2338-1311	-2.86	0.38	9.99	0.34	0.061
HE 2338-1618	-2.65	0.16	-0.97	0.47	0.304
HE 2345-1919	-2.46	0.33	-0.59	0.24	0.157
HE 2347-1254	-1.83	0.29	-0.74	0.27	0.000
HE 2347-1334	-2.55	0.28	-0.59	-0.50	0.060

HE 2347-1448	-2.31	0.13	-1.11	0.50	0.000

Table 16: Metallicity $\left[\frac{Fe}{H}\right]$, chemical abundances of Mg, Al, C and reddening from StarHorse for 253 very metal-poor stars.